Premature Cleavage of Ship Plating under Reversed Bending

by

Osamu Muragishi

B.S., Naval Architecture, Osaka University, 1984
M.Eng., Naval Architecture, Osaka University, 1986

SUBMITTED TO THE DEPARTMENT OF OCEAN ENGINEERING IN PARTIAL
FULFILLMENT OF THE REQUIREMENTS FOR THE DEGREE OF

DOCTOR OF PHILOSOPHY IN STRUCTURAL MECHANICS
AT THE
MASSACHUSETTS INSTITUTE OF TECHNOLOGY

FEBRUARY 2001

Signature of Author . . . .
Department of Ocean Engineering
September 29, 2000

Certified by . . . .
Frank A. McClintock
Professor of Mechanical Engineering
Thesis Supervisor

Certified by . . . .
Tomasz Wierzbicki
Professor of Applied Mechanics
Doctoral Committee Chairman

Accepted by . . . .
Nicholas Patrikalakis
Kawasaki Professor of Engineering
Chairman, Department Committee on Graduate Students
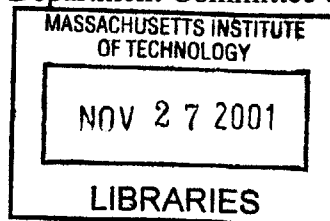
Premature Cleavage of Ship Plating under Reversed Bending

by

Osamu Muragishi

Submitted to the Department of Ocean Engineering
on September 29, 2000 in Partial Fulfillment of the
Requirements for the Degree of Doctor of Philosophy in
Structural Mechanics

ABSTRACT

The objective of the thesis is to develop and apply testing methodology for fracture initiation of actual components of a ship's hull and to provide engineering design data to be used by the industry in predicting the effects of extreme loads such as accidents at sea or earthquakes. Since cleavage is more dangerous than ductile fracture, attention was focused on conditions controlling cleavage fracture. A careful inspection of damaged components of ships and structures damaged in the 1995 Kobe earthquake showed that fracture often initiates in the zones of large bending strains. It was found from the literature that tensile strains resulting from bending alone are not sufficient to cause fracture. A certain amount of reversed strain is needed. Also, temperature is an important parameter of the process.

A comprehensive experimental program was undertaken to study the effects of pre-strain, reversed strain, and temperature. A total of 39 bending specimens cut from actual ship plating were tested and on that basis a 3-D failure surface was constructed for the AH36 steel, suitable for practical applications. The failure surface was formed in terms of compressive pre-strain, temperature, and reverse tensile strain. As-rolled plates pre-strained by -0.43 at room temperature with a Charpy 20 J work transition of 6 °C, cleaved with very small reversed strain of 0.011 at low service temperatures of -40 °C. Machining the surface, as done with conventional test specimens, raised the reversed strain to cleavage to 0.33. Thus, a serious risk is hidden in the use of machined specimens in bending. Effects of other parameters such as aging were also studied on separate types of specimens.

In addition, several mechanisms that could be responsible for the initiation of cleavage were identified and discussed in some depth. Because of the complex interaction between these various mechanisms and effects, it is not possible to make fracture prediction based on first principles. This difficulty necessitates conducting experiments on full-scale test specimens on ship plating which was one of the main objectives of the present thesis. In practical terms, the thesis gives a relatively simple method to chose a steel that could withstand anticipated accidental conditions.

Thesis Supervisor: Frank A. McClintock
Title: Professor of Mechanical Engineering

Thesis Committee: Professor Ali S. Argon
                    Professor Koichi Masubuchi
                    Professor Frank A. McClintock
                    Professor Tomasz Wierzbicki, Chairman

Acknowledgement

This study has been carried out under the supervision of Professor Frank A. McClintock and Professor Tomasz Wierzbicki, to whom I, the author Osamu Muragishi, wish to express my deepest gratitude. I would like to thank Professor Ali S. Argon and Professor Koichi Masubuchi for their helpful comments and discussions during this study.

Mr. Stephen Rudolph prepared all the specimens and the testing machines, to whom I wish to express my appreciation.

Dr. Shoji Tanaka, Dr. Kouji Michiba and Mr. Nobuyuki Ishikawa are most sincerely thanked for their specialized knowledge and support during the study. I also express my profound appreciation to Mr. Yoichi Murakami for help with the temperature equilibration analysis.

Thanks are also extended to the colleagues in the Strength Research Department, Kawasaki Heavy Industries, Ltd., who allowed me to engage in the graduate program in MIT.

Last, but not least, I would like sincerely to thank my wife Hiromi and my children for their perpetual cooperation and patience during the time this work was in process.

Premature Cleavage of Ship Plating
under Reversed Bending

Contents

Part I   Preliminaries

The Need

All ground, sea, and air structures are designed not to be damaged, destroyed, broken down, cracked, torn, or deformed against normal loads, and even some overloads. New design methods have changed against other overloads for structures to reduce serious problems. The oil outflow from Exxon Valdez, which grounded in Alaska in 1989, caused serious environmental damage. Even if a tanker runs aground, it is important that its hull plate is not torn. A partial solution is the requirement of double rather than single hull tankers.

Since the recent Northridge and Kobe earthquakes, design standards for buildings and structures have been reexamined, and improvements in quality and safety of steel and reinforced concrete structures have been proposed (Toyoda, 1995). That is, a steel bridge subjected to a severe earthquake should not collapse. However, in most cases, traditional structural designs have still been applied to structures that are sound; the durability and safety of damaged structures such as grounded tankers and bridges subjected to earthquake have only been investigated individually and tentatively.

The recent computer and information technology revolution is expected to make it more possible to apply an advance in structural design technology. As an example of such a possible

advance, consider a ship grounded on a rock or damaged by an external explosion, and later encountering a storm as it is being sailed or towed to a dry-dock. The objective of this study is to obtain data about the resistance of modern steels to cleavage under reversed bending.

When an accident occurs to a steel structure, bending is likely to cause higher strain than axial deformation. Ripling and Baldwin (1952), Mylonas, Drucker and Brunton (1958), Mylonas (1959), found subsequent brittle behavior in steel pre-strained axially. Ludley and Drucker (1960), Mylonas (1964), and Dvorak and Mylonas (1968) found a fracture mode transition in subsequent reversed bending after bending pre-strain. Especially, when a specimen with an as-rolled surface was subjected to compressive strain by pre-bending, cleavage fracture in reversed bending occurred with less pre-strain than a specimen with a machined surface, and with strains only a few times the yield strain. In reversed bending tests at –27 °C, the transition pre-strain was $\varepsilon_{pre} = -0.43$ for ABS-B steel specimens with as-rolled surfaces.

In the American Bureau of Shipping (ABS) standards, a specific Charpy V-notch work is required at only one temperature. For example, a minimum of Charpy V-notch work of 34.3 Nm is required for AH36 steel at 0 °C, DH36 at –20 °C, and EH36 at –40 °C. The actual temperature in service varies over a range. The temperature of ship structure submerged in icy seawater is about 0 °C, while the steel plate above waterline and steel construction on the ground in cold winter could be as cold as –40 °C. Fracture mode transitions are usually described as a transition in Charpy V-notch work or appearance in terms of temperature. For reversed bending, the concept must be expanded to a transition in reversed strain in terms of temperature and pre-strain.

The currently available structural steels have been improved since the 1950's. A goal of this research is to obtain the transition data on modern steels.

The Structure of the Thesis

This thesis is made up of three major parts.

In Part I, preliminaries consisting of the need, this section, major results, and titles of figures and tables are introduced.

Part II was edited in the format of a journal publication. Following abstract and nomenclature, an introduction is presented in Section 1. Prior work is discussed in Section 2 in terms of the many factors affecting cleavage on reverse bending.

In Section 3, to characterize the bending strain history, a relation between bending angle of specimen and bending strain is derived from an assumption of non-hardening plane strain plate bending. Measured strains and FEM results are used to judge the relation.

In Section 4, test conditions are selected based on the prior work and practical considerations. The high tensile strength shipbuilding steel AH36 is chosen from the present ABS Standard grades as being most likely to cleave since it has a highest Charpy transition temperature. A new type of bend specimen is designed so that plane strain bending of an as-rolled surface can be obtained.

In Section 5, the apparatus and the procedure are introduced and the test results are given. A

discussion of the results is given in Section 6, followed by conclusions in Section 7.

In Part III, details of tests and analyses supporting Part II are reported as individual appendices.

Major Results

In reverse bending tests, the pre-strain and the temperature of reverse straining were changed while the other factors such as aging and strain rate were held constant. The pre-strain was taken from $\varepsilon_{pre} = -0.20$ to -0.43 and the temperature on reverse bending was taken from a room temperature to $T = -40$ °C.

The high strength steel AH36, rated to 0 °C, in bending of as-rolled plates, pre-strained at room temperature by $\varepsilon_{pre} = -0.43$, cleaved with very small reversed strain $\varepsilon_{rev} = 0.011$ at low service temperatures from -30 to -40 °C. The low ε_{rev} rose abruptly with either less $|\varepsilon_{pre}|$ or higher service temperature.

On the three dimensional space of pre-strain, temperature, and reverse strain, all cleavage points were found to be between two limit surfaces of a locus. The surfaces were found to mean a cleavage transition over the domain of pre-strain and the reverse bend temperature.

A machined surface condition obscures the risk of premature cleavage found on as-rolled surfaces.

A system for pre- and reversed plane strain bending has been developed, along with approximate relations between testing machine displacement, bend angles, and strains.

List of Figures and Tables

Part II   Main Body of the Thesis

Nomenclature

h	bent plate thickness
h_p	plate thickness
H_{MS}	modified superficial hardness
H_{RB}	Rockwell B hardness
l	half of pinhole distance of specimen
l_{eff}	effective length of bending
N	power-law hardening exponent
R_C	radius of corner of specimen groove
R_i, R_o	inner and outer radii of bent plate
R_u	radius of unstretched element of bent plate
s_h	length of plate whose thickness is h
s_{eff}	effective length of bent plate
t	time
T	temperature
T_m	modified temperature

T_{pre}	temperature at pre-bending
T_{rev}	temperature at reverse bending
T_{CVN}	Charpy V-notch work transition temperature
T_{RBC}	reverse bending cleavage transition temperature
w_0, w	certain initial and current distances between two rigid parts of the bent specimen
x_0, x	initial and current end-loading pin separations
Δx	pin separation increment
α	coefficient in velocity-modified temperature conversion
β_{pre}, β	initial and current end-to-end bend angles
$\Delta\beta$	bend angle increment
δ	increment of end-load displacement
ε	engineering strain
$\dot{\varepsilon}, \dot{\varepsilon}_0$	engineering strain ratios on the inside and outside of bent plate
$\varepsilon_i, \varepsilon_o$	engineering strains on the inside and outside of bent plate
$\varepsilon_{i,true}, \varepsilon_{o,true}$	true (logarithmic) strains on the inside and outside of bent plate
ε_{pre}	pre-strain
ε_{rev}	reversed strain
ε_{revf}	reversed strain to fracture
ε_{true}	true strain
$\Delta\varepsilon_{i,true}, \Delta\varepsilon_i$	true and engineering additional bending inside strain
θ	angle of bent specimen $(\theta + \beta = \pi)$

1.   Introduction

If a ship encounters an extreme event at sea, such as a stranding, grounding, collision, or the explosion shown in Figure 1a, nominal strains as high as $|\varepsilon| = 0.5$ can be produced by local folding of plates resulting from buckling or tripping. This can occur in stiffened plates or at corners of structures. As shown in Figure 1b, reversed strain could follow the large pre-strain. In 1997, the Structures and Composites Division of NSWC (Naval Surface Warfare Center) conducted model tests on 3-bay grillage (Figure 2) and box girders (Figure 3) to study the effect of underwater explosions on the instantaneous and deferred damage of a ship's hull. It was found that fracture occurred after only a few cycles or even during reverse straining at locally buckled stiffeners and bent plates. In service, the subsequent strain could be a single reaction to the prior event, or a repeating strain caused by a navigation in a rough sea. The tensile strains developed by the first bending usually are not sufficient to cause immediate fracture. However, after a high compressive strain of $|\varepsilon| = 0.5$, a reversed strain to fracture as small as $\varepsilon_{revf} = 0.01$ (e.g. Mylonas 1964) can cleave a structural element almost entirely. Such a small reversed strain may be caused by normal service loads subsequent to the accident. If the reversed bending occurs in icy seawater or cold weather, cleavage can occur after even smaller compressive pre-straining.

Additionally, it has been found that cleavage occurs more easily with the typical as-rolled surfaces of ship plates instead of the machined surfaces of specimens (Dvorak and Mylonas 1968). Further work for the cleavage problem in reverse bending is quite extensive and will be reviewed in Section 2.

Besides ships in storms after accidents, there are many other examples of highly bent plates which may later undergo strain reversals. In steel railway or highway tank cars in collisions, the strain reversals may be caused by elastic springback or vehicle recovery operations. Cleavage is especially dangerous if it causes leaking of hazardous contents. In buried pipelines under earth-quake conditions, large strains and reversals occur. In structures or buildings subjected to earth-quakes, the problem may be less critical, because the structures would have collapsed under large distortions, or would have cracked in later fully plastic cycles. However, a preliminary experi-ment did show final cleavage after 1.5 cycles, as described in Appendix I.

For the safety of the damaged ship or structure before it can be repaired or replaced, data are needed to predict cleavage with various temperatures, pre-strains, and reversed strains. Further-more, in advanced structural design for accidental or explosive massive loads, data for the tough-ness of damaged steel plate should be needed in the near future. Figure 4 is showing an imagi-nary test specimen drawn at the local buckling of T-stiffener buckled by a compressive load. The upper surface element on the specimen is subjected to a compressive strain due to the bending. The goal of this research is to obtain the conditions for cleavage in reverse bending of plate with large compressive pre-strain and at low temperature.

2.   Prior Work on Effects of Variables

In absence of pre-strain (ε_{pre}), there is a transition in some measure of ductility, such as total work, strain to fracture, or fracture appearance, as a function of temperature (T). With a strain reversal after pre-strain, the reversed tensile strain to fracture (ε_{revf}) can be taken as a measure of ductility. The transition in ε_{revf} is a function of both T and ε_{pre}. At a constant ε_{pre}, there is a transition in ε_{revf} with T; at a constant T, there is a transition in ε_{revf} with ε_{pre}. In general, the ε_{revf} is a function of both T and ε_{pre}. That is, the brittle to ductile transition becomes a locus in the T-ε_{pre} plane.

The current structural steels for shipbuilding should have lower transition temperatures than those of 50 years ago. To find out conditions for cleavage on reverse straining in a current structural steel for ships is the focus of this research.

2.1   Cleavage after Large Pre-bending and Small Reversed Bending

Ludley and Drucker (1960) tested E-steel beams (yield point: 228 MPa, tensile strength: 421 MPa, and 36.5 % elongation over 2 in. with 0.5 in. diameter). They observed brittle fractures

in reverse bending below -18 °C after a pre-strain of $\varepsilon_{pre} = -0.6$ on the inside of curved specimens. (Since all prior researchers have used the engineering or nominal strain, it will be used here unless otherwise specified. True or equivalent strain will be defined in Section 3.1.) Mylonas (1964) found that ABS Class C steel bars pre-strained to $\varepsilon_{pre} = -0.63$ cracked and fractured with reversed strains of the order of $\varepsilon_{revf} = 0.01$ at $T = -26.7$ °C (-16 °F).

Reverse bending tests using flat bars or beams have been reported also by many other authors (e.g. Mylonas and Rockey 1961, Dvorak and Mylonas 1968, Yamamoto 1995) to study the effect of pre-strain on the ductile-to-brittle transition in reversed strain.

2.2   Temperature on Reverse Bending

In ships voyaging in a cold sea, the temperature of the hull plating exposed to seawater can be somewhat below 0 °C and the structure above the water line could be much colder. Temperatures strongly affect the ductile-to-brittle transition pre-strain. Mylonas (1964) found that, at -26.7 °C (-16 °F), the transition pre-strain was only 50 to 60 % of that at 23.9 °C (75 °F) to induce cleavage on reverse bending.

2.3   Temperature on Pre-bending

Mylonas and Rockey (1961) found that, for the E-steel, a high temperature of pre-bending increased the brittleness in subsequent reverse bending. The compressive pre-strain at 260 °C (500 °F) needed for a brittle fracture on reversal was $\varepsilon_{pre} = -0.35$, while the value at room temperature was $\varepsilon_{pre} = -0.55$. Similarly, Dvorak and Mylonas (1968) demonstrated with ABS-B steel (yield point: 234 MPa, tensile strength: 407 MPa, and 33 % elongation over 8 in. with 1.5

in. width) that the compressive pre-strain at 288 °C (550 °F) needed for a brittle fracture on reversal was $\varepsilon_{pre} = -0.23$ while the value at a room temperature was $\varepsilon_{pre} = -0.43$. Such high temperatures are only likely in welding, giving lower pre-strains, and not for extreme events at sea.

2.4 Aging and Strain Rate

MacGregor and Fisher (1946) found that aging, measured as a change of flow stress, requires longer at lower temperature. This is correlated with the rate-modified temperature. Lower temperature corresponds to higher strain rate after bending. Ludley and Drucker (1960) reported an aging effect in reverse bending using E-steel specimens. Their aging was carried out at 150 °C for 1.5 hours after bending. They concluded that "Aging is harmful," i.e., the compressive pre-strain for brittle fracture in reverse bending was always less for aged specimens than for unaged ones, but they did not mention by how much.

2.5 Surface Condition

Unlike cylindrical specimens with machined surfaces, bending specimens can be manufactured with the surface condition encountered in practice, such as-hot-rolled or corroded surfaces. Surface conditions strongly affect the fracture toughness of bending specimens.

Dvorak and Mylonas (1968) reported that when ABS-B steel was pre-strained in bending at room temperature and reverse bent at –27 °C, its transition pre-strain was about –0.43 with an as-rolled surface but –0.55 with a machined surface.

Hutchinson and Tvergaard (1980) carried out a bifurcation analysis with the finite element

method of surface roughening in tension on a statically bent plate. They showed that small initial surface irregularities grew into cracks, while no cracks grew from a smooth surface.

To obtain the conditions for crack initiation and cleavage in reversed bending, the surface as used in service should be tested. The conditions can be roughly categorized into two conditions, i.e., smooth and rough. The machined surfaces are typically smooth, while as-received ship plates are as-hot-rolled, rusted, or corroded. As the first step of investigating the surface condition effect and for convenience, it is worth starting with the as-rolled surfaces, as did Dvorak and Mylonas.

Hardened surfaces also give different conditions for crack initiation. Dvorak and Vrtel (1966) used V-notched low-alloy mild steel specimens in three point bending, which normally fractured in ductile way. They reported a low-stress brittle fracture when a nitrided surface layer in the notch root was used. Dvorak (1966) hardened the notch root by pre-bending in compression, and found a low-stress brittle fracture on reverse bending.

2.6   Choice of Steel and its Charpy Transition Temperature

In ABS-B steel, Dvorak and Mylonas (1968) found the Charpy V-notch 20 J work transition temperature to be −12 to −8 °C. In reverse bending at −27 °C, they found a transition pre-strain at $\varepsilon_{pre} = -0.43$, with $\varepsilon_{revf} \sim 0.01$. This means that, with the high compressive pre-strain, the unnotched steel has a $\varepsilon_{revf} = 0.01$ transition temperature of −27 °C that is less than, but comparable to the 20 J Charpy V-notch transition temperature.

The specifications of present high-strength structural steel plates for hulls have been standardized by the American Bureau of Shipping (ABS, 1984) and ASTM (1997). The grades that are required to have the highest yield point (353 MPa) are AH36, DH36, and EH36. A minimum

of Charpy V-notch work of 34.3 J is required for all these grades, AH36 at 0 °C, DH36 at –20 °C, and EH36 at –40 °C. While grade AH36 is required to be semi-killed or killed, DH36 and EH36 are not only to be killed but also to meet the fine grain practice requirement described in ABS Standard (1984), Material for Hull Construction and Equipment. This corresponds to the fact that the steels with finer grain sizes are tougher.

Presumably, the transition temperature of unnotched AH36 steel to cleavage in plane strain reverse bending would have been much lower than the Charpy V-notch transition temperature. McClintock and Parks (1999) reported that a means is needed to use data from small specimens to predict cleavage in structures. To compare the Charpy V-notch transition temperature with that in reverse bending for AH36 is another focus of this research.

2.7   Axisymmetric Tension-Compression vs. Plane Strain Bending

The reverse bending tests described above were preceded by studies on reverse axial straining. Ripling and Baldwin (1952) used an intrinsically ductile structural steel SAE1340 pre-strained by $\varepsilon_{pre} = -0.8$ and found brittle fracture at $T_{rev} = -79$ °C (–110 °F). Mylonas (1958, 1959) used E-steel and found that compressive pre-strain led to cleavage in subsequent tension around 14 °C (–10 °F), but he did not estimate the pre-strain. Hawley and Drucker (1973) conducted axisymmetric tests using 1020 hot-rolled steel. The specimens pre-strained to $\varepsilon_{pre} = -0.65$ showed a cleavage fracture in following tension at a small plastic strain of 0.02. Yamamoto et al (1995) used a pre-compressed cylindrical specimen made of JIS SS400, whose virgin elongation over 12.9 mm with 3 mm in diameter was 0.3. His group reported that a pre-strain of –0.5 decreased the elongation in tension to 0.1, but still gave micro-ductile fracture.

For steel plate with more than a certain thickness, the mechanical parameters of yield

strength, tensile strength, and elongation are commonly measured in a round tension specimen. If isotropic, the round specimen has an axisymmetric plastic strain state; i.e., the ratio of principal plastic strains is 1 : –0.5 : –0.5. In plate bending, the state is a plane strain condition, i.e., the ratio of principal plastic strains is 1 : 0 : –1. Clausing (1970) found that the ductility, defined as an equivalent strain to fracture, in plane strain was 72 % of the axisymmetric value for mild steel with 270 MPa yield strength, and only 17 % for steel with a 1710 MPa yield strength. Thus, the strain state changes the brittle fracture conditions.

Round specimen tests are essential when a characteristic of the standard tensile test is of interest. For actual structures, however, tests that model the stress and strain states in critical components are essential for exploring the differences between materials and the environmental effects on the borderline between ductile and brittle behavior of the structure.

In plate bending, unlike axial tension, there is a residual stress, which varies across the cross section. The effects of residual stress on cleavage fracture in axial loading and bending have been studied extensively (Mylonas 1959, Mylonas 1961, Hall et al. 1967), and the residual stresses were found not to contribute significantly in the initiation of brittle fracture of bars subjected to reversed bending. In cleavage on reversed bending, since the reversed strain to fracture is usually much larger than the yield strain, the effect of residual stress is lost before fracture.

The bending test on rectangular cross-section specimens cut from ship plating is a practical and convenient method to evaluate structural steel used in shipbuilding, much closer to the service situation than reversed axial loading.

2.8   Summary of Prior Work

From the above literature survey, three factors out of various effects appear to be key in

determining cleavage in reverse bending of ship steel plates: high compressive pre-strain, low temperature, and high reversed tensile strain. Additionally, since the rough surface reduces the tensile strain to crack initiation in plate bending, the cleavage conditions should be examined on as-rolled surfaces instead of machined surfaces.

The other factors, such as temperature during pre-strain, aging, and strain rate, also affect whether or not the material cracks in a brittle way. However, to find the dependence of cleavage on the main factors, other factors should be kept constant.

One purpose of this paper is to quantify the conditions for cleavage in reverse bending of a present shipbuilding steel plate to see whether it has been improved over steels studied in the 1960's.

3.   Analysis

Before discussing test conditions, the relations between the bending strains and the bend angle or the machine head displacement are considered.

First, the specimen is bent using a 4-point configuration by about 40 degrees. Then the specimen is bent in the end-loading configuration of Figure 5 up to a specified angle. The end-loading configuration is also used for reversed bending. In the following subsections, the bending strains are calculated based on the plane strain, non-hardening, pure bending plate theory of Hill (1950) and Lubahn and Sachs (1950), and compared with a finite element analysis of the actual specimen.

3.1   Relation between Strain and Bend Angle

The thickness of the mid-length of the bending specimen in Figure 6 is reduced to concentrate the bending strain in the middle, leaving the ends rigid. To derive a simple relation between the bending strain and the bend angle, the bent specimen is modeled as three parts (Figure 7). The bending part has a thickness h and length s_{eff}. The rigid parts have a length l_{eff}. These effec-

tive lengths are functions of the geometry shown in Figures 6 and 8:

$$s_{eff} = f(s_h, h, R_C), \quad l_{eff} = g(s_h, h, h_p, R_C, l_p)$$ (3.1)

For a more precise evaluation, s_{eff} and l_{eff} should also be functions of bend angle β. However, in the following analyses, the variation of them during bending was assumed small enough to be neglected, and $s_{eff} = 25.4$ mm and $l_{eff} = 90$ mm were used.

Assume that the material is nonhardening (perfectly plastic) in plane strain, and an uncracked continuum. Under this condition, Hill derived that the thickness remains unchanged after bending. For large bending, the unstretched (neutral) plane, which has experienced the same amount of first compression and then extension during bending, turns out to be at the middle of the plate. If the bend angle is β and the angle of the bent specimen is θ, from Figure 7,

$$\beta + \theta = \pi$$ (3.2)

The lengths of the outside and inside elements are respectively

$$s_{eff} + \frac{h\beta}{2}, \quad s_{eff} - \frac{h\beta}{2},$$ (3.3)

giving the engineering strains:

$$\varepsilon_o, -\varepsilon_i = \frac{h\beta}{2s_{eff}} = \frac{h(\pi - \theta)}{2s_{eff}}$$ (3.4)

The true strains are

$$\varepsilon_{o,true} = \ln\left(1 + \frac{h\beta}{2s_{eff}}\right), \quad \varepsilon_{i,true} = \ln\left(1 - \frac{h\beta}{2s_{eff}}\right).$$ (3.5)

In terms of the inner and outer radii, R_i and R_o, of the curved plate, which are easiest to measure, eliminating h gives

$$\varepsilon_o, -\varepsilon_i = \frac{h}{2R_u} = \frac{R_0 - R_i}{R_0 + R_i} = \frac{h/2}{R_i + h/2} \quad \text{where} \quad R_u = \frac{R_i + R_o}{2}$$ (3.6)

In terms of the bend angle increment $d\theta$, the strains are

$$-\frac{d\varepsilon_o}{d\theta} = \frac{d\varepsilon_i}{d\theta} = \frac{h}{2s_{eff}}.$$ (3.7)

3.2   Pre-Strain as a Function of Bend Angle

The pre-strains are calculated from the bend angle of the specimen using (3.4). The curve of the engineering strain versus the bend angle for $h = 9.525$ mm and $s_{eff} = 25.4$ mm is plotted in Figure 9. Also plotted are results from a numerical analysis (FEM) using the commercial nonlinear structural analysis code ABAQUS, measured data from marks on the specimen surface, and data from internal radii R_i measured with drill bits and interpreted with Equation (3.6), are plotted as well to validate the approximate expression in Equation (3.4) and the FEM result. The true strains ε_{true} obtained from the FEM were converted to engineering strains ε, both axial, using

$$\varepsilon = \exp(\varepsilon_{true}) - 1$$ (3.8)

The non-hardening plane strain bending theory is representing good strain estimates for the large angle bending of the plate. Therefore, Equation (3.4) was used for pre-strain estimation in the reverse bending tests. For details of the comparison of bending strains together with some results measured by curvature, see Appendix A. For details of the FEM analysis, refer to Appendix B. For details on the measured data, see Section 5.2.

3.3   Reverse Strain as a Function of End Displacement

The reverse bending is done with the end-loading configuration in the temperature-controlled chamber of Figure 5c, where the change of bending angle is not easily measured. Instead,

3. Analysis

the reverse strain is calculated from the end-load displacement.

Suppose that the bent specimen is opened from an pre-bent initial angle of θ_0 to a final angle θ. The relation between the angle θ and the pin separation x is given in terms of the distance w between the center lines of the two rigid parts in Figure 7.

$$2l_{eff} \sin \frac{\theta}{2} = x - w \tag{3.9}$$

In the range from $\theta = 45$ to 120 degrees with $l_{eff} = 90$ mm, $s_{eff} = 25.4$ mm and $h = 9.525$ mm, it is shown in Appendix C that the change of w is less than 0.9% of x, and w is almost constant. Therefore, Equation (3.9) can be well approximated as

$$x = 2l_{eff} \sin \frac{\theta}{2} + w_0 \quad \text{where } w = w_0 \text{ when } \theta = \theta_0. \tag{3.10}$$

For the bent plate whose arc length is s_{eff} and pre-bend angle is β_{pre}, the inside true strains due to the bending increment $\Delta\beta$, i.e., for the bend angle of $\beta_1 = \beta_{pre} + \Delta\beta$, are from Equation (3.5)

$$\Delta\varepsilon_{i,true} = \ln\left(\frac{1 - \beta_1/s_{eff} \cdot h/2}{1 - \beta_{pre}/s_{eff} \cdot h/2}\right) = \ln\left(1 - \frac{\Delta\beta}{2s_{eff}/h - \beta_{pre}}\right) \tag{3.11}$$

For the practical range of $\beta_{pre} = 60$ to 135 degrees and $\Delta\beta = 0$ to -80 degrees with $s_{eff} = 25.4$ mm and $h = 9.525$ mm of the reverse bending conditions, (3.11) is well approximated within 7 % of the largest strain increment by using the first term of the series expansion of (3.11) with a coefficient of 0.88,

$$\Delta\varepsilon_i = -\frac{0.88\Delta\beta}{2s_{eff}/h - \beta_0} \tag{3.12}$$

Combining (3.10) and (3.12) with (3.2), for an increment of end displacement Δx, the additional bending inside strain is

$$\Delta\varepsilon_i = \frac{0.88}{s_{eff}/h - \pi/2 + \theta_0/2}\left[\arcsin\left(\frac{\Delta x}{2l_{eff}} + \sin\frac{\theta_0}{2}\right) - \frac{\theta_0}{2}\right]. \tag{3.13}$$

For positive Δx, that is, increase of the pin separation, the additional bending strain at the

inside of the bent plate is tensile. Figure 10 shows the relation of reversed strain ε_{rev} to the end

displacement Δx for various initial bend angles θ_0. For details of the derivation, see Appendix C.

4.   Test Conditions

4.1   Specimen

(1)   Choice of Steel

Of the currently available three grades of high-strength structural steel plates for hulls

mentioned in Section 2.6, AH36 was chosen as being most likely to cleave since it has the

highest transition temperature. Chemical compositions and mechanical properties and parameters

in the longitudinal direction, provided by the supplier for this heat, are given in Table 1. Me-

chanical parameters for the transverse direction are also given from local tests. The apparent

grain size of this steel was measured from photomicrographs (e.g. Figure 11) using the random

line intersection method (ASTM E112-96, 1997). The average volumetric pearlite-ferrite-bainite

grain diameter was 0.0696 ± 0.0064 mm (95 % confidence). The corresponding ASTM grain size

number was 5.7. For details of grain size measurement, see Appendix D.

Tensile tests were carried out using specimens whose diameter was 6.35 mm and length of

reduced section was 63.5 mm (see Appendix E). The stress strain curves are shown in Figure 12;

they have about half the strains after the peak loads that would be expected with the standard

ASTM gauge length-to-diameter ratio of four. Figure 12 also contains the true stress-strain curve

used for the bending strain FEM calculations of Appendix B. The Charpy V-notch impact results

of Figure 13 show that the brittle to ductile transition in work is nearly the same for the LS and

TS orientations and extends from –25 or below to 100 °C (Appendix F), where L represents the

longitudinal (rolling) direction, T the long transverse direction, and S the short transverse direc-

tion.

Tetragonal (elongated cube) coupons were machined from the same steel. The Rockwell B

hardness was taken on the two surfaces facing L and S directions. Both hardnesses were $H_{RB} =$

89±1.

(2)   Dimensions of Bend Specimen

The bending specimen in Figure 6 was machined from AH36 steel plates 25.4 mm thick.

The two ends are forked, with holes for the end-loading. One side of specimen was either left as

rolled or machined to a clean surface, and this surface became the inside when pre-bent. The

central part of the other side was reduced to 9.525 mm, and had curved corners to avoid cracks

caused by strain concentration in the pre-bending. The central part with reduced thickness has a

rectangular cross section with an aspect ratio of 4 so that on pre-bending its center is approxi-

mately in plane strain (McClintock and Argon 1999, pp 349-353).

As indicated in the ASTM Standard, this steel has a lower Charpy work or toughness in the

transverse than the longitudinal direction. The long direction of the specimen was taken in the

transverse direction of the plate to study the more likely conditions for cleavage in reverse

bending.

4.2   Strain Magnitude

To estimate an order of magnitude of the strain history including pre-strain and reversed

strain resulting from an accident and the following service, the following example was studied.

(1)   Pre-Strain

The initial damage, or pre-strain, might have arisen from extreme curvatures at a local dent

in the hull caused by an underwater ledge. The pre-strain could also have arisen at extreme

transverse curvatures in stiffeners by folding over or "tripping" or due to an external explosion.

Large displacement and acceleration of earthquakes might have caused local buckling and

extreme bending on steel structures such as bridges and buildings. A variety of damaged struc-

tures typically show the most curved plates to have the ratio of the outer radius to the inner

radius, R_o/R_i, of about 3.

The resulting engineering bending strain on the surface of the curve is approximately, from

(3.6),

$$|\varepsilon_{\max}| = \frac{R_o - R_i}{R_o + R_i} = 0.5, \quad |\varepsilon_{\max}| = \frac{R_o/R_i - 1}{R_o/R_i + 1}, \quad \frac{R_o}{R_i}\left(1 - |\varepsilon_{\max}|\right) = 1 + |\varepsilon_{\max}|. \tag{4.1}$$

Assuming, as derived in Section 3.1 for non-hardening alloys, that the plate thickness h remains

constant even for large curvatures gives an alternative expression:

$$|\varepsilon_{\max}| = \frac{h/2}{R_i + h/2} = 0.5. \tag{4.2}$$

In the reverse bending test, the maximum compressive pre-strain was taken as $\varepsilon_{pre} = -0.43$,

at which ductile cracks were just initiated on the outside of pre-bent specimens. The smallest pre-

strain was chosen to be –0.2. This magnitude corresponds to the ratio of the outer radius to the

inner radius of $R_o/R_i = 1.5$.

(2)   Reversed Strain

Reversed loadings can occur in service or further accidents. To simulate this, the specimens were reverse bent. The transition of fracture modes in reverse straining is described in terms of the reversed strain to fracture. Cleavage fracture may occur at a very small reversed strain of ε_{revf} = 0.01. The maximum value of the reversed strain was taken as ε_{rev} = 0.4. Beyond that, micro-ductile fracture or fatigue turn out to become predominant. Also since the specimen is straightened and subjected to tension rather than bending, there is an upper limit by the jig.

4.3   Other Conditions

(1)   Surface Conditions

Since the cleavage fracture in bending starts on or very near the surface, the cleavage transition is sensitive to the surface condition. The as-rolled surface is covered with a smooth oxidized scale but it can be easily removed by scratching or tapping with a hard tool. Under the scale, the metallic surface is rough and sandy at a scale of tenths of millimeters.

The machined surface was produced by good machining practice. To compare the two surface conditions without any other effects, as-rolled and machined specimens were taken the same 254 mm square plate.

(2)   Range of Temperature

With lower temperature, the possibility of cleavage in reverse bending increases. The temperature during both the pre-bending and reverse bending can influence the cleavage condi-

tions in the reverse bending. In an icy ocean, the temperature of seawater can cool down to about

0 °C. The steel used for ship structure above the waterline could be exposed to temperatures as

low as –40 °C. This lowest temperature, –40 °C, is used for Charpy V-notch requirements in any

ABS and ASTM standards, and is likely to be the lowest temperature in service. However, to

reduce the number of parameters in the test and to focus more tests on the pre-strain and on the

reverse bending temperature, the temperature in the pre-bending was chosen to be constant at

room temperature. In the reverse bending, the range of temperature was set to be a room tem-

perature down to –40 °C.

(3)   Aging

Aging is another important factor that decreases the ductility. Aging would also affect the

hardness and the yield strength. To study the aging effect, the coupons mentioned in Section 4.1

were compressed in the long transverse direction of the plate (the long direction of the bending

specimens) by strains of –0.1 and –0.5. After compression, the coupons were aged for 2 to 744

hours at room temperature and the Rockwell B hardness was taken again. Since the aging effects

are possibly observed most on the initial yield strength, modified Rockwell superficial hardness

tests were also carried out. A 0.5 inch ball indenter was used instead of the 1/16 inch for the

standard Rockwell superficial hardness. The ball indenter was pushed against the material so

lightly that the material around the contact portion barely reached yield. From the both Rockwell

B and large-ball 30 kg superficial hardness tests of Figures 14 and 15, no significant room

temperature aging effect was found. For consistency of any aging effect, however, a constant

period of one day was employed for aging for each bent specimen between the pre-straining and

the reverse straining. The details of the test are reported in Appendix G.

(4)   Strain Rate

According to MacGregor and Fisher (1946), the effects of temperature and strain rate on the

flow stress-strain relationship can be correlated with

$$T_m = T\left(1 - \alpha \ln \frac{\dot{\varepsilon}}{\dot{\varepsilon}_0}\right) \quad \text{where} \quad \dot{\varepsilon}_0 = 10^{-3}/\text{sec}, \quad \alpha = 0.018 \tag{4.3}$$

For example, a factor of a hundred times greater strain rate corresponds to approximately a

24 °C reduction from room temperature and a corresponding change of flow stress. Therefore,

the strain rate is another important factor that can affect the bending strain history. In actual

accidents, the strain rates for bending deformation may range from 10^{-3} to 10 sec^{-1}. In these

tests, $d\varepsilon/dt = 10^{-3}$ sec^{-1} was used for both pre-straining and reversed straining.

In applying the results to service conditions with strain rates of perhaps 0.1 sec^{-1}, appropri-

ate corrections to the transition behavior should be made.

5.   Reverse Bending Tests

As described in Section 4, the variables: surface condition, amount of pre-bending, and

temperature of reversed bending determine the amount of reversed bending before cleavage or

any micro-ductile fracture. The apparatus, procedure, and results are described in this section.

Further details are give in Appendix I.

5.1   Apparatus

Three stages shown in Figure 5 consist of a) initiating the pre-bending in a 4-point fixture,

b) completing the pre-bending at room temperature in an end-loading fixture, and c) reverse

bending at a low temperature in the end-loading fixture.

a) 4-point bending (Figure 5a)

The 4-point bending setup bends the specimens up to an angle of about 40° for the subse-

quent end-loading. A pure bending moment is applied in the thinned region without damaging

the test surface. The four loading supports were cylindrical rods of 25.4 mm diameter in half-

bearing blocks. The lower supports were pushed up by a 90 kN Instron hydraulic testing ma-

chine. The distance of the upper rods was 60 mm, and the moment arm to the middle part was 55 mm. Since there was no difference found in preliminary bent specimens for the same head displacement with and without lubrication at the contacts between the rods and the specimens, no lubricant was used.

b) End-load pre-bending at room temperature (Figure 5b)

The end-loading configuration consists of a pair of attachments that linked both ends of the specimen to the loading head of the hydraulic testing machine.

c) End-load reverse bending at low temperature (Figure 5c)

The low temperature reverse bending was done with a 100 kN Instron screw driven testing machine with a temperature-controlled chamber. The internal dimension of the chamber was 560 mmH × 400 mmW × 400 mmD with a 350 mmH × 125 mmW window for observing cracks. The bent specimen was pinned at both ends to the attachments to the loading rods into the chamber. The low temperature inside the chamber was automatically controlled to within ±2 °C, from ambient to –150 °C, by liquid nitrogen and forced gas convection.

5.2   Procedure

Before pre-bending, a strain gauge mark shown in Figure 16 was drawn on the outside of the center of the bend specimen with blue resinous paint.

The bending specimen was bent first up to the angle of $\beta = 40°$ ($\theta = 140°$ in Figure 7) in the 4-point bending fixture. The machine head traveled at a speed of 10 mm per minute, which corresponded to an average strain rate of $d\varepsilon/dt = -0.001$ sec^{-1}. After that, the specimen was bent in the end-load configuration up to the angle of 80° to 130°, which gives the planned compressive strain at the inside of the bent specimen according to Equation (3.4) in Section 3.1. For example,

assuming s_{eff} = 25.4 mm and taking a bend angle β = 130° (θ = 50°) gives the compressive strain

ε_{pre} = –0.43. The machine head traveled at a speed of 10 mm per minute, which corresponded to

an average strain rate of $d\varepsilon/dt$ = –0.0006 sec⁻¹. After the pre-bending, the size of the deformed

strain gauge mark was measured to calculate the pre-strain on the outside surface.

The reversed bending of Figure 5c was carried out one day after the pre-bending. During

cooling, a tension between the two pins was kept at or below 0.7 kN to hold the specimens snug.

After the atmosphere inside the chamber reached to the set temperature, the temperature was held

for 60 minutes before the reverse bending. For the study of temperature equilibration inside the

specimen, refer to Appendix J.

After the chamber temperature equilibration, the specimen was extended at 10 mm/min,

which corresponded to an average strain rate of $d\varepsilon/dt$ = 0.0009 sec⁻¹. The load and extension

were recorded. The extension was continued until one of the two events: cleavage or the load of

22 kN as an upper limit by the jig due to possible tension effects (mean stress 10 % of the tensile

strength). Cleavage was shown by a large noise and a drop of the load. The reversed strain to

fracture was calculated from the pin separation at cleavage by Equation (3.13).

5.3   Results

After the pre-bending, the strain gauge marks on the outside (Figure 17) and the central

plate thicknesses were measured.

Pre-strains on the outside were plotted on Figure 9 to support the theoretical estimates and

FEM results. At the bend angle of 130°, the transverse strains were –0.05 ± 0.10 (20 to 1 odds)

compared to the longitudinal strains of 0.43 ± 0.05 (20 to 1) for the points in Figure 9. This

confirmed the aspect ratio of the net cross section chosen in Section 4.1 for plane strain at the

center.

The plate thickness measured from specimens with a machined surface increased about 1.5 percent for the largest pre-bending of 130°. This is consistent with the constant thickness of bent plate described in Section 3.1 for non-hardening material. However, since the magnitude of the nominal bending strains is proportional to the current plate thickness, measured thicknesses after pre-bending were used for the reported pre-strains for the purpose of the strain definition consistency.

Because of the limited number of specimens, first the reverse bending temperature and then the pre-strain was varied while the other was taken to be constant. The temperatures on reverse bending of –20, –25, –30 and –40 °C were used for a constant pre-strain of approximately –0.43, and the nominal pre-strains of –0.2, –0.3, –0.35 and –0.43 were chosen for a constant reverse bending temperature of –40 °C. Precise results are shown in Table 2.

(1)   For Constant Pre-strain of –0.43

For the constant pre-strain of –0.43, the reversed strains to fracture ε_{revf} were plotted in Figure 18 as black circles versus the temperature on reversed bending. For –40 °C, cleavage fractures occurred with reversed strains ε_{revf} = 0.113 or less, and as low as ε_{revf} = 0.014. Below –30 °C, cleavage fractures occurred with reversed strains ε_{revf} = 0.209 or less, and as low as ε_{revf} = 0.011. For –20 °C, it was ε_{revf} = 0.25 or more. When a specimen was reverse bent at room temperature, it did not cleave with ε_{rev} = 0.265, which is also plotted on Figure 18. Although the data shows some scatter, there is a strong tendency for higher reversed strain to fracture at higher temperature.

The fracture strains for the specimens with a machined surface were also plotted in Figure 18, as black triangles. The temperature dependency was weak, and the reversed strain to fracture

ε_{revf} was almost constant at $\varepsilon_{revf} = 0.34$ over the temperature of -40 to -20 °C, while that for the as-rolled surface depended strongly on the temperature.

(2) For a Constant Reversed Straining Temperature of -40 °C

For the constant reverse bending temperature of -40 °C, the reversed strains to fracture ε_{revf} were plotted in Figure 19 versus the pre-strains as black circles. White circles in the figure show that there was no cleavage fracture before the jig limit. Often ductile cracks initiated. While the largest reversed strain to fracture with $\varepsilon_{pre} = -0.43$ was $\varepsilon_{revf} = 0.113$, that with $\varepsilon_{pre} = -0.35$ was 0.253. With $|\varepsilon_{pre}| = 0.3$ or less, no specimen cleaved before tensile loading became appreciable. For example, with $\varepsilon_{pre} = -0.2$, a reversed strain of only $\varepsilon_{rev} = 0.087$ was applied before the tensile load exceeded 22 kN (a nominal mean tensile stress of 10 % of the tensile strength). Any cleavage occurred at 16 kN or less.

(3) Other Observations

The as-rolled surface was initially covered with a smooth oxidized scale. During pre-compression of the as-rolled surfaces in bending, the scale came off and a black rough surface appeared, with a waviness on the order of 0.5 mm, and sometimes folds between the waves. Apparently some scratches from a previous roll pass became intensified. When machined sur-faces were similarly compressed, tiny wrinkles grew and the surface became rough on the scale of the grain size. On the tensile side, machined sides of all specimens, the surface became dim and rough on the scale of the grain size, and at $\varepsilon_{pre} = -0.43$, short tensile cracks sometimes appeared.

When the cleavage fracture on strain reversal below $\varepsilon_{revf} = 0.06$ occurred on as-rolled surfaces at low temperatures, only tiny folds were visible before the main fracture. At higher

temperatures, with larger ε_{revf}, a number of V-shaped grooves up to 0.5 mm wide formed. Some of these developed micro-ductile cracking from their roots.

Figure 20 shows the load-displacement curves in the end-loading configuration for reverse bending after $\varepsilon_{pre} = -0.43$ and different temperatures. All the curves for the specimens with an as-rolled surface were almost superposed with different fracture points. The upward curvature of the curves in the later half was caused by the geometric effect of the bent specimen. The tensile load for the specimen with a machined surface was 4% larger than that with an as-rolled surface. This was caused because the net thickness of the specimen excluding the oxidized scale was approximately 0.2 mm less than the initial total thickness of 9.525 mm, while the specimen with a machined surface had a net thickness of 9.525 mm.

Figure 21a shows a crack surface which was subjected to $\varepsilon_{pre} = -0.43$ and cleaved at $T_{rev} = -40$ °C giving $\varepsilon_{revf} = 0.019$. Both ends of the crack surface were curled up by the 3-D effect of plate bending, but the central part remained almost flat. The cleavage crack spread over the entire cross section with only a slight ligament on the outside of the bend. There was no initial ductile crack observed at the initiation point on the inside. On another sample of a crack surface in Figure 21b of a specimen that was subjected to $\varepsilon_{pre} = -0.43$ and fractured at $T_{rev} = -20$ °C giving $\varepsilon_{revf} = 0.265$, there were initial micro-ductile wedge openings about 0.2 mm deep on the inside surface prior to cleavage fracture, but with no micro-ductile ligament on the crack surface (Similar sliding-off phenomena can occur in striations at the tips of fatigue cracks, McClintock, 1997). The cleavage in Figure 21b occurred at a higher tensile load. The higher load produced complete cleavage with no remaining ligament.

In a preliminary reverse bending test conducted in room temperature, one specimen with $\varepsilon_{pre} = -0.44$ did not cleave during the first reverse bending up to $\varepsilon_{rev} = 0.27$, but did during the second. Thus, cyclic straining can also cause cleavage even at room temperature. See Appendix I

for details.

6. Discussion

6.1 General

Specimens with as-rolled surfaces and large pre-strains at room temperature cleaved with

very small reversed strains ε_{revf} at low service temperatures. The cleavage transition depends on

two variables rather than just on the temperature as in the Charpy test. In particular, at -30 °C or

lower and $\varepsilon_{pre} = -0.43$, cleavage sometimes only required $\varepsilon_{revf} = 0.011$, but the ε_{revf} rose

abruptly with either less $|\varepsilon_{pre}|$ or higher temperature: First, from Figure 18 at $\varepsilon_{pre} = -0.43$, as the

temperature T_{rev} increased from -40 to -20 °C, ε_{revf} increased from $0.014 \sim 0.11$ to $0.25 \sim 0.27$.

Second, from Figure 19 at $T_{rev} = -40$ °C, when $|\varepsilon_{pre}|$ was decreased from 0.43 to 0.35, ε_{revf}

increased from $0.014 \sim 0.11$ to $0.055 \sim 0.25$.

In Figure 18 for the constant pre-strain $\varepsilon_{pre} = -0.43$, all the reversed strains to cleavage

measured here for the as-rolled surface are included within the two lines:

$$\varepsilon_{revf} = 0.0125\, T_{rev}\,(°C) + 0.625$$
$$\varepsilon_{revf} = 0.0235\, T_{rev}\,(°C) + 0.706 \qquad\qquad (6.1)$$

For higher T_{rev}, higher ε_{revf} is required until the jig reaches its limit, roughly in equation from

$\varepsilon_{revf} = -1.23\varepsilon_{pre} - 0.154$ from Figure 19, or the fracture mode changes from cleavage to micro-

ductile cracking. Since there is no cleavage fracture on reverse bending at room temperature, there should also be another limit of crack free deformation between $T_{rev} = -20$ and 20 °C in this test.

In Figure 19 for the constant temperature on reverse bending at $T_{rev} = -40$ °C, there is a clear limit between $\varepsilon_{pre} = -0.35$ and -0.3. For cleavage fracture shown as black circles, there was a very small or no initial ductile crack. After cleavage, an uncracked ligament was observed on the fracture surface, as shown in Figure 21. White circles in Figure 19 show that no cleavage cracking occurred before the bending was stopped due to the jig limit. If the reversed bending were continued in the 4-point fixture and a hole growth fracture occurred, there will be a fracture appearance transition.

The data in Figures 18 and 19 are replotted in a 3-D space in Figure 22. The two contoured curved surfaces show the upper and lower limits of the locus that includes all the cleavage results for the as-rolled condition.

The bottom region of the lower limit, $|\varepsilon_{pre}| > 0.4$ and $T_{rev} < -30$ °C, should be noted. To prevent premature cleavage after an accident subjected to structural members made of AH36, this region of the locus should be avoided because a reversed strain of only the order of 0.01 could cause cleavage. As a second example, if the structural member were subjected to pre-strain as high as -0.43 and a reversed strain of 0.2 were anticipated, the structure should be used at a -20 °C or higher temperature.

6.2   Expanded Concept of Cleavage Transition

Traditional fracture transitions such as Charpy V-notch work, crack surface appearance, % ferrite grains with micro-cleavage, reduction in area and fracture stress have been expressed in

terms of test temperature. In a design to prevent reverse bending cleavage, some of the above

independent transition variables are not possible or appropriate. The reversed strain to fracture is

appropriate and useful for design analysis. Suppose the cleavage transition is defined at $\varepsilon_{revf}=$

0.2 in the second example above. On a plane of $\varepsilon_{revf}=$ 0.2 from Figure 22, the cleavage transition

band for temperature and pre-strain in Figure 23a is obtained. Similarly, Figure 23b is obtained

for $\varepsilon_{revf}=$ 0.01. The plots of Figure 23 are an expansion of the concept of cleavage transition

from a linear range of temperature to a two-dimensional range of temperature and pre-strain. This

transition band obtained here is for AH36 steel with a reverse strain rate of $d\varepsilon/dt = 10^{-3}$ sec^{-1} at a

pre-bending temperature of T_{pre} = 20 °C. On Figure 23b, the result (ε_{pre} = –0.43 at T_{rev} = –27 °C)

obtained quasi-statically for ABS-B steel by Dvorak and Mylonas (1968) appears beside the

band for the AH36 steel. Actually, their 25.4 mm by 19.05 mm deep cross sections of bent plate

did not remain as flat as shown in Figure 21, i.e., the plane strain condition was not well

satisfied. Therefore, their equivalent transition pre-strain might be more than that of the plate

bending in plane strain. If such bands (Figure 23) were available for several steels and

conditions, the bands closer to the left bottom would indicate tougher behavior against reversed

bending.

The toughness or brittleness of a material is often based on Charpy V-notch work. Dvorak

and Mylonas reported a 20 J Charpy work transition temperature T_{CVN} and a reverse bending

cleavage transition temperature T_{RBC} with pre-strain ε_{pre} about ABS-B steel, as shown below.

	ABS-B	AH36(this work)
20 J T_{CVN} (°C)	–12 to –8	6
$\varepsilon_{revf}=$ 0.01 T_{RBC} (°C) ($\varepsilon_{pre}=$ –0.43)	–27	$\leq$ –30

Supposing that the lower probability limit of cleavage in Figure 22 about AH36 is taken as a cleavage transition curve of AH36, a ε_{revf}= 0.01 T_{RBC} can be obtained, as shown in the table above. Note that Dvorak and Mylonas gave their ε_{revf} of approximately 0.01. Judging from the T_{CVN}, the modern AH36 steel has less ductility. Judging form the T_{RBC} and ε_{revf}, it has more ductility. This comparison illustrates an important fact that, to predict a cleavage transition temperature in reverse bending for the practical application, the reverse bending test is essential and much closer to actual application.

6.3 Machined vs. As-rolled

The machined surface gave very different cleavage conditions from the as-rolled, as shown in Figure 18. Even with a high pre-strain as high as ε_{pre} = –0.43, the specimens required a reversed strain of at least ε_{revf}= 0.33. The reversed strain ε_{revf} for the machined surface was almost constant over the temperature of –40 to –20 °C, while that for the as-rolled surface depended strongly on the temperature. For higher temperatures, the fracture points for the machined surface presumably would join to the band for the as-rolled surface if the jig allowed further reverse strains. They would no longer be premature cleavages, however. With ε_{pre} = –0.43 and at T_{rev} = –40 °C, the machined surface gave 30 times the reversed strain for cleavage of the as-rolled conditions. This result is similar to that of Dvorak and Mylonas (1968). This implies that machining the surface of a specimen can obscure a premature cleavage fracture in an as-rolled plate. A serious risk is hidden in the use of machined specimens to predict cleavage in bending of plates.

Machining the inside surface after bending also remarkably improves the toughness

(Dvorak and Mylonas, 1968). However, it is almost impossible to machine the inside surface of bent plate on actual damaged structures. Machining, better rolling finish, chemical treatment, or shot peening in advance are possible methods of improving the toughness of plates that may be subjected to accidents or explosions.

6.4   Implications for Other Conditions

Effect of Pre-strain Temperature

From MacGregor and Fisher (1946) for annealed 1020 and 1045 steels, stresses for the same strain change approximately by -1.24 MPa/°K in the range of $T = -100$ to $+75$ °C and $\varepsilon < 0.6$. The change of temperature in pre-bending causes different stress levels, but no different strain concentrations, for the same pre-bend angle in the specimen. The plastic flow strength of the material hardened in the lower temperature would be increased higher than that in the room temperature. The increase of plastic flow strength in the subsequent reverse bending would amplify the stress field for the same reverse strain, which would cause more likelihood of cleavage according to Davidenkov theory. Although the transition pre-strain of as-rolled ABS-B steel bars rose from $-\varepsilon_{pre} = 0.24$ at $T_{pre} = 288$ °C to 0.43 at 21 °C (Mylonas 1968) as mentioned in Section 2.3, this tendency cannot be applied for all the range of temperature. To enhance the applicability of the reverse bending cleavage transition, further studies for the relation between T_{pre} and ε_{revf} is required.

About Other Steels

The transition of cleavage on the reverse bending uncracked plate depends on various

material properties and parameters such as chemical composition, grain size, micro-structure, and heat history. It also depends on the structural conditions such as plate thickness, width, plane strain conditions, and welding. If details of the cleavage mechanism were understood and quantitative prediction methods based on metallurgical variables were established, conceivably the transition characteristics of various other steels could be predicted. Until then, for the present structural applications of steel plates in which large bending deformation followed by reverse bending is anticipated probably by accidental events, the author strongly recommends that the individual reverse bending tests with the steel plates be carried out. The conclusions obtained in this research indicate the expanded concept of cleavage transition regarding with the reverse bent plate using a single type of modern high tensile strength ship steel.

Why Not Compare Reverse Bending with Transition in K_{IC} or J_C?

To discuss the brittle-to-ductile transitions of material, there are several independent methods such as K_{IC} and J integrals. These crack tip analyses are applied to study unstable overall growth of pre-cracked plates. Furthermore, K_{IC} is limited to apply to linear structures with a plastic zone much smaller than the crack length. In plate bending, however, cleavage may start from a nominally smooth surface with fully plastic conditions. The Charpy impact specimens have notches which still give different subsurface conditions from plate bending. However, the Charpy V-notch impact test is the most easy way to be carried out in laboratories and actual industrial sites. Therefore, it is worth comparing the results of the reverse bending cleavage transition with the Charpy V-notch work.

Pre-cracked Surface

If the pre-cracked surface was inside of the bent plate, the crack would be closed during pre-

bending, and the pre-strain field would be the same as the non-cracked surface. The pre-strain on

the crack tip should be considered, and it should be smaller than that on the surface. On reverse

bending, stress and strain concentration would strongly affect the cleavage conditions. The effect

of pre-strain with a crack tip analysis would be necessary.

If the pre-cracked surface was outside of the bent plate, it would be an ordinary crack

opening problem.

6.5   The mechanisms of cleavage on reverse bending

In pre-bending, the surface undulations form on both the outside and inside surfaces (Figure

24), very likely furnishing evidence of shear banding beneath. In reverse bending, the amplified

undulations also indicate shear band action. At the relatively high temperature of –20 °C within

the test range, V-shaped surface grooves are formed, sometimes with cracking from their roots as

seen by a stereo light microscopy at 12X and 70X. At a temperature of –40 °C, the cracking

started even without V-grooving. In either case, observations of the final fracture surface sug-

gested that the cracking started by a hole growth mechanism, and soon changed to micro-cleav-

age. Due to complexity of the problem, the need for specimen testing is emphasized to get design

data.

In the following sections, these mechanisms are discussed further.

Shear bands in pre-bending

In various metal forming processes, bending beyond a certain strain gives a shear fracture

running in from the surface, which arises as follows. During large plastic deformations in plane

strain bending, a non-homogeneous but smoothly varying deformation pattern gives way rather

abruptly to jump discontinuities in the displacement gradients across certain surfaces, while the displacements remain continuous. Regions between these surfaces form narrow shear bands (Figure 25). The deformation within each band is predominantly shear parallel to the interface between the band and the adjacent material. The growth of such shear bands can be an important precursor to a sub-surface initiation of fracture across the bounding surfaces of these shear bands, perhaps in part by a ductile cavity growth process as discussed by McClintock, Kaplan and Berg (1966).

The bifurcation of surface deformation and shear band formation at strains of 0.03 to 0.4, larger for higher strain hardening, have been studied by several researchers. Hutchinson and Tvergaard (1980) assumed deformation theory plasticity with a vertex on the yield surface, and with the a smooth yield surface and isotropic hardening, to predict surface instabilities in mono-tonic plane strain, both tension and compression. Anand and Spitzig (1980) used the flow theory and the deformation theory to predict localized shear bands in plane strain tension and compression. Triantafyllidis, Needleman and Tvergaard (1982) determined numerically the course of shear band development in pure bending for three material models; an elastic-plastic solid with a rather sharp vertex on its yield surface, an elastic-plastic solid with a more blunt vertex on its yield surface, and a nonlinear elastic solid (Figure 26). Becker (1992) used a polycrystalline, poly-slip constitutive model to predict shear localization in sheet bending. Anand and Kalidindi (1994) also used a slip system structure to demonstrate shear band formation in plane strain compression of initially isotropic OFHC polycrystalline copper, which has a strain hardening exponent of approximately 0.3, in contrast to the nearly 0.1 of the above studies.

On both the inside and outside surfaces of the bent specimens reported here, the machined surfaces became dull as the angle of pre-bending increased. The inside as-rolled surface formed undulations visible to the naked eye, parallel to the axis of bending. As Anand and Spitzig (1980)

reported, the material can sustain considerable deformation beyond the point of initiation of shear bands before fracture occurs, especially in compression. In the plane strain AH36 steel specimens reported here, no fracture surface at approximately ±45° to the load axis was found on reversal from compression to tension.

Initial imperfections lead to the development of surface undulations on both the compressive and tensile sides of the bending plate and, simultaneously, shear bands initiate at points of strain concentration induced by these surface undulations. In plate bending, the shear bands must propagate into the plate against an adverse deformation gradient so that the peak straining within the bands always occurs at the free surface. The as-rolled surface has relatively large initial imperfections, and the machined surface also has an initial collection of imperfections perhaps due to grain structures or orientations, even though it looks virtually smooth to the unaided eye. The locations of shear bands are very sensitive to the form of small initial surface imperfections, just as in necking in a bar in tension. The diameter becomes non-uniform before peak load. Even before the first bifurcation point is reached, the surface waves will start to grow. Very little additional overall straining is required to meet the condition for shear band inception in small material regions at the wave bottoms (Hutchinson and Tvergaard, 1980). Strain concentrations due to the initial imperfections induce the shear band initiations, while the growth of shear bands accelerates the plate surface undulations. Also, in the large deformation gradient across the thickness of the bent plate, the intensity of the localized shearing varies considerably along the bands, which often end inside the material.

Bifurcation strain estimate

Hutchinson and Tvergaard (1980) found the bifurcation condition for semi-infinite half space with the deformation theory in terms of true strain, with a power-law hardening exponent

N (<1):

$$\varepsilon_{true}\left[1-\exp\left(-2\varepsilon_{true}\right)\right]=N \tag{6.2}$$

For uniaxial plastic strains larger than 0.002 in the tensile specimens of AH36 steel in this study, the best fit power-law curve yields $N = 0.187$. By (6.2), bifurcation strains in plane strain extension and compression from this power-law exponenet are

$\varepsilon_{true} = 0.363$, $\varepsilon_{nom} = 0.437$ for extension

$\varepsilon_{true} = -0.266$, $\varepsilon_{nom} = -0.234$ for compression

Other researchers, mentioned in the subsection above, did not show quantitative estimates for strains for bifurcation or inception of localization. Their finite element methods have not been used to predict critical strains. The strains for inception of localization obtained above are comparable with the transition pre-strain of $\varepsilon_{pre} = -0.3 \sim -0.35$ at $T_{rev} = -40$ °C in Figure 19.

Shear band deformation on reversal

In reverse bending, shear deformation starts earlier within the former localized shear bands than in the material outside the bands, if the Bauschinger strain increases with pre-strain, and starts forming shear bands. The hardening is higher, however, so the formation of shear bands in the tensile strain field is hard to predict. Further, the direction of the bands is different from the compressive ones: In tension, the angle of inclination of the shear bands to the load axis is approximately ±38° which is less than ±45°, and in compression it is approximately ±55° which is greater than ±45° (Anand and Spitzig, 1980).

In pre-bending, the subsurface shear band localization that concentrates shear strains into a few lines on the surface has a gradient and lies along a curved surface. The enhanced localized normal strain must become much larger than the nominal strain estimated by averaging along the surface. The locally reduced flow strength accelerates grooving on reversal, accompanied with

the strain concentration due to the amplified surface undulation, especially for the pre-compressed as-rolled surface.

V-groove growth on reversal

On the inside surface of both as-rolled and machined specimens that fractured at –20 °C, a number of V-grooves were observed. From observations of the fracture surfaces, cracking appears to initiate at the bottom of one of the grooves. There was no visible V-groove observed on the specimens that fractured with smaller strains at –40 °C. Details of the V-groove growth mechanism are discussed by McClintock (1971, 1999) in terms of the slip planes of non-hardening plasticity that meet at the bottom of the groove (Figure 27). The initiation of the groove by sliding-off occurs more easily with rough surfaces than smooth ones because of the strain concentration. The shear bands discussed above cause enhanced shear deformation and undulation in the compressive strain field on the surface in pre-bending. The formation of V-grooves on the inside surface contributes increasing the fields of high stress and strain below the surface. At the roots of the V-grooves, stable hole growth microcracks initiate and start to grow. The first unstable crack growth is likely to trigger the macroscopic cleavage fracture, as observed through the stereo-microscope.

Initiation of cleavage fracture from surfaces and cracks

Hahn et al. (1959) discussed the details of the cleavage mechanism in unnotched round bar tensile tests on Project Steel E, with grain sizes of 0.106 and 0.041 mm, at temperatures ranging from the ambient to down to –250 °C. On lowering the temperature, the fracture stress and the reduction in area fall abruptly when stabilized cleavage microcracks start to appear in ferrite grains (Figure 28). Most of the microcracks are about the length of the ferrite grains. In this

range of temperature, macroscopic cleavage fracture may occur when a growing microcrack penetrates an adjoining grain and continues to propagate.

The surface subjected to compressive deformation in pre-bending has undulations amplified by shear bands initiated by the surface imperfections. For the smooth machined surface, the wavelength of the imperfection is possibly about the grain size, about 0.07 mm for the AH36 steel. For the as-rolled surface, the roughness consists of a superposition of multiple wavelengths ranging from the grain size to even the circumference of the rolls in the rolling mill. During pre-bending, undulations will become sharper. In reverse bending, respective notches or micro-ductile cracks initiated at the bottoms of undulations or at the roots of V-grooves act like initial cracks in the local monotonic tension field. Thus, the larger initial imperfections form larger initial edge cracks in pre-bending, and subsequently, cleavage fracture occurs more likely in reverse bending. This scenario, based on the ductile-to-brittle transition due to microcrack emergence, accounts for the sensitivity of the cleavage in reversed bending to the surface conditions, and for the scattering of data for the as-rolled surface condition with multiple wavelengths. Clearly, these processes will manifest themselves in somewhat different forms based on the microstructure and surface finish of the steel, but should be present in many cases.

The complexity of the processes of the formation of undulations on the surface and shear banding in sub-surface, of the Bauschinger effect on reversal, and of the initiation and growth of cleavage cracks, necessitates testing specimens with practical surface conditions and strain states to obtain quantitative data for structural design. Such test procedure has been developed in the present thesis.

6.6   Further Studies

The plane strain bending tests on the as-rolled steel surface can outline the fracture locus for reversed tensile strain to fracture for practical applications without converting stress or strain states from machined axial specimens. The effects of more variables, such as strain cycling, strain rate, size, strain distribution, prior cracks, pre-bending temperature, and steels and their micro-structures should be explored. Since a complete locus of reversed strains over all combinations of these effects would require thousands of tests, it is recommended that, as here, only a few traverses be taken for each combination. Furthermore, to reduce the number of traverses, known models should be applied such as used in the study of Charpy transition by Tvergaard and Needleman (2000), the extension to statistical effects by Bernauer, et al (1999), and the study of rate-modified temperature by MacGregor and Fisher (1946). (See also McClintock and Argon, 1999, p191)

7. Conclusions

In many structures, such as in ships being sailed or towed after explosions or groundings, and in pipelines and buildings during earthquakes, there is a need for steel plates ductile enough to survive not only severe bending, but also at least some reversed strain before fracture.

Reverse bending of novel specimens having either as-rolled or machined test surfaces, from the high strength ship steel AH36, showed that:

(1) After large accidental bending, small reversed bending at temperatures that can be encountered in service can give unexpected cleavage fracture even in a modern steel structure.

Specifically, in reverse bending of as-rolled plates pre-strained by $\varepsilon_{pre} = -0.43$ at room temperature, a reversed strain $\varepsilon_{revf} = 0.011$ at -30 °C or lower can cause cleavage. Further, based on the 31 tests reported here, when an accident has subjected structural members made of AH36 to local compressive strains of $\varepsilon_{pre} = -0.40$ or more, either temperature lower than -30 °C or reversed strains higher than 0.01 should be avoided to prevent unexpected cleavage.

(2) In reverse bending, a machined surface may obscure the probability of premature cleavage fracture.

With a machined surface, the reversed strain with $\varepsilon_{pre} = -0.43$ at $T_{rev} = -40$ °C required for

cleavage increased to $\varepsilon_{revf} = 0.33$, from $\varepsilon_{revf} = 0.011$ with as-rolled surface. That is, the

machined surface gave 30 times the reversed strain for cleavage of the as-rolled conditions.

Further, the strain ε_{revf} for the machined surface was almost constant over the temperature of

−40 to −20 °C, while that for the as-rolled surface depended strongly on the temperature.

(3) To predict a cleavage transition temperature in reverse bending for this practical application,

the reverse bending test itself in terms of reversed strain to fracture is essential.

In a similar bending test on ABS-B steel with the same pre-strain, Dvorak and Mylonas

(1968) found the same transition temperature $T_{RBC} = -27$ °C for a reversed strain to cleavage

of $\varepsilon_{revf} \sim 0.01$ as here for $T_{RBC} \leq -30$ °C. However, the Charpy V-notch transition temperature

was much higher for AH36: $T_{CVN} = 6$ °C for AH36 to −14 °C for ABS-B. AH36 appears more

ductile in reverse bending, although less in Charpy work, than ABS-B. For the reverse bend-

ing cleavage, the plate bending tests rather than Charpy V-notch tests are essential.

(4) The fracture mode transition must be expanded from one independent variable (temperature)

to two: temperature and pre-strain.

Traditional fracture transitions have been expressed in terms of temperature. In reverse

bending cleavage, the transition is expressed in terms of not only on temperature but also on

pre-strain. That is, the concept of cleavage transition must be expanded from a point of

temperature to a locus of temperature and pre-strain.

(5) In modern ship steels on reverse bending fracture, the reversed strain to fracture is used as the

dependent variable that undergoes a transition.

Traditional fracture transition parameters have been Charpy V-notch work, crack surface

appearance, % ferrite grains with micro-cleavage, fracture stress, etc. On reverse bending fracture, a transition appeared in the amount of reverse strain to fracture. In older steels, judging from ABS-B, ε_{revf} was negligible.

(6) In the space of pre-strain, temperature, and reverse strain to fracture in reverse bending of as-rolled plates pre-strained at room temperature, there was a 3-D transition locus.

In particular:

at −40 °C and $\varepsilon_{pre} = -0.43$, cleavage required $\varepsilon_{revf} = 0.011$.

The low ε_{revf} disappeared abruptly with either less negative ε_{pre} or higher temperature:

at −40 °C and $\varepsilon_{pre} = -0.35$, cleavage required $\varepsilon_{revf} = 0.25$, and

at −20 °C and $\varepsilon_{pre} = -0.43$, cleavage required $\varepsilon_{revf} = 0.27$.

(7) The hole growth and cleavage fracture mechanisms involved in reversed bending are discussed from the point of view of subsurface deformation, shear band formation, and surface grooving. Quantitative prediction of fracture transitions remains out of reach.

(8) A system for pre- and reversed plane strain bending has been developed, along with approximate relations between testing machine displacement, bend angles, and strains.

The complexity of the mechanisms and processes of cleavage necessitates testing specimens with practical surface conditions and strain states to obtain quantitative data for engineering design. The results generated in this thesis provide a practical method to choose a steel that could withstand anticipated accidental conditions.

References

ABS 1984 Material for hull vonstruction and equipment, rules for building and classing steel vessels, American Bureau of Shipping, Section 43

ANAND, L. AND KALIDINDI, S. R. 1994 The process of shear band formation in plane strain compresion of fcc metals: effect of crystallographic texture, *Mechanics of Materials*, **17**, 2-3, pp 223–243, Mar.

ANAND, L. AND SPITZIG, W. A. 1980 Initiation of localized shear bands in plane strain, *J. Mech. Phys. Solids*, **28**, pp 113–128

ASTM A131/A 131M-96 1997 Standard specification for structural steel for ships, *Annual Book of ASTM Standards*, **01.04**, Jan.

ASTM E112-96 1997 Standard test methods for determining average grain size, *Annual Book of ASTM Standards*, **03.01**, July

ASTM E23-96 1997 Standard test methods for notched bar impact testing of metallic materials, *Annual Book of ASTM Standards*, **03.01**, July

BECKER, R. 1992 An analysis of shear localization during bending of a polycrystalline sheet,

Journal of Applied Mechanics - Transaction of ASME, **59**, 3, pp 491–496 Sep.

BERNAUER, G., BROCKS, W. AND SCHMITT, W.   1999   Modifications of the Beremin model for cleavage fracture in the transition region of a ferritic steel, *Engineering Fracture Mechanics*, **64**, pp 305–325

CLAUSING, D. P.   1970   Effect of plastic state on ductility and toughness, *International Journal of Fracture Mechanics* **6**, 1, pp 71–85

DVORAK, J.   1966   The precompression bending test, *The Welding Journal*, **45**, 5, *Research Supplement*, pp 235s–240s

DVORAK, J. AND MYLONAS, C.   1968   Effect of surface condition on the exhaustion of ductility by cold or hot straining, Ship Structure Committee Report No. SSC-185, July

DVORAK, J. AND VRTEL, J.   1966   Measurement of fracture toughness in low-alloy mild steels, *The Welding Journal*, **45** (6), *Research Supplement*, pp 272s–283s

HAHN, G. T., AVERBACH, B. L., OWEN, W. S. AND COHEN, M.   1959   Initiation of cleavage microcracks in polycrystalline iron and steel, *Proceedings of an International Conference on the Atomic Mechanisms of Fracture*, April, pp 91–116

HALL, W. J., KIHARA, H., SOETE, W. AND WELLS, A. A.   1967   *Brittle Fracture of Welded Plate*, *Theoretical and Applied Mechanics*, Prentice-Hall, Inc., Englewood Cliffs, New Jersey

HAWLEY, R. H. AND DRUCKER, D. C.   1973   Brittle fracture of precompressed steel as affected by hydrostatic pressure, temperature and strain concentration, *Experimental Mechanics*, **13**, 1, pp 1–6

HILL, R.   1950   *The Mathematical Theory of Plasticity*, Clarendon Press, Oxford, pp 287–294

HUTCHINSON, J. W. AND TVERGAARD, V.   1980   Surface instabilities on statically strained plastic solids, *Int. J. Mech. Sci.*, **22**, pp 339–354

LUBAHN, D. AND SACHS, G.   1950   *Trans. ASME*, **72**, 201

LUDLEY, J. H. AND DRUCKER, D. C.   1960   A reversed-bend test to study ductile to brittle transition, *The Welding Journal*, **39**, 12, *Research Supplement*, pp 543s–546s

MACGREGOR, C. W. AND FISHER, J. C.   1946   A velocity modified temperature for the plastic flow of metals, *J. Appl. Mech.* **13**, pp A11–A16

MASUBUCHI, K., MCCLINTOCK, F. A. AND LIANG, L.   1996   *Summary report on welding research from the tanker grounding project*, Joint MIT-Industry Program on Tanker Safety, MIT, Cambridge MA, **56**, June

MCCLINTOCK, F. A.   1971   Plasticity aspects of fracture mechanics, *Fracture*, ed. H. Liebowitz, New York, Academic Press, **3**, pp 47–225

MCCLINTOCK, F. A.   1997   The Paris law for fatigue crack growth in terms of the crack tip opening displacement, *Proc. Prof. P. C. Paris Int. Sympo. on Fatigue of Materials*, The Minerals, Metals and Materials Society, Indianapolis, IN, pp 3–25, September

MCCLINTOCK, F. A. AND ARGON, A. S.   1999   *Mechanical Behavior of Materials, Reprinted with corrections and errata*, Ceramic Book and Literature Service, Marietta, OH

MCCLINTOCK, F. A. KAPLAN, S. M. AND BERG, C. A.   1966   Ductile fracuture by hole growth in shear bands, *Int. J. Fracture Mechanics*, **2**, pp 614–627

MCCLINTOCK, F. A. AND PARKS, D. M.   1999   On predicting the transition in probability of rare cleavage in ductile cracked structures, *Proc. 7th Symposium on Energy Engineering*

Sciences, Argonne National Laboratory, Argonne, IL, May

MYLONAS, C. 1959 Pre-strain, size and residual stresses in static brittle-fracture initiation, *The Welding Journal*, **38**, 10, *Research Supplement*, pp 414s–424s

MYLONAS, C. 1961 Static brittle fracture initiation without residual stresses, *Welding Journal*, **40**, 11, *Research Supplement*, pp 516s–520s

MYLONAS, C. 1964 Exhaustion of ductility and brittle fracture of E-steel caused by pre-strain and aging, Ship Structure Committee Report No. SSC-162, July

MYLONAS, C., DRUCKER, D. C. AND BRUNTON, J. D. 1958 Static brittle-fracture initiation at net stress 40% of yield, *The Welding Journal*, **37**, 10, *Research Supplement*, pp 473s–479s

MYLONAS, C. AND ROCKEY, K. C. 1961 Exhaustion of ductility by hot straining - an explanation of fracture initiation close to welds, *The Welding Journal*, **40**, 7, *Research Supplement*, pp 306s–310s

RIPLING, E. J. AND BALDWIN, W. M., JR. 1952 Overcoming rheotropic brittleness: precompression versus pretension, *ASM Trans.*, **44**, pp 1047–1057

TOYODA, M. 1995 How steel structures fared in Japan's great earthquake, *Welding Journal*, December, pp 31–42

TRIANTAFYLLISIS, N., NEEDLEMAN, A. AND TVERGAARD, V. 1982 On the development of shear bands in pure bending, *Int. J. Solids Structures*, **18**, 2, pp 121–138

TVERGAARD, V. AND NEEDLEMAN, A. 2000 Analysis of the Charpy V-notch test for welds, *Engineering Fracture Mechanics*, **65**, pp 627–643

YAMAMOTO ET AL 1995 Crack initiation strength of structural steel members having experi-

enced large compressive strain due to buckling deformation (1st report, Japanese), *Journal of the Society of Naval Architects of Japan*, **178**, pp 565–573

Figures and Tables

a.   *Extreme loads caused by stranding and by explosion*

b.   *Single reversed strain and cycling strain*

Figure 1   *Examples of Extreme loads and strain history*

Figure 2   NSWC 3-bay grillage model loaded in compression. The panel underwent global buckling associated with local buckling of stiffeners. The model was subsequently loaded in tension to produce tearing.
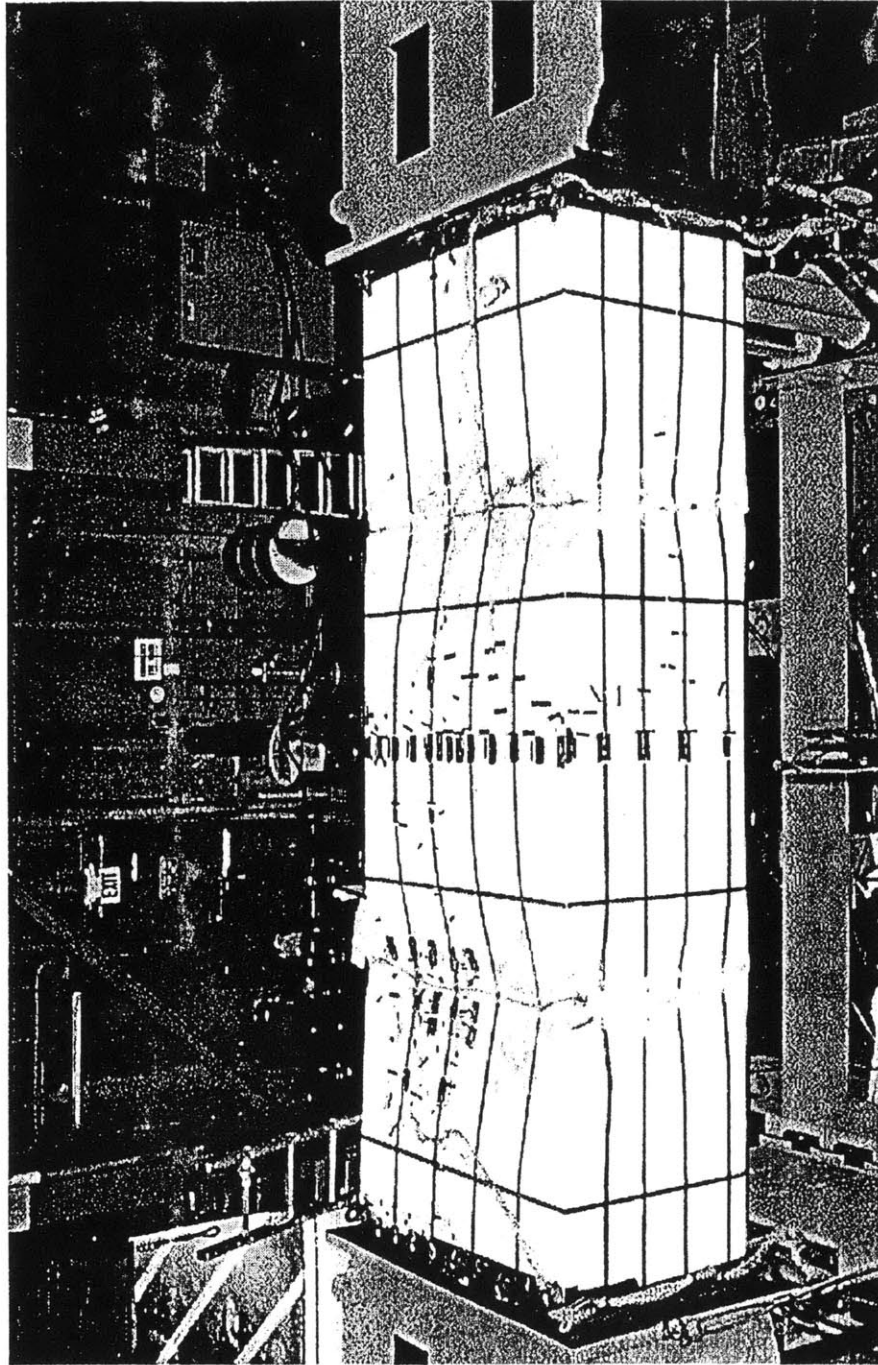
Figure 3   *Box girder representing ship's hull loaded in bending/compression developed fracture at the corners. (Courtesy of NSWC)*
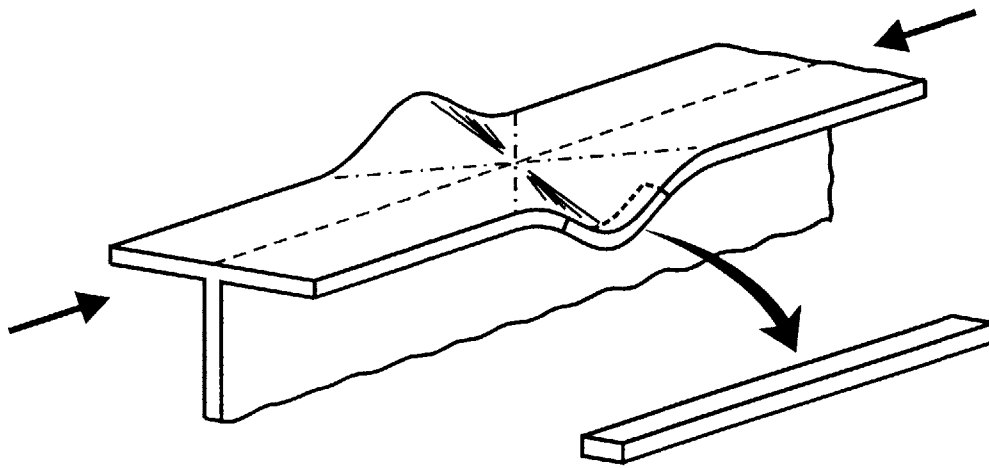
Figure 4   *Local buckling of T-stiffener due to compressive load and an extracted bar specimen with a surface element subjected to compressive strain by bending.*

P, δ ↓

a. 4-point bending

P, δ

b. End-load
bending

P, δ ↑

N₂

Cryogenic Chamber
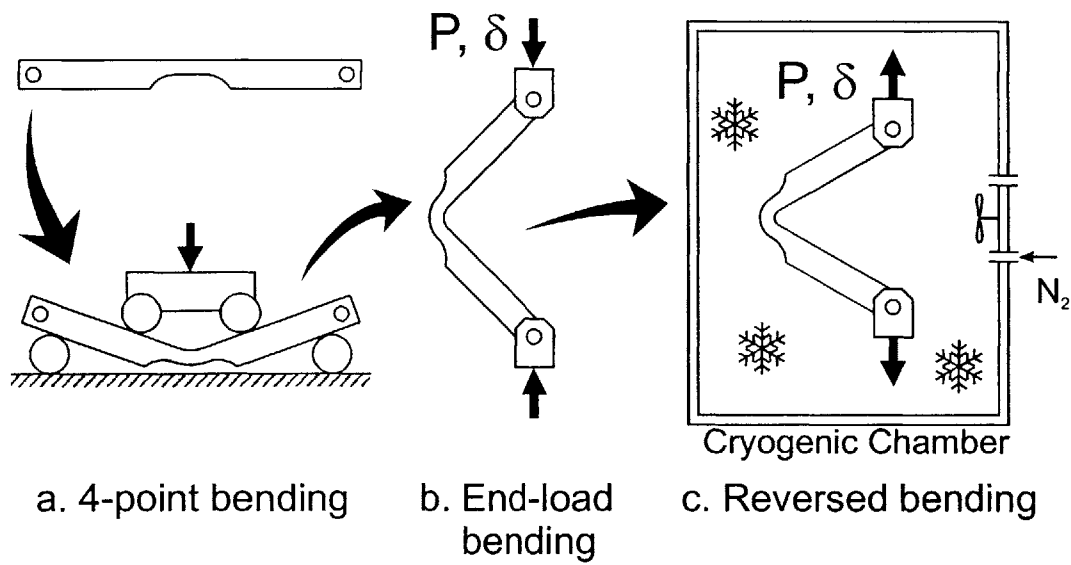
c. Reversed bending

Figure 5 *Reversed bending test procedure: a. 4-point bending, b. end-loading*
bending, c. reversed bending in cryogenic chamber
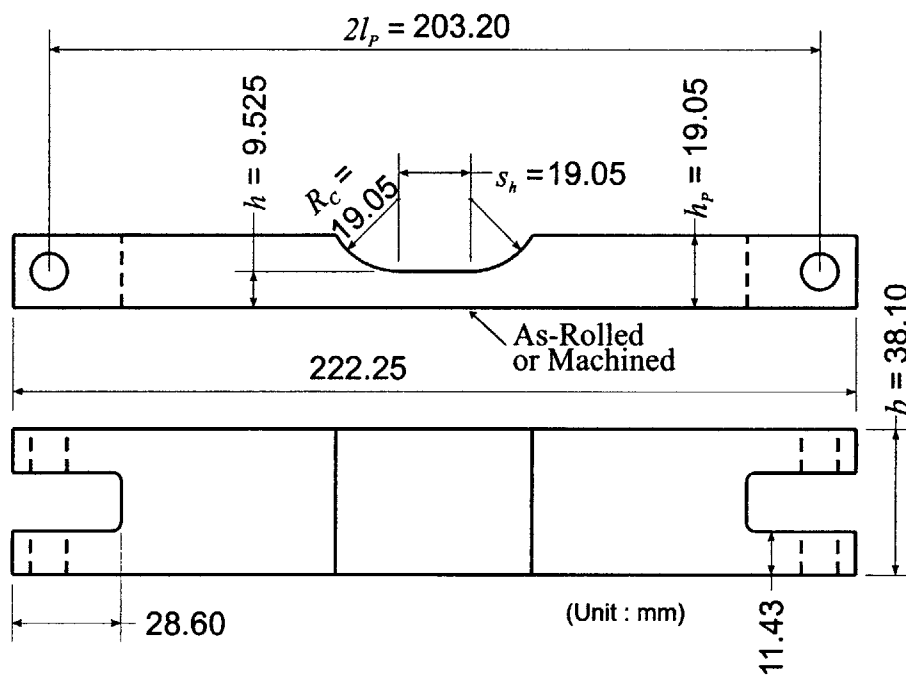
Figure 6　　*Reverse bending specimen with as-rolled or machined surface*
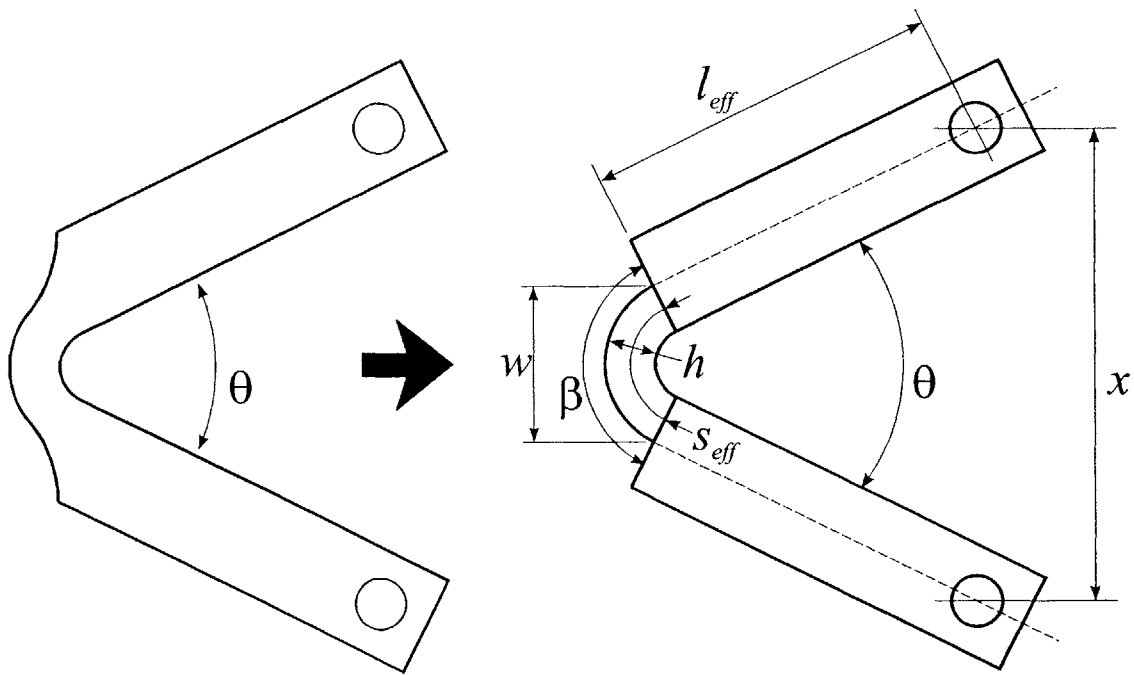
Figure 7   *Reverse bending specimen modeling for relation between bend angle and bending strain*
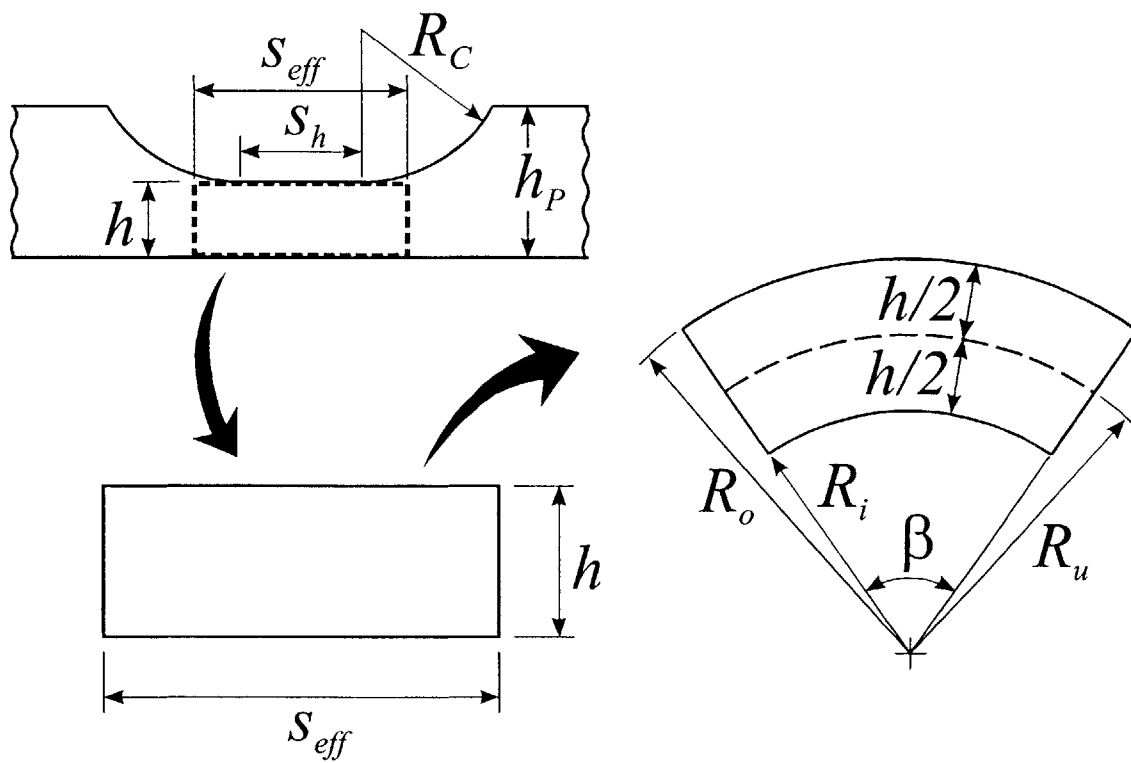
Figure 8   Plane strain bending with effective length s_{eff}
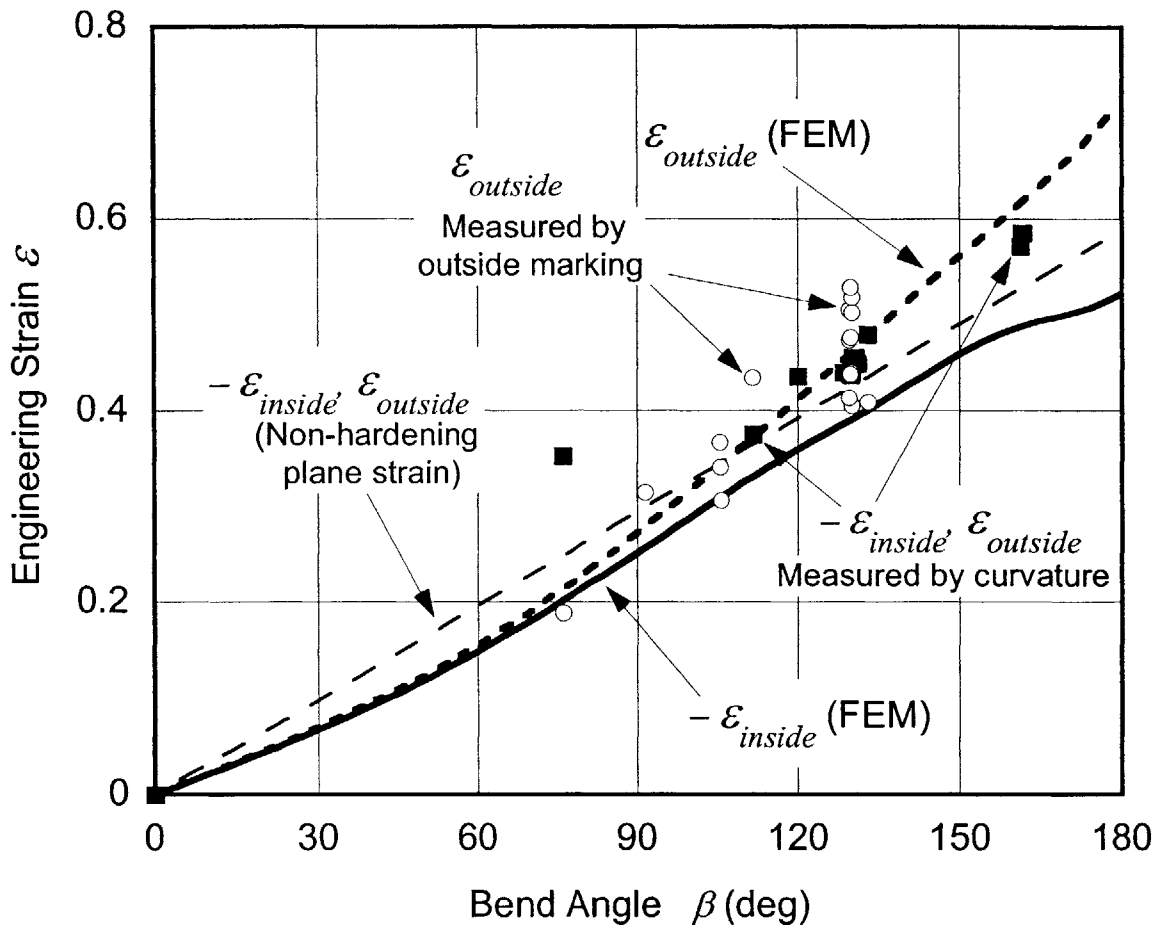
Figure 9   *Comparison of bending strain versus bend angle by theory, FEM, and measurements by outside marking and curvature, h = 9.525 mm, s_{eff} = 25.4 mm*
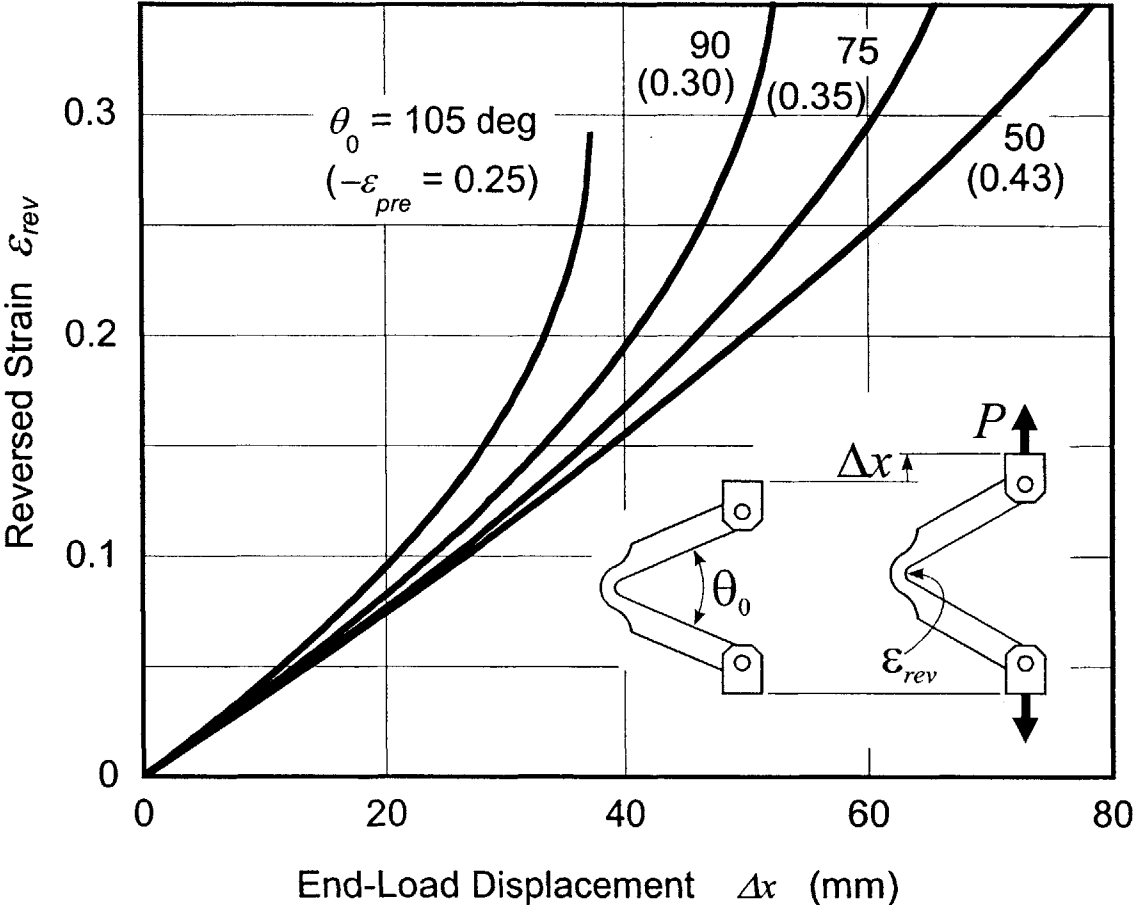
Figure 10   Reversed strain versus end-load displacement, l_{eff} = 90 mm, s_{eff} = 25.4 mm and h = 9.65 mm

Table 1   *Properties and parameters of high strength steel AH36*

Supplier's Data								
Chemical composition, %								
C	Mn	Si	P	S	Cr	Ni	Al	Cu
0.179	1.56	0.441	0.016	0.006	0.03	0.18	0.053	0.153
Ti	N	Nb	V	Mo	Ca	Sn	B	
0.003	0.007	0.003	0.005	0.054	0.0002	0.002	0.0002	

Mechanical Parameters in L-direction (rolling direction)		
Yield Point MPa	Tensile Strength MPa	
380.6	590.9	

Measured Mechanical Parameters in T-direction (long transverse direction)

Yield Point MPa	Tensile Strength MPa	Elong. 2.5 in %	Charpy V-notch(TS) J			ASTM Grain Size No.*1	Plate Thickness mm
			-25 °C	0 °C	25 °C		
322.2	621.1	19.7	9.5	16.6	35.3	5.7	25.4

*1 The ASTM grain size number, G, is defined as $N_{AE} = 2^{G-1}$, where N_{AE} is the number of grains per square inch at 100X magnification.
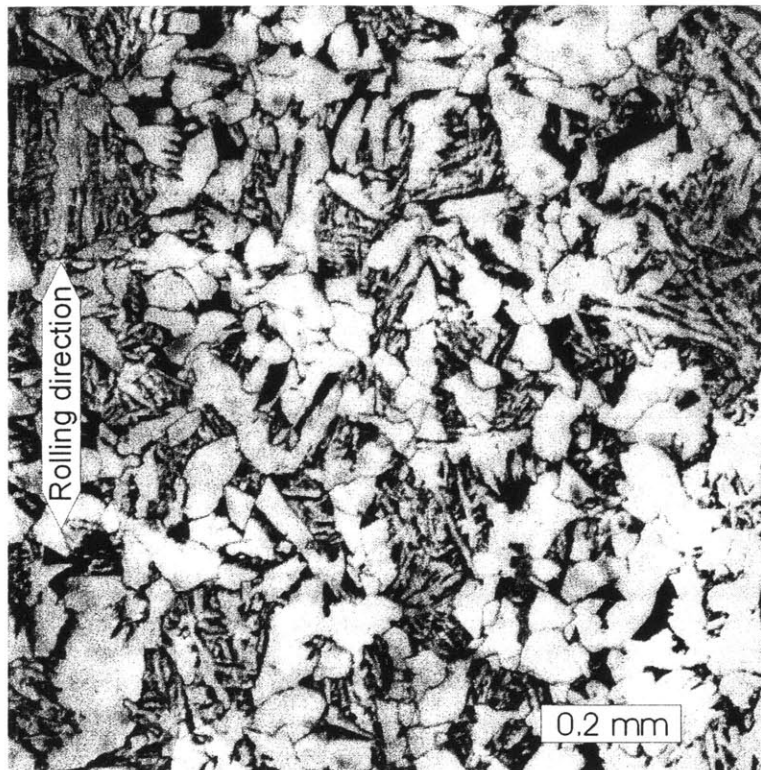
Figure 11   Grain shape of AH36 steel on the plane normal to T-direction
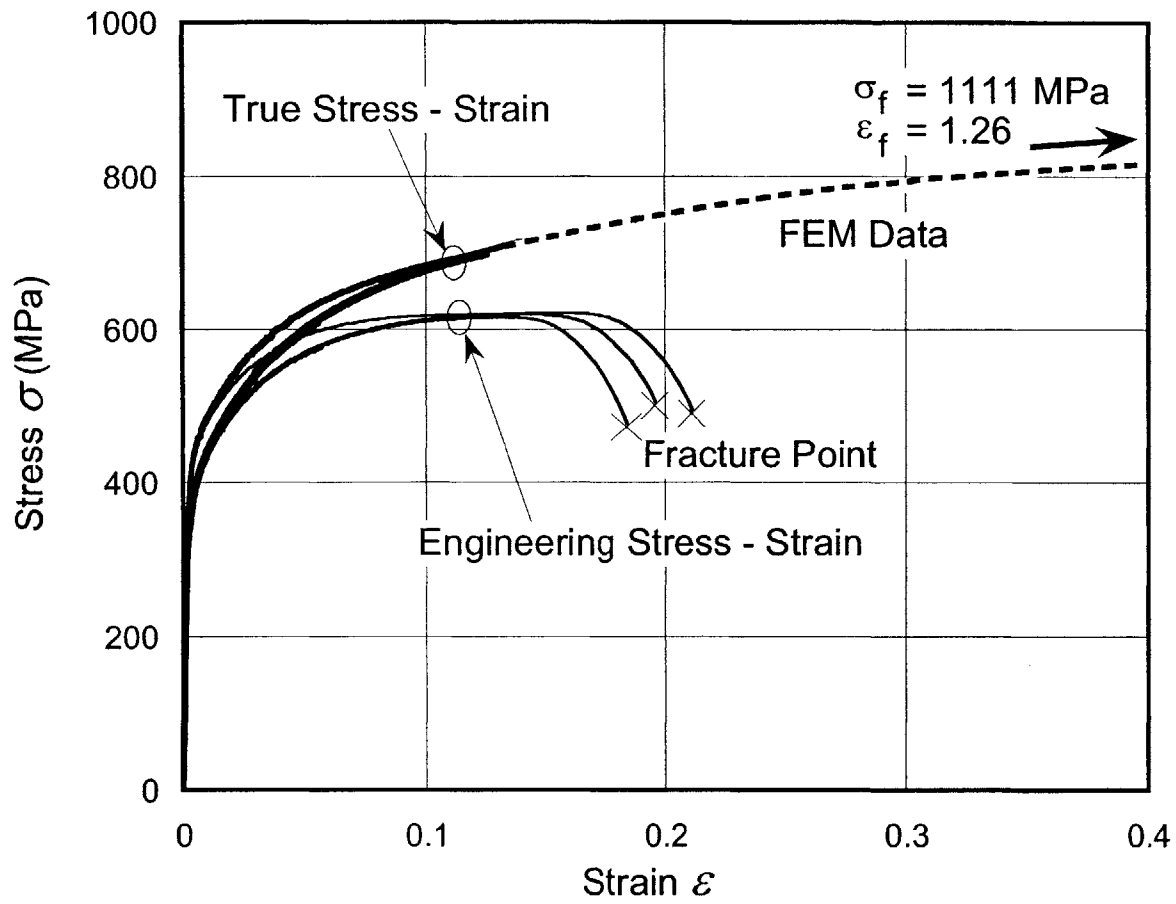
Figure 12   *Stress-strain behavior of AH36 steel from three 1/4 inch diameter and 2.5 inch long specimens*
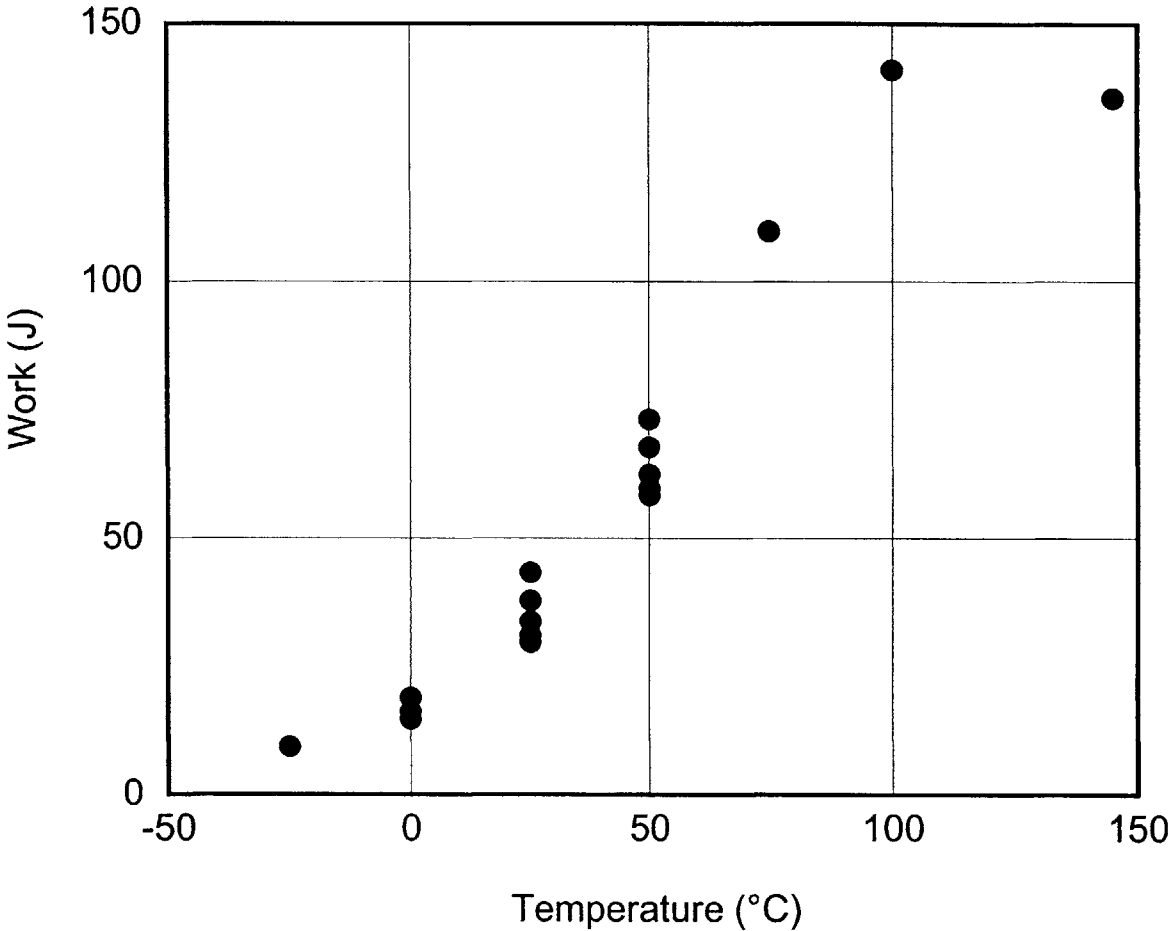
Figure 13   Charpy V-notch tests of AH36 steel using transverse (TS) specimens
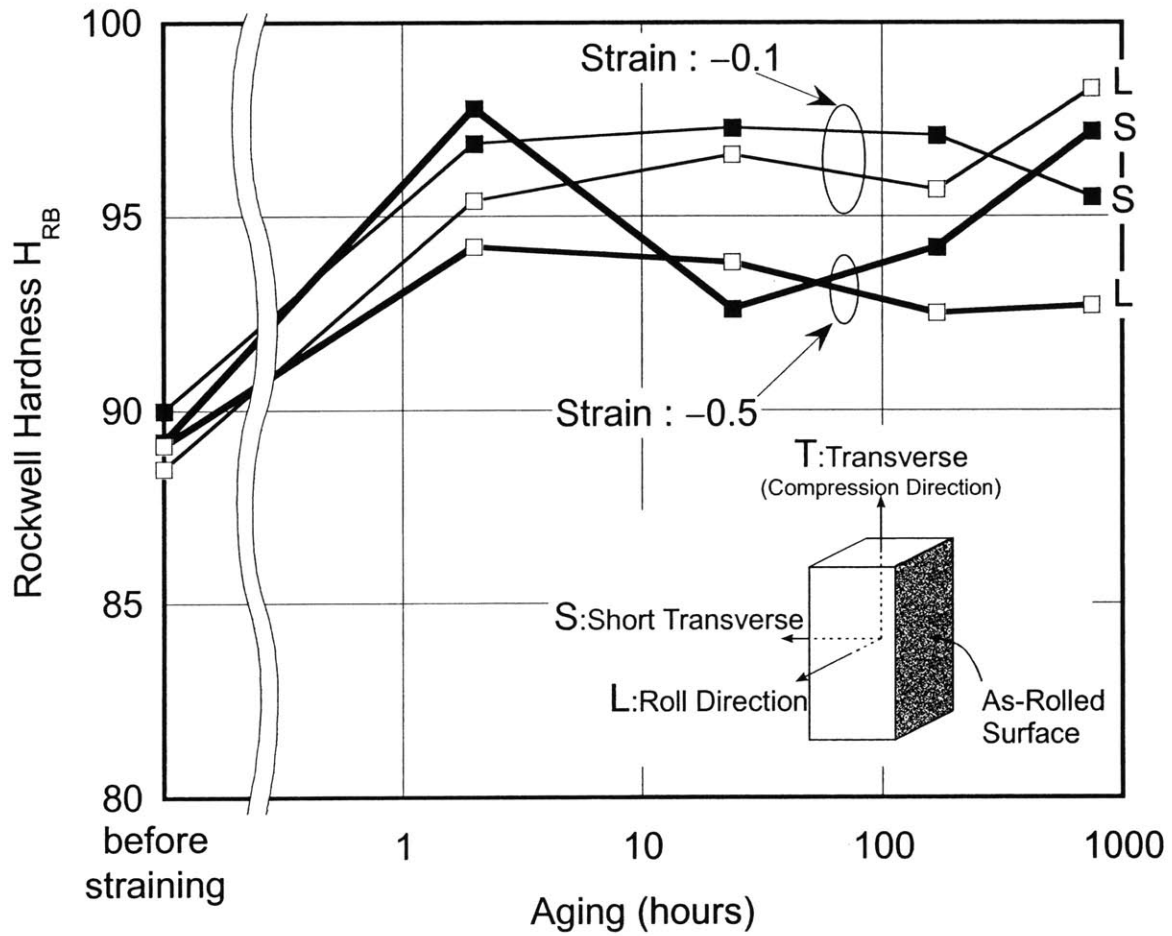
Figure 14   *Aging of Rockwell B hardness of AH36 steel after straining by –0.1 and –0.5 in transverse direction*
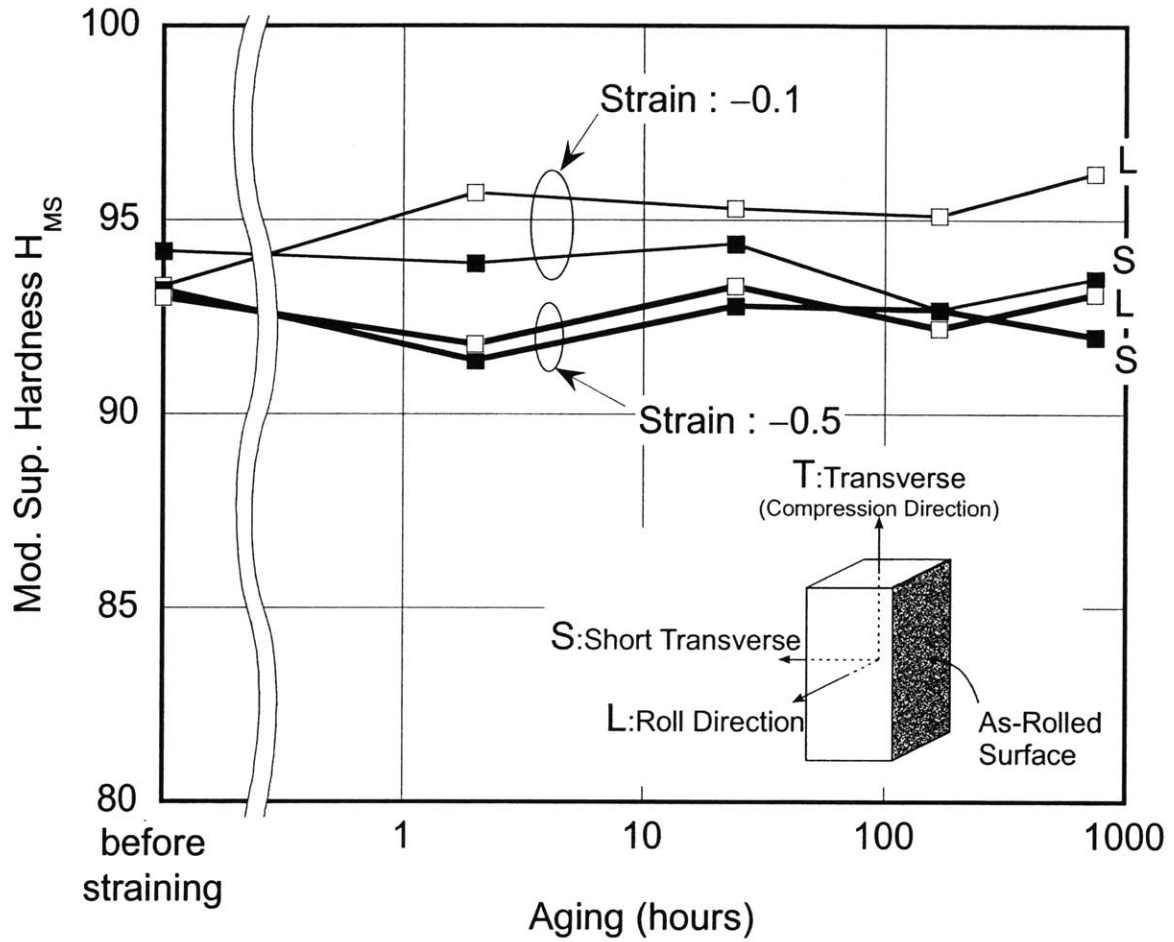
Figure 15 Aging of low-strain modified superficial hardness of AH36 steel after straining by −0.1 and −0.5 in transverse direction
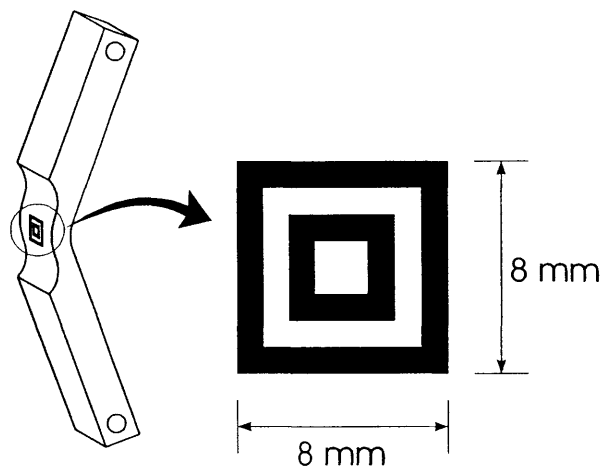
Figure 16   Mark for strain measurement

Table 2   *Details of the reversed bending test results*

Specimen No.	Planned Nominal pre-strain	Engineering pre-strain	Temperature during reversal (°C)	Reversed strain at cleavage	Surface As-Rolled or Machined
7[*1]	-	-0.393	20	0.279[*2]	A
8[*1]	-	-0.248	20	0.094[*2]	A
9[*1]	-	-0.365	20	0.302[*3]	A
10[*1]	-	-0.435	20	0.265[*4]	A
30	-0.20	-0.200	-40	0.087[*5]	A
31	-0.20	-0.203	-40	0.087[*5]	A
34	-0.30	-0.304	-40	0.220[*5]	A
35	-0.30	-0.304	-40	0.155[*5]	A
45	-0.30	-0.302	-40	0.167[*5]	A
32	-0.35	-0.352	-40	0.173	A
43	-0.35	-0.349	-40	0.241[*5]	A
44	-0.35	-0.348	-40	0.055	A
46	-0.35	-0.348	-40	0.254	A
17	-0.43	-0.431	-20	0.252	A
25	-0.43	-0.432	-20	0.265	A
40	-0.43	-0.428	-25	0.303	A
12	-0.43	-0.431	-30	0.024	A
18	-0.43	-0.431	-30	0.011	A
19	-0.43	-0.431	-30	0.013	A
23	-0.43	-0.431	-30	0.011	A
24	-0.43	-0.430	-30	0.017	A
41	-0.43	-0.429	-30	0.209	A
42	-0.43	-0.430	-30	0.092	A
14	-0.43	-0.433	-40	0.113	A
15	-0.43	-0.432	-40	0.049	A
20	-0.43	-0.429	-40	0.014	A
22	-0.43	-0.427	-40	0.019	A
13	-0.43	-0.437	-45	0.039	A
21	-0.43	-0.431	-20	0.354	M
26	-0.43	-0.433	-30	0.338	M
16	-0.43	-0.432	-40	0.328	M

[*1] At end of thinned section, 0.5 mm R corners rather than 19.05 mm R fillets.
[*2] Fractured at fillet on bending after this first reversed strain.
[*3] Shear cracking and instability on second such reversed straining.
[*4] Shear cracking and instability on bending after this first reversed strain.
[*5] Stopped at jig limit (22 kN) before fracture.

Figure 17   *An example of deformed strain gauge mark*
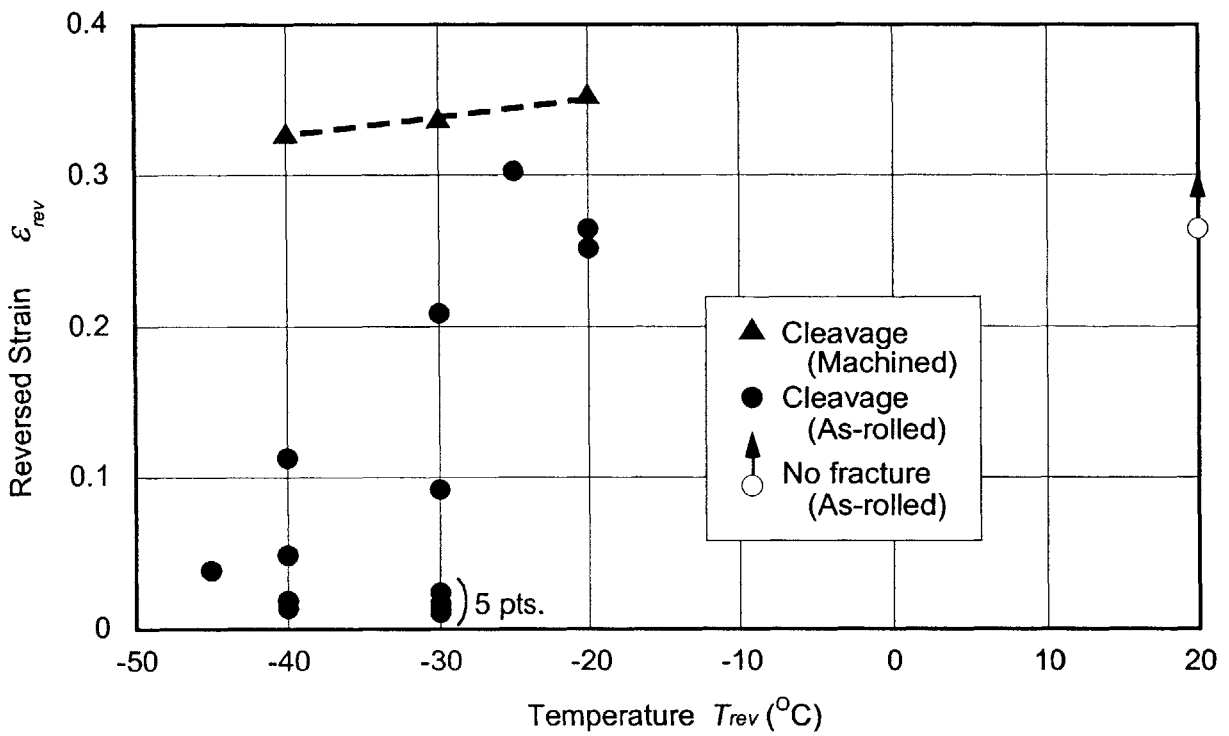
Figure 18   *Reversed strain to fracture versus temperature at reverse bending with the*
                pre-strain $\varepsilon_{pre} = -0.43$
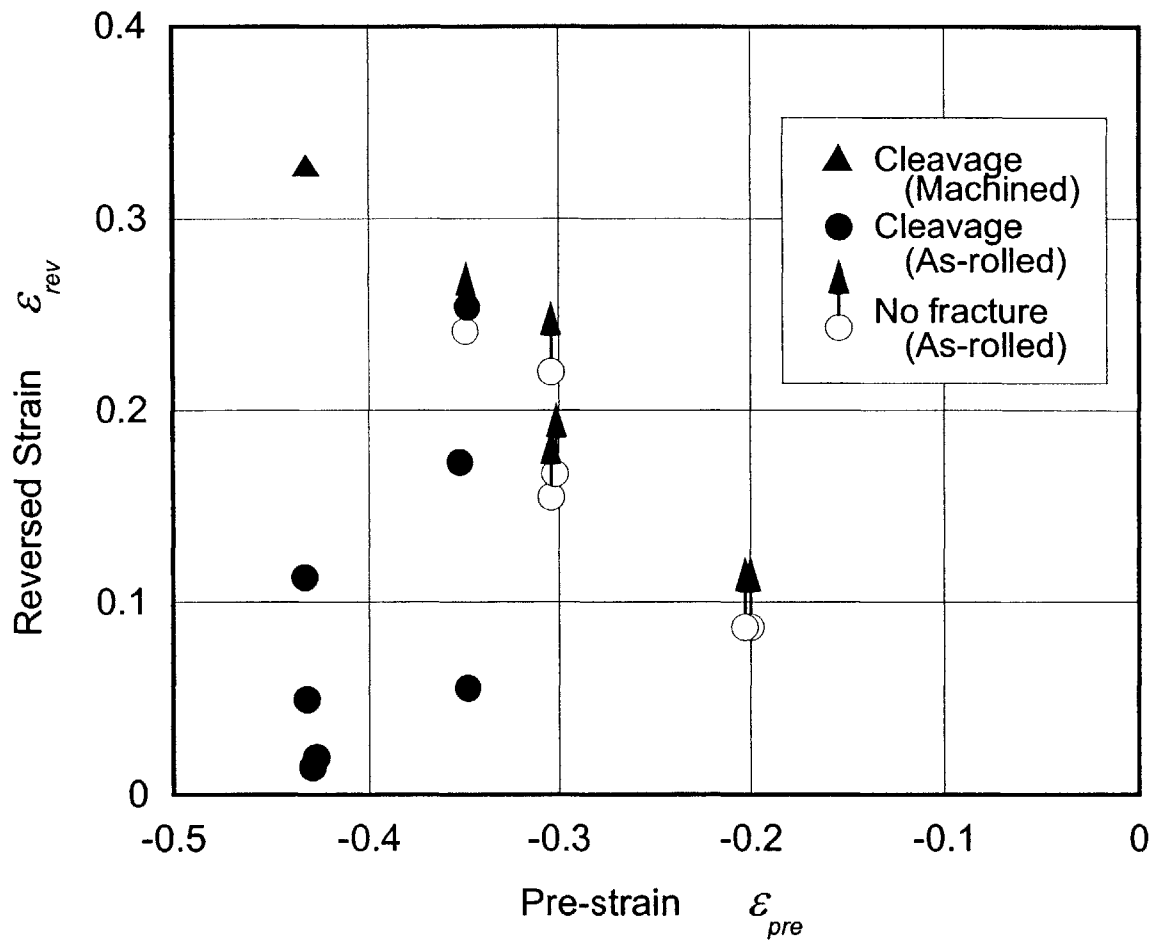
Figure 19   *Reversed strain to fracture versus pre-strain at temperature $T_{rev} = -40$ °C*
              Arrows denote tests stopped due to straightening and tensile dominance over
              bending (jig limit).
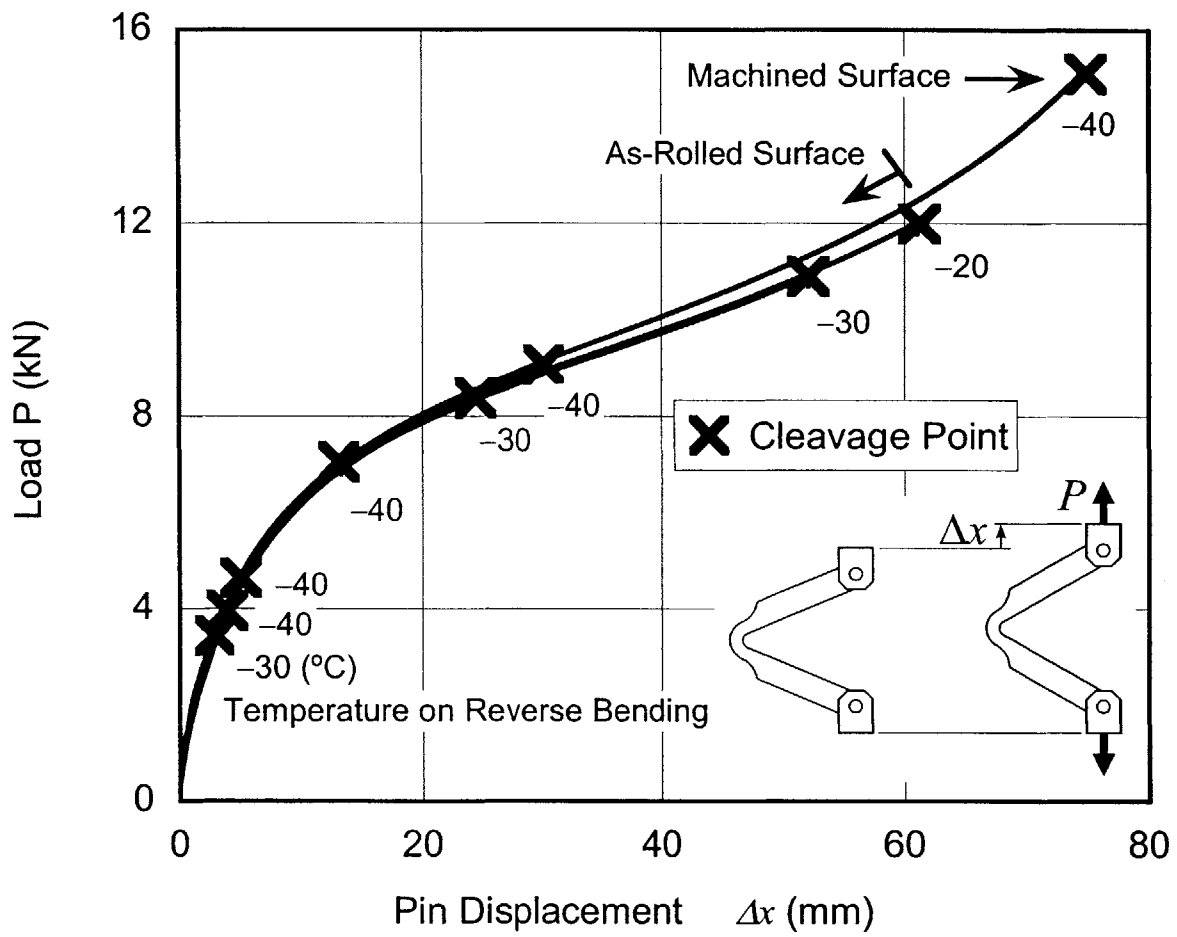
Figure 20   *Load-displacement curves to fracture in reverse bending for $\varepsilon_{pre} = -0.43$*
             (selected)
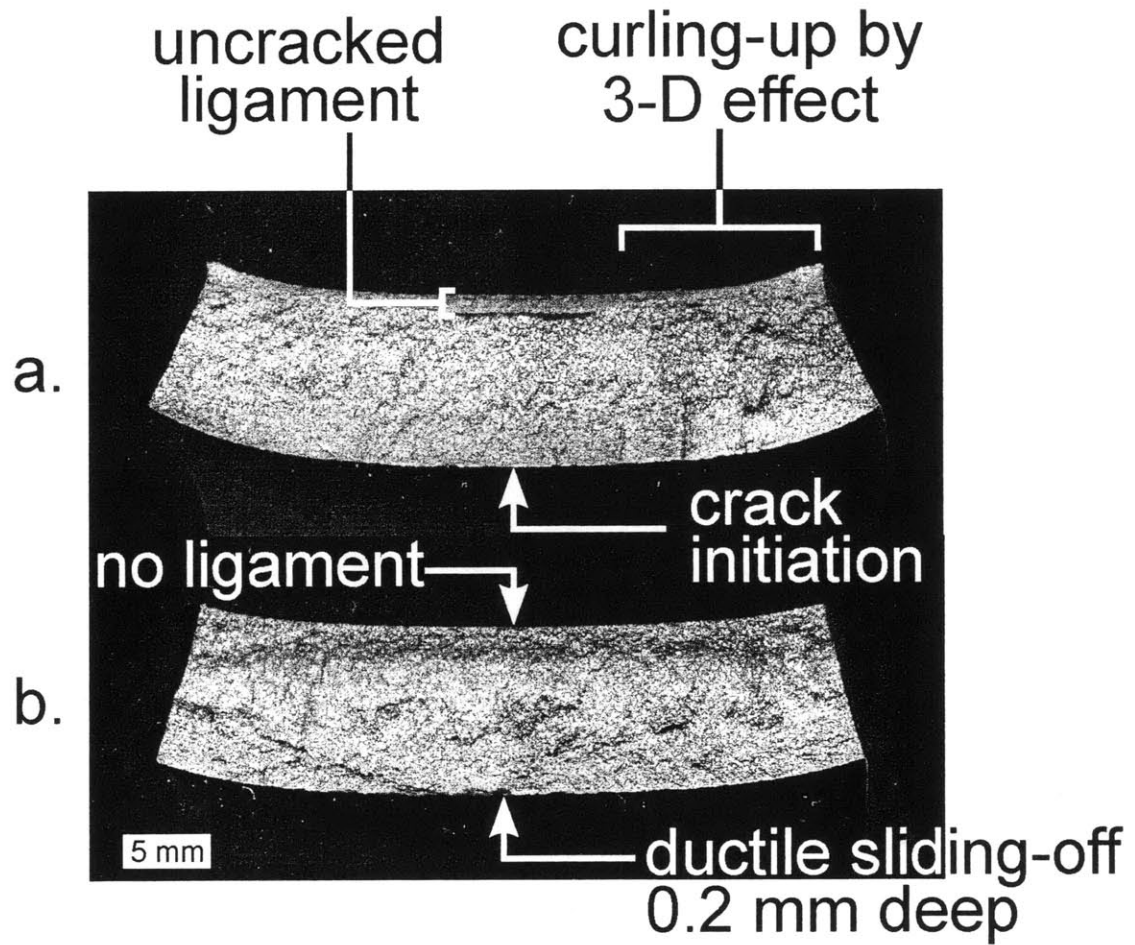
Figure 21   *Cleavage surfaces after pre-strain of $\varepsilon_{pre} = -0.43$, a. $T_{rev} = -40\ °C$ and $\varepsilon_{revf} = 0.019$, b. $T_{rev} = -20\ °C$ and $\varepsilon_{revf} = 0.265$*
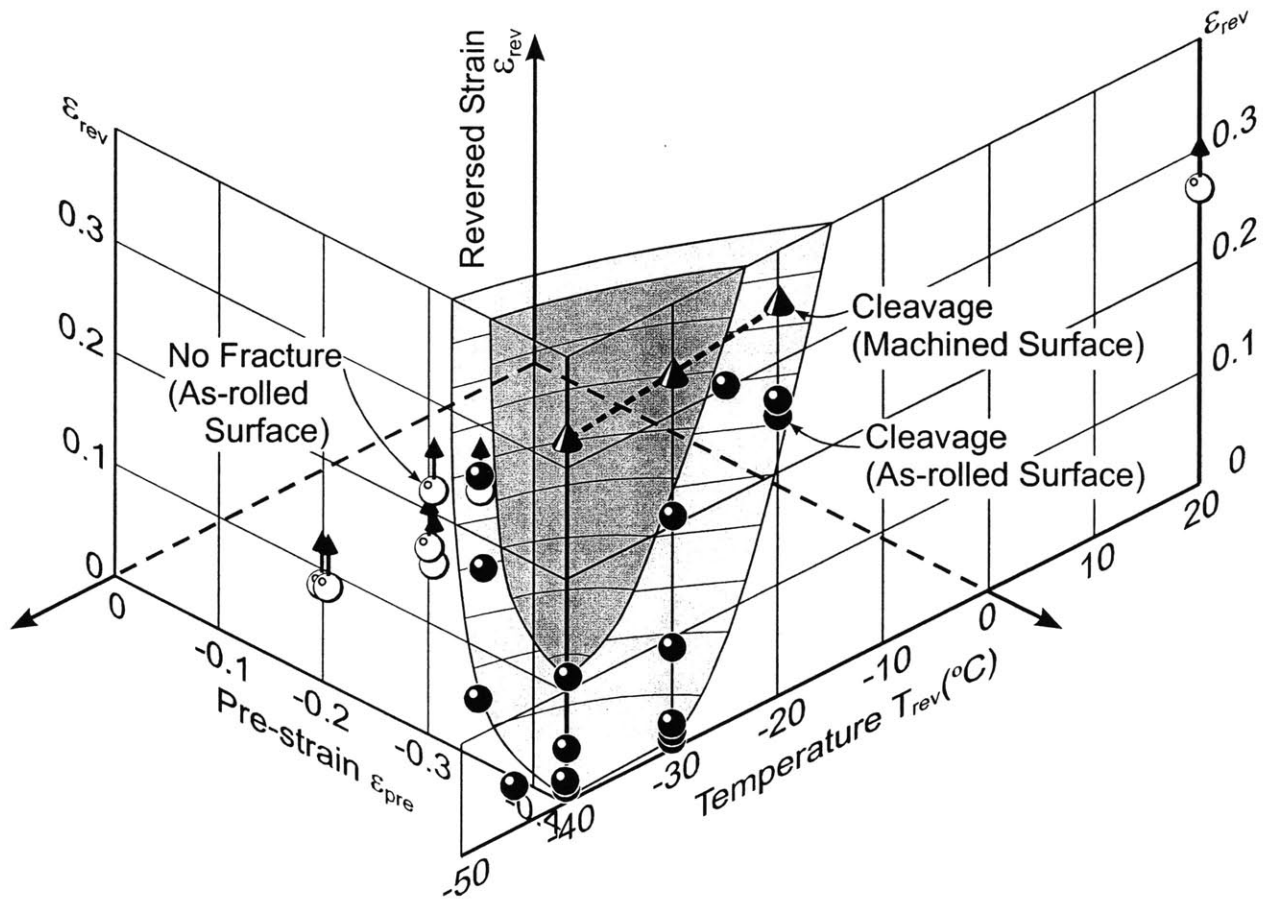
Figure 22   3-D cleavage locus for reverse bending

Temperature of Reverse Bending T_{rev} (°C)

-40   -20   0

AH36, T_{pre} = 20 °C
ε_{revf} = 0.2

Ductile
Fracture

Cleavage
Fracture

-0.2

-0.4

Pre-
Strain
ε_{pre}

(a) ε_{revf} = 0.2 cleavage transition

Temperature of Reverse Bending T_{rev} (°C)

-40   -20   0

AH36, T_{pre} = 20 °C
ε_{revf} = 0.01

Ductile
Fracture

ABS-B Steel
ε_{revf} ~ 0.01
(Dvorak &
Mylonas, 1968)

Cleavage
Fracture

-0.2

-0.4

Pre-
Strain
ε_{pre}

(b) ε_{revf} = 0.01 cleavage transition
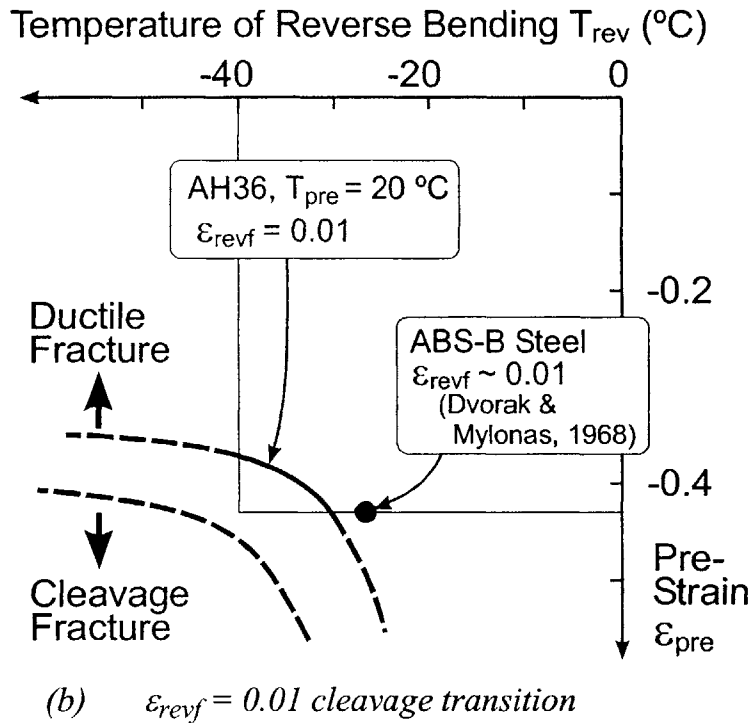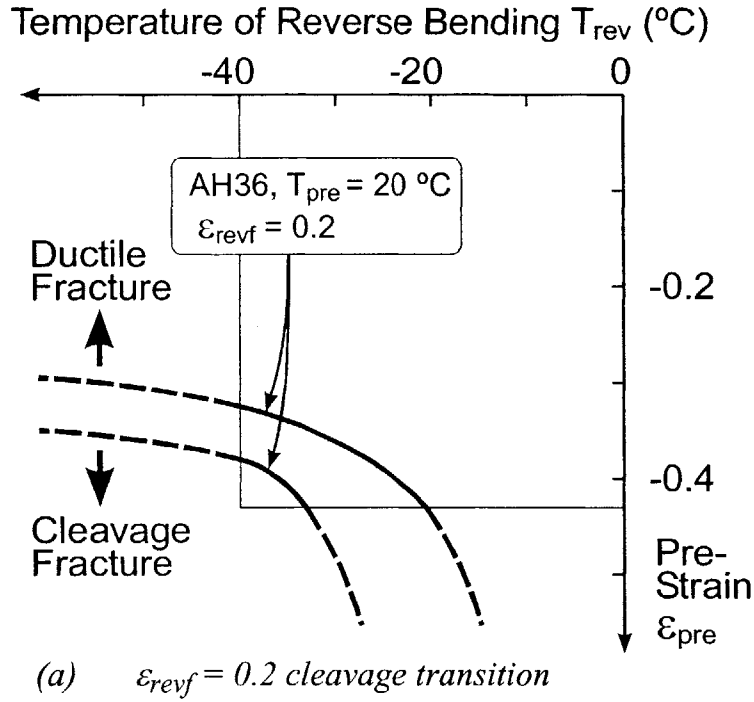
Figure 23   Cleavage transition over ε_{pre}-T_{rev} plane

As-rolled Surface   Machined Surface
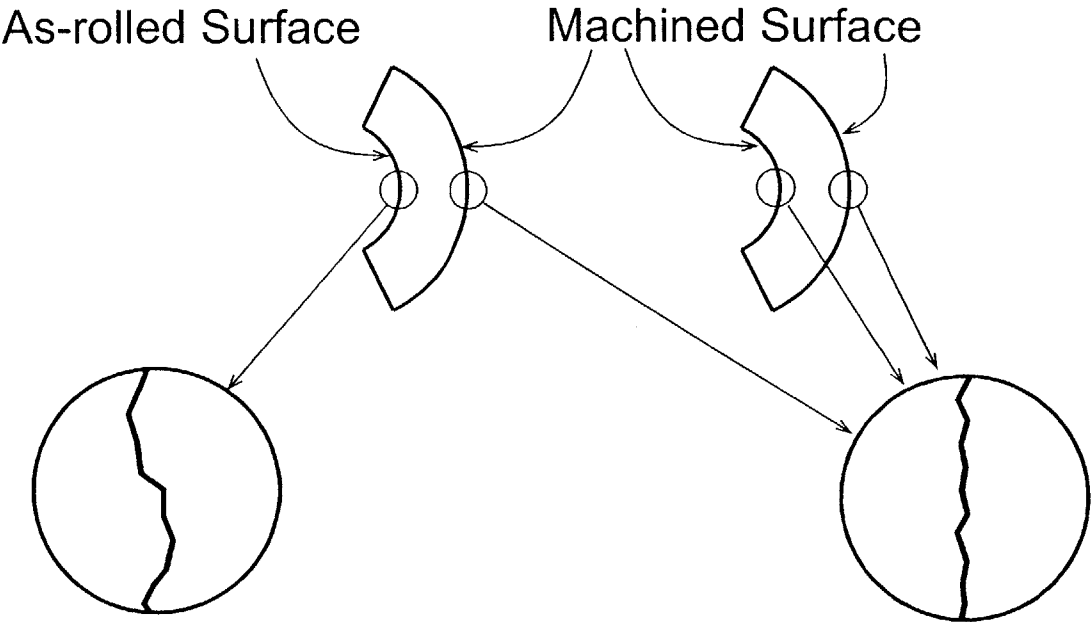
Figure 24   *Undulations accelerated by initial imperfections of as-rolled surface and*
               machined surface
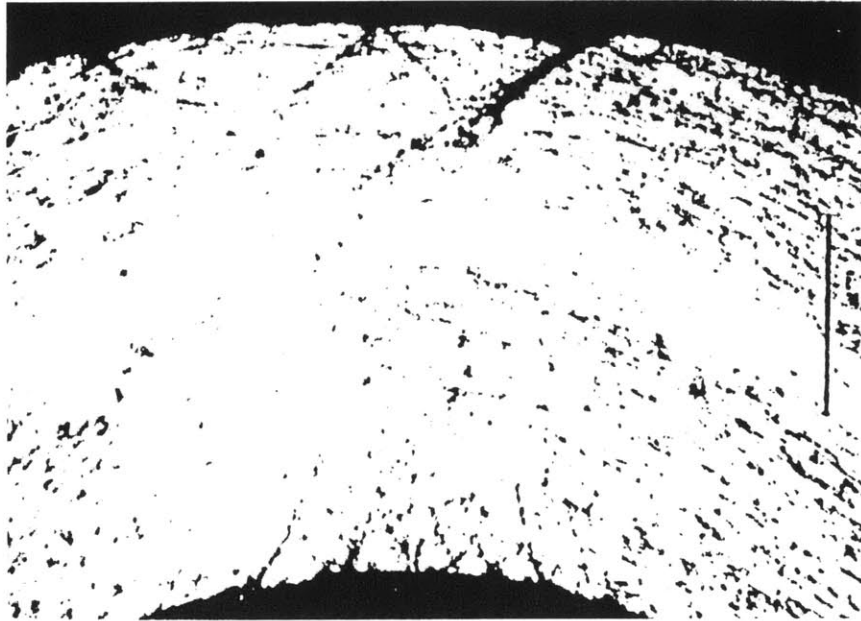
Figure 25   *Shear bands in a micrograph of a sheet deformed in bending (Becker, 1992)*
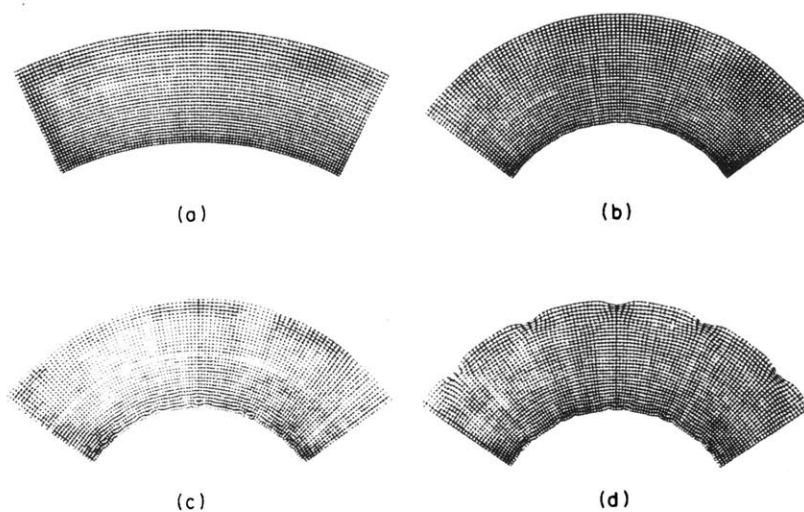
Figure 26   The deformed mesh of plate bending at four curvatures for the nonlinear elastic solid. (a) h/R=0.300, (b) 0.626, (c) 0.632 and (d) 0.654. (Triantafyllidis, Needleman and Tvergaard, 1982)

(The outer boundaries should have been drawn at
constant arc lengths from ABGH.)
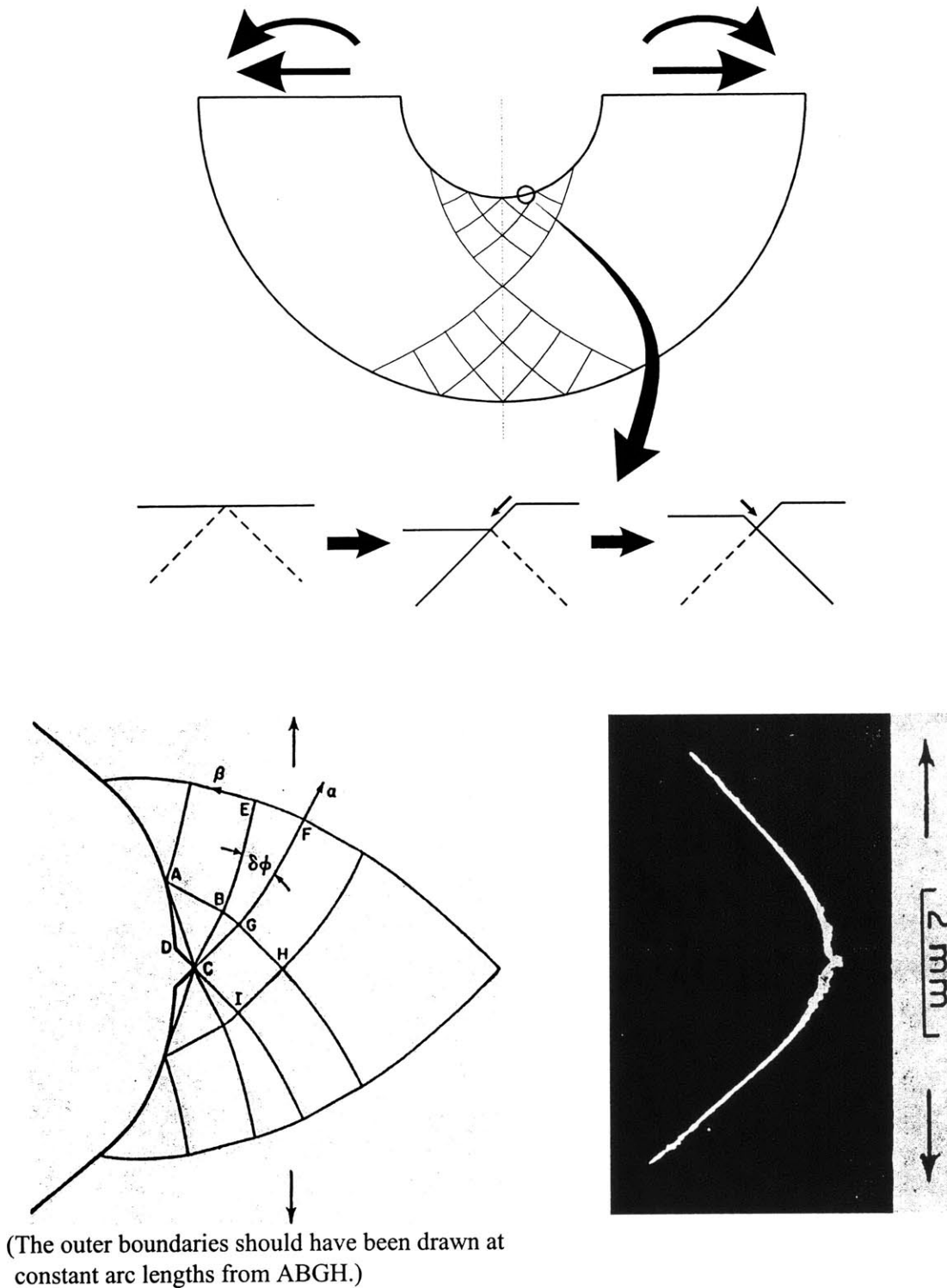
Figure 27   *V-groove formation in a bent plate in opening (top), slip line field for a V-groove at the tip of a rounded groove in tension (bottom left), and optical section showing a 90° V-groove in 1100-F aluminum (bottom right) (McClintock 1971, 1999)*
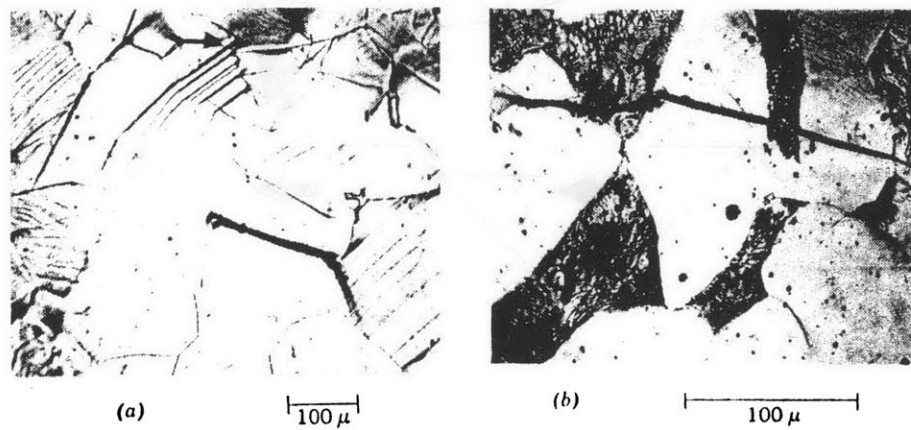
Figure 28   *Microcracks in specimens prior to fracture.   (a) Ferrite F2, coarse grain, −140 °C, strained 8%.   (b) Steel E, coarse grain, −152 °C, strained 3.5% (Hahn et al., 1959)*

Part III   Appendices

Appendix A   Comparison of Bending Strains - Theory, FEM & Measurement

Summary

For the bent plate, the bending strain found from the non-hardening plane strain assumption following Appendix C was compared with results of FEM and measurements. The engineering bending strain by the assumption expressed suitable values for the large pre-bending strain.

1.   Objective

In the reverse bending cleavage tests, pre-strain due to bending is one of the important factors affecting the cleavage condition. Bending strains derived by non-hardening plane strain assumption were compared with FEM results and measurements.

2.   Plane strain bending strain

Since the middle part with thickness reduced is considered to be plane strain condition, the classical plane strain bending plate theory by Hill (1950) and Lubahn and Sachs (1950) was used to define the bending strain. (See also Appendix C) The bending strain is concentrated in the middle part of the specimen, and the other parts remain undeformed (Figure A1). The bent specimen is modeled as three parts, i.e., one uniformly bending part and two rigid parts, which are also shown in Figure A1. The bending part has a thickness h and length s_{eff}. The rigid parts have a length l_{eff}. These effective lengths shown in Figures A1 and A2 are functions of the geometry:

$$s_{eff} = f\left(s_h, h, R_C\right), \quad l_{eff} = g\left(s_h, h, h_p, R_C, l_p\right) \tag{A1}$$

where l_p is the half of the pinhole distance of the undeformed specimen. More precisely, s_{eff} and l_{eff} should also be a function of the bend angle β. However, in the following analyses, the variation of them during bending was assumed negligible, and $s_{eff} = 25.4$ mm and $l_{eff} = 90$ mm were used for $s_h = 19.05$ mm, $h = 9.525$ mm, $h_p = 19.05$ mm, and $l = 101.60$ mm.

Assume that the material is non-hardening (perfectly plastic) in plane strain, and an uncracked continuum. Under this condition, Hill derived that the thickness remains unchanged after bending. For large bending, the unstretched (neutral) plane, which has experienced the same

amount of first compression and then extension during bending, turns out to be at the middle of the plate (See Appendix C). If the bend angle is β and the angle of the bent specimen is θ, from Figure A1,

$$\beta + \theta = \pi \tag{A2}$$

The lengths of the outside and inside elements are respectively

$$s_{eff} + \frac{h\beta}{2}, \quad s_{eff} - \frac{h\beta}{2}, \tag{A3}$$

giving the engineering strains

$$\varepsilon_o, -\varepsilon_i = \frac{h\beta}{2s_{eff}} = \frac{h(\pi - \theta)}{2s_{eff}} \tag{A4}$$

Eliminating h with the radii of the curved plate gives

$$\varepsilon_o, -\varepsilon_i = \frac{h}{2R_u} = \frac{R_0 - R_i}{R_0 + R_i} = \frac{h}{2R_i + h} \quad \text{where} \quad R_u = \frac{R_i + R_o}{2}. \tag{A5}$$

3.   Four kinds of strain estimates

For the bending angles of $\theta = 0$ to $180°$, the following four strains were compared.

(1) Non-hardening plane strain

Using Equation (A4) with $h = 9.525$ mm and $s_{eff} = 25.4$ mm, the engineering strains are obtained in terms of the bending angle. The angle of θ is measured between the two rigid parts. The absolute values of the engineering strains on the outside and the inside of the bent plate are equal.

(2) Measured by curvature

On measurement, it was assumed that the relation of the outer and inner radii satisfies $R_0 = R_i + h$, and only R_i and h were measured. The inner radius R_i was measured by putting drill bits inside the bent plate. Using Equation (A5), the engineering strains are obtained in terms of curvature and plate thickness. The absolute values of the engineering strains on the outside and the inside of the bent plate are equal.

(3) Measured by marking

Multi-square concentric strain gauge marks were drawn on the outside of the bending plate. An example of the deformed gauge mark is shown in Figure A3. The side length of the smallest

square was nominally 2 mm. The size of the mark was measured before and after bending. The strain on the outside surface was calculated using:

$$\varepsilon_o = \frac{l_a - l_b}{l_b}$$ (A6)

where l_b and l_a are the longitudinal lengths of the strain mark before and after the bending. The strain on the inside of bent plate was not measured by this method.

(4) FEM

Using a quarter symmetrical 3D FEM model shown in Figure A4 and A5, the strains on the outside and inside surface of the bent plate were calculated by ABAQUS. The material properties are:

Young's modulus	$E = 206 \times 10^9$ Pa
Poisson ratio	$v = 0.3$
Density	$\rho = 7833$ kg/m^3
Yield strength	$\sigma_Y = 381 \times 10^6$ Pa
Strain hardening	multilinear down to $d\sigma/d\varepsilon = 333.3$ MPa
	(See Figures B3 in Appendix B and E4-12 in Appendix E)
Fracture option	no

In Figure A4, strain histories were monitored on the two points A (inside) and B (outside). For the details of the analysis, see Appendix B.

4.   Comparison

Four strains on the outside, by non-hardening plane strain bending theory, curvature, marking, and FEM, are plotted in Figure A6. Three strains on the inside, by non-hardening plane strain bending theory, curvature, and FEM, are plotted in Figure A7.

In the both figures, the non-hardening plane strain bending theory is representing good strain estimates for the large angle bending of the plate.

References

HILL, R.,   1950   *The Mathematical Theory of Plasticity*, pp 287-294, Clarendon Press, Oxford

LUBAHN, D. AND SACHS, G.   1950   *Trans. ASME*, **72**, 201

115
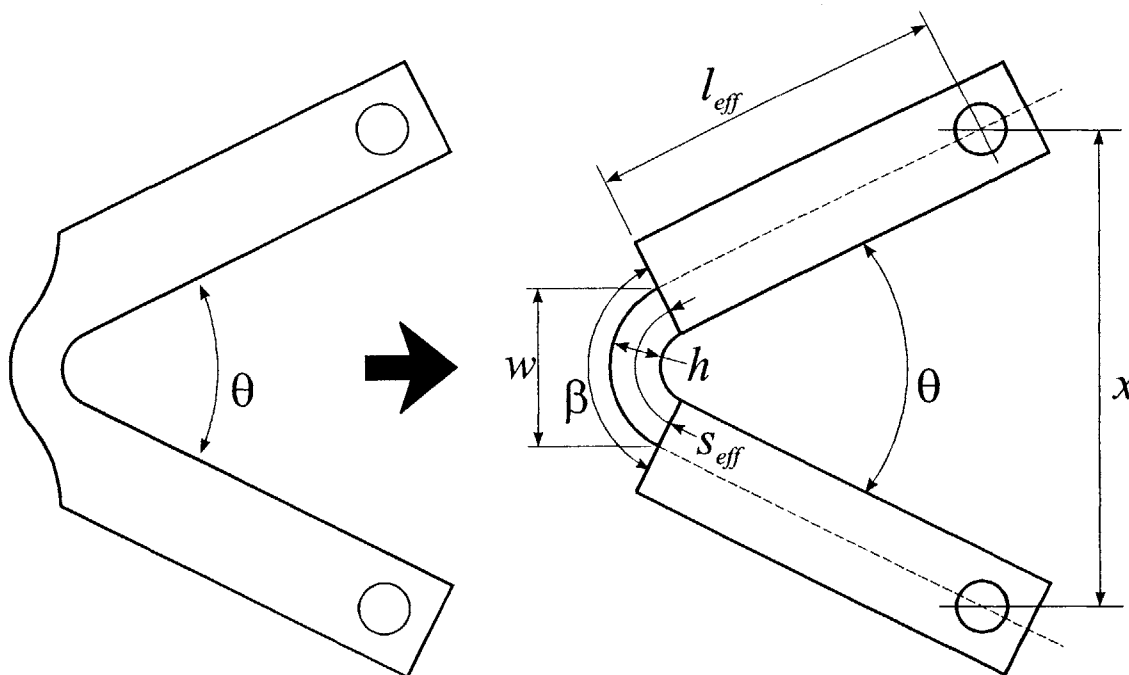
Figure A1   Bending specimen modeling for relation between bend angle and bending strain
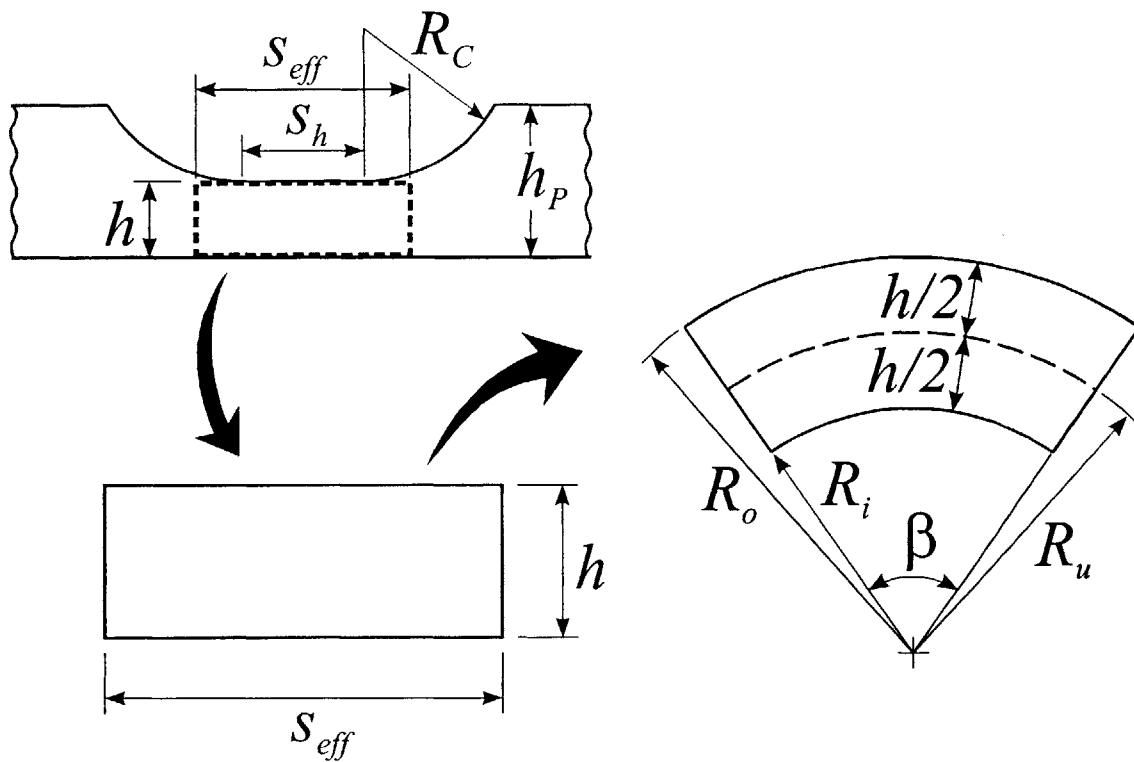
Figure A2   Plane strain bending with effective length s_{eff}
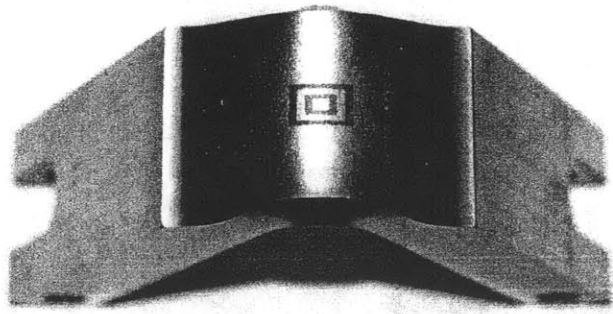
Figure A3   An example of deformed strain gauge mark
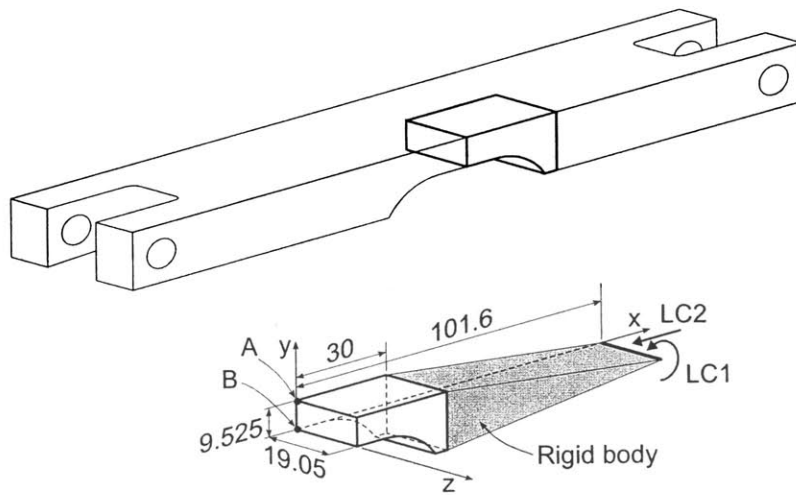
Figure A4   Quarter symmetrical FEM model with observation points A &B

Figure A5   FEM mesh

117
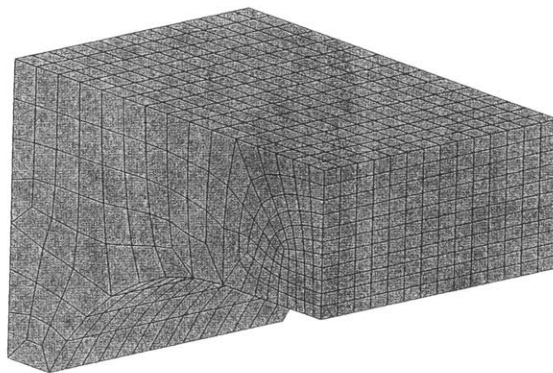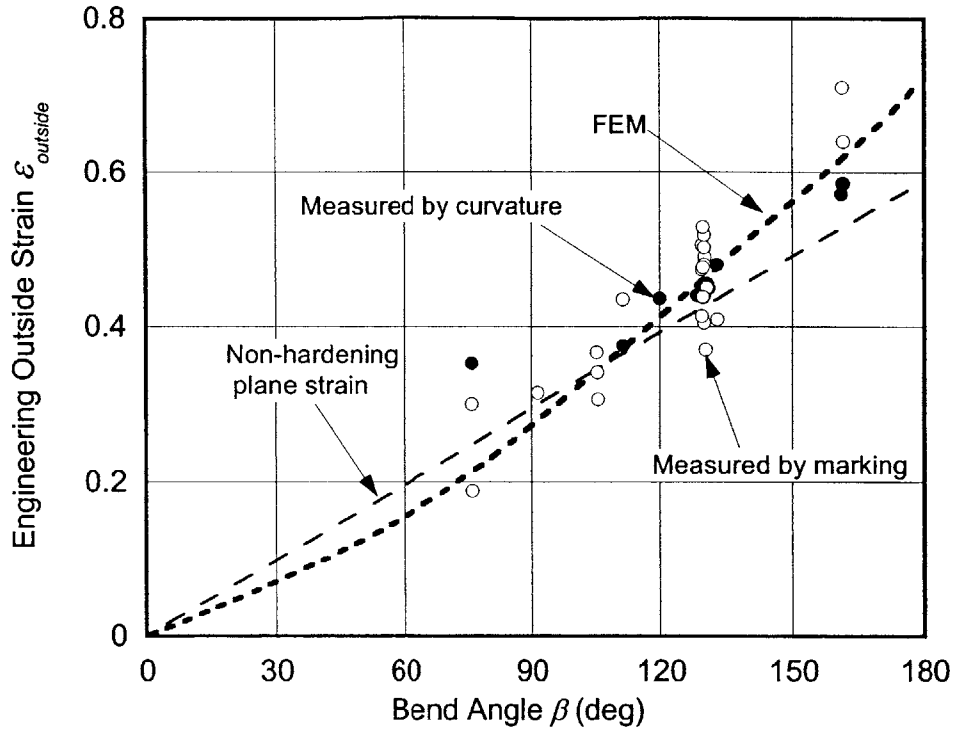
Figure A6   Engineering bending strains on the outside of bent plate
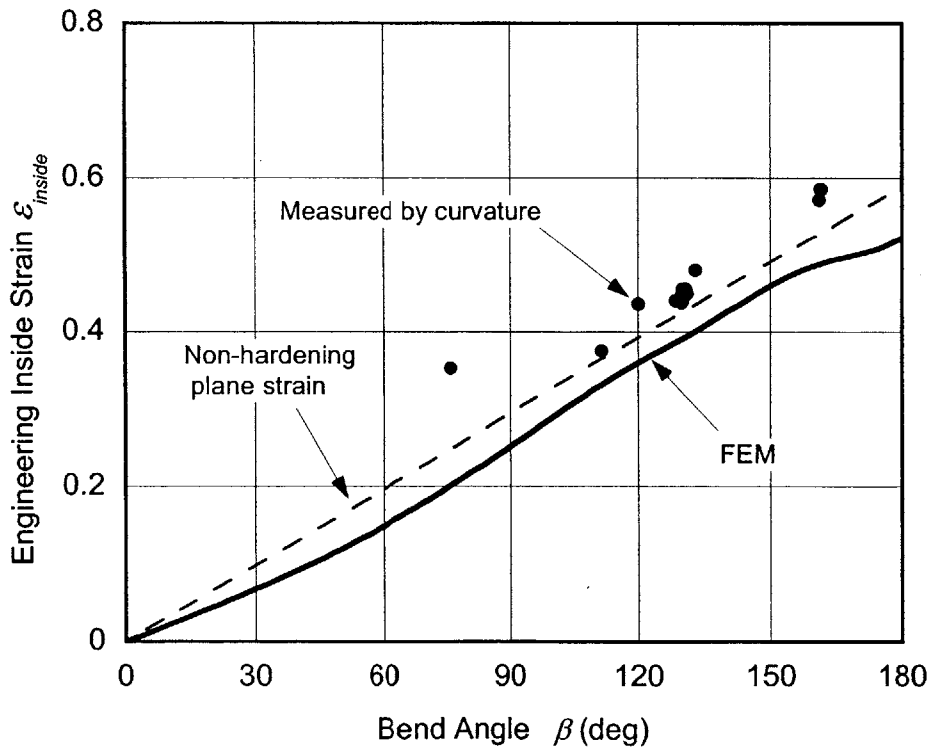
Figure A7   Engineering bending strains on the inside of bent plate

Appendix B   Numerical Bending Analysis - ABAQUS

1.   Introduction

In the study of cleavage of steel plate under reversed bending, the bending strain was esti-mated by the perfect plastic bending plate theory. To validate the pre-strain in reverse bending experiments, an FEM analysis was carried out using ABAQUS. In the bending test, the specimen is bent in two steps: 4-point bending and end-loading bending. The central part of the specimen is thinned so that the bending strain is concentrated there. That part and some of the transition are extracted for calculations, and the other parts are considered rigid (Figure B1). A quarter sym-metrical model is used with isotropic hardening. In the 4-point bending, the central modeled part is subjected to a pure bending. In the end-loading bending, that part is subjected to a linear displacement with free rotation by the rigid parts. The sequence of load conditions followed the actual test sequence.

2.   Model

2.1   FEM Model and Symmetry Conditions

The middle part of the bending specimen was modelled by a quarter symmetry shown in Figure B1. The $x = 0$ and $z = 0$ planes are symmetrical boundaries. The FEM mesh is shown in Figure B2. To apply two kinds of loading, a triangular prismatic rigid body was connected behind the deformable part.

Material Properties:

Young's modulus	$E = 206,000$ MPa
Poisson ratio	$v = 0.3$
Density	$\rho = 7833$ kg/m^3
Yield stress	$\sigma_Y = 381$ MPa
Strain hardening	multilinear down to $d\sigma/d\varepsilon = 333.3$ MPa (See Figure B3)
Fracture option	no

Element type	C3D8R

(8-node linear brick, reduced integration with hourglass control of the ABAQUS element library)

Number of nodes   2430

Number of elements: 1904

Solver   ABAQUS Standard (implicit) Version 5.8-14

Machine   Dell Optiplex GX1 333MHz

Total CPU time: 6837.4 sec

2.2   Load Conditions

The model was bent by prescribed displacements in two steps. Both loads were applied to the far end of the rigid body to simulate the loading conditions. Bend angle θ is measured around z-axis at the loading point, i.e., the total bend angle of the specimen is 2θ.

LC1   Bending $d\theta_z/dt = 0.4019$ rad/sec   1 second
        (yields final angle of $\theta = 23.03°$)

LC2   Translation $dx/dt = -0.065$ m/sec   1 second
        (yields final angle of $\theta = 93.1°$)

3.   Results

3.1   Strain Histories

The strain histories at two points A and B in Figure B1 were obtained as the bend angle θ increased. The point A is on the inside surface of the bent specimen and the point B is on the outside of it. The values are of the integration points of the elements on the points A and B. The true strains $\varepsilon_{inside,true}$ and $\varepsilon_{outside,true}$ versus bend angle $2\theta (= \beta)$ are shown in Figure B4. The true strains obtained from the FEM were converted to engineering strains using

$$\varepsilon = \exp\left(\varepsilon_{true}\right) - 1 \tag{B1}$$

where ε is the engineering strain and ε_{true} is the true strain, both axial. The engineering strains ε_{inside} and $\varepsilon_{outside}$ versus bend angle $2\theta (= \beta)$ are shown in Figure B5.

While the strain on the outside surface is increasing uniformly as the bend angle is increas-

ing, the strain on the inside surface is waving in the latter half. This may be due to a bifurcation caused by high strain concentrated in the region. Further study is needed to explain this waviness.

3.2 Other Results

At the bend angle of $\theta = 65.23°$ ($\beta = 130.46°$), which is the highest pre-bending angle in the reverse bending test, the following field results are shown in figures. In the following, "outside edge" is on the integration point of the element on the edge on the outside of the bent part, and "inside center" is on the integration point of the element on the center of inside surface of the bent part. In the figures, coordinates 1, 2 and 3 are representing x, y and x axes in Figure B1.

Figure B6	Deformed mesh
Figure B7	von Mises equivalent stress
	Highest of 804 MPa at edge on tension side (outside)
Figure B8	Normal stress in x-direction
	Highest of 845 MPa at edge on tension side (outside)
	Lowest of –1078 MPa at center on compression side (inside)
Figure B9	Plastic equivalent strain
	Highest of 0.558 at center on compression side (inside)
Figure B10	Normal logarithmic strain in x-direction
	Highest of 0.473 at edge on tension side (outside)
	Lowest of –0.498 at center on compression side (inside)

As shown in Figure B9, the high strain region is concentrated and its length is approximately the same as the thickness in the center of specimen. The plane strain region is short and approximately 5 mm long in the central part of the bent specimen.

4. Extracted Input Code

The extracted code from ABAQUS an input file is appended in the end of this Appendix.
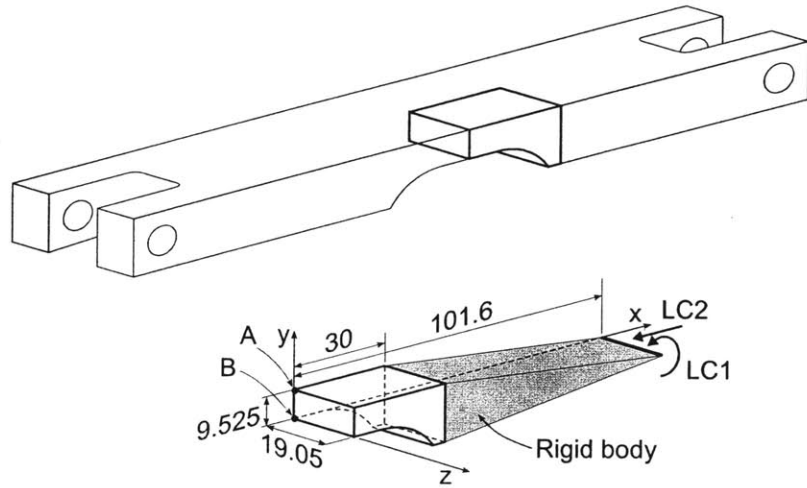
Figure B1   Quarter symmetrical FEM model with observation points A & B
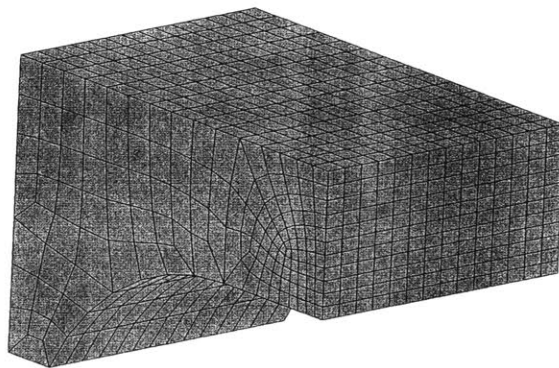
Figure B2   FEM mesh
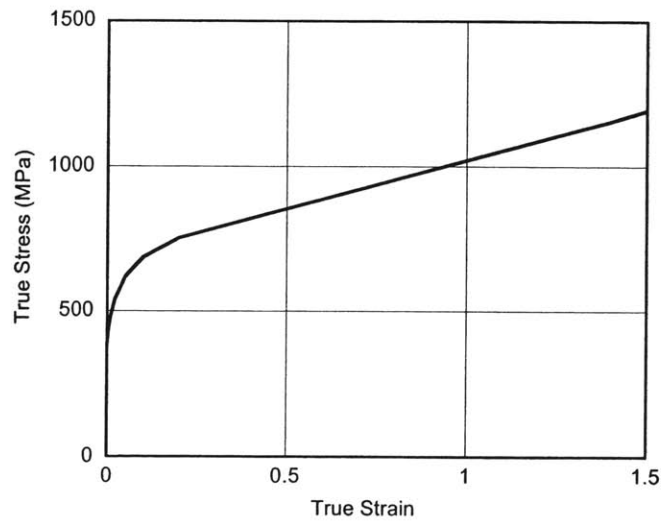
Figure B3   True stress - true strain curve
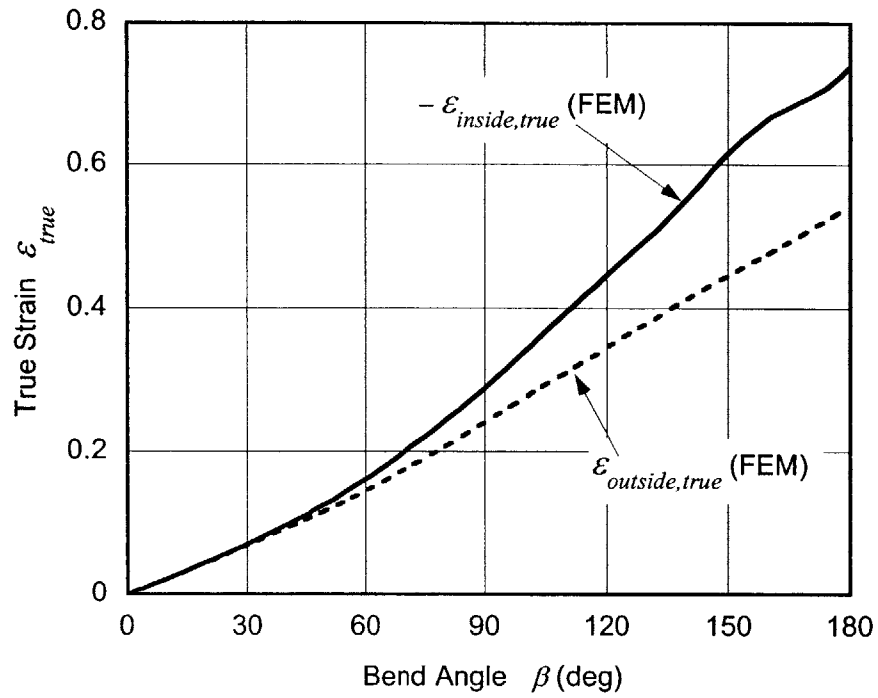
Figure B4   True strains versus bend angle 2θ (= β)
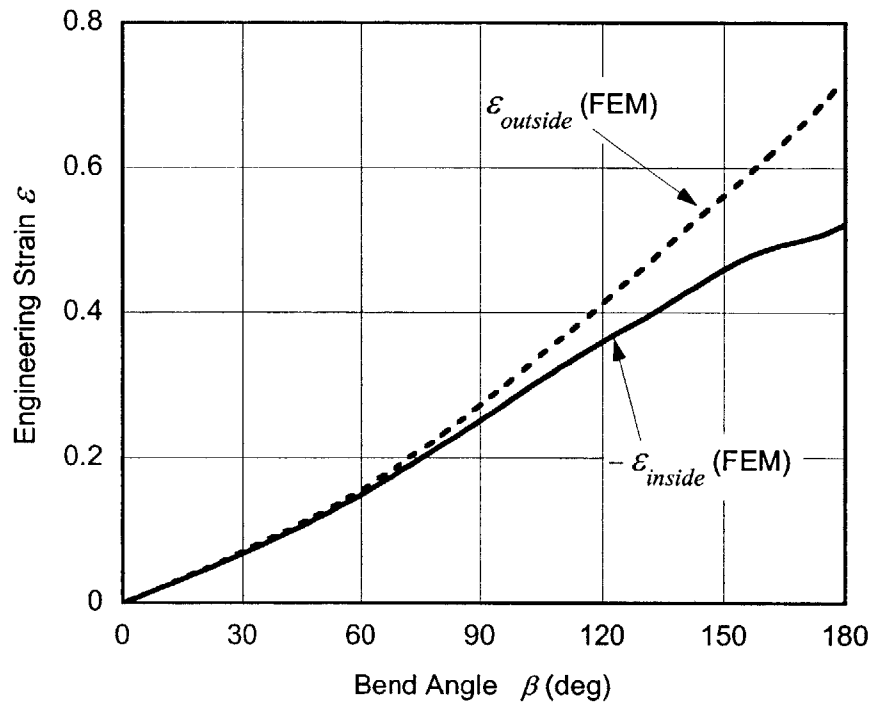
Figure B5   Engineering strains versus bend angle 2θ (= β)

Printed on: Sat Mar 18 12:24:19 est 2000

ABAQUS

Viewport: 1 Model: Model-1 Module: Visualization

```
          reverse bending - isotropic
          ODB: reverse.odb    ABAQUS/Standard 5.8-14    Fri Mar 17 20:00:07 est
  2
  |
1 |   3  Step: Bend-2: Apply 2nd Bend    Increment      34: Step Time =    0.4992

          Deformed Var: U    Deformation Scale Factor: +1.000e+00
```
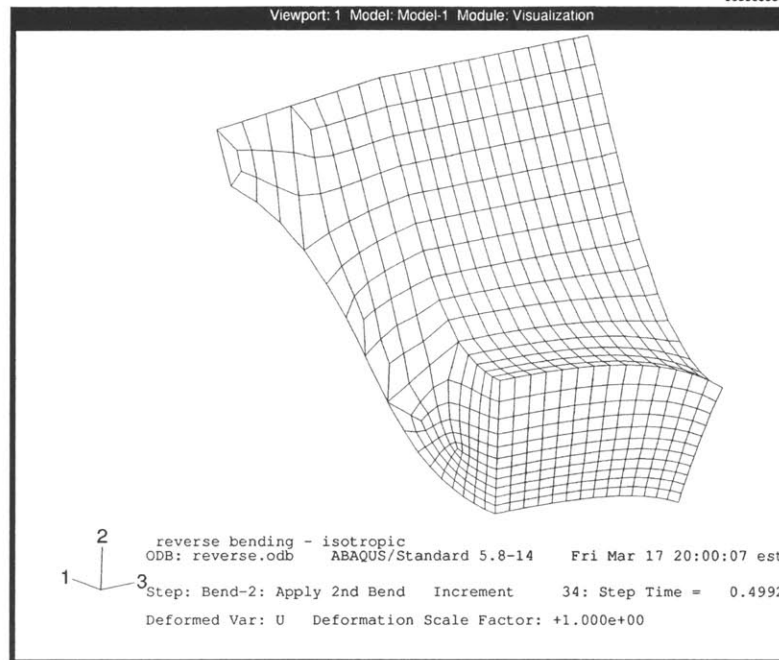
Figure B6   *Deformed mesh at $\beta = 2\theta = 130.46°$*

Printed on: Sat Mar 18 12:21:49 est 2000
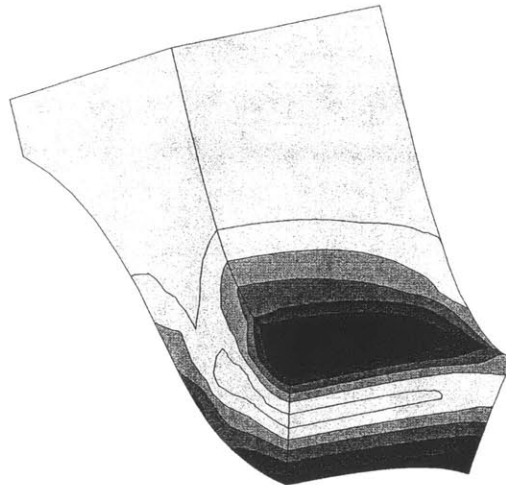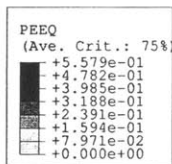
ABAQUS

Viewport: 1 Model: Model-1 Module: Visualization

```
S, Mises
(Ave. Crit.: 75%)
  +8.040e+08
  +6.961e+08
  +5.881e+08
  +4.802e+08
  +3.722e+08
  +2.643e+08
  +1.563e+08
  +4.836e+07
```

```
          reverse bending - isotropic
          ODB: reverse.odb    ABAQUS/Standard 5.8-14    Fri Mar 17 20:00:07 est
  2
  |
1 |   3  Step: Bend-2: Apply 2nd Bend    Increment      34: Step Time =    0.4992
          Primary Var: S, Mises
          Deformed Var: U    Deformation Scale Factor: +1.000e+00
```

Figure B7   *von Mises equivalent stress at $\beta = 2\theta = 130.46°$*

Figure B8   Normal stress in x-direction (S11)   at β = 2θ = 130.46°

Figure B9   Plastic equivalent strain (PEEQ)   at β = 2θ = 130.46°

Viewport: 1 Model: Model-1 Module: Visualization

LE, LE11
(Ave. Crit.: 75%)
    +4.725e-01
    +3.339e-01
    +1.953e-01
    +5.666e-02
    -8.195e-02
    -2.206e-01
    -3.592e-01
    -4.978e-01

reverse bending - isotropic
ODB: reverse.odb   ABAQUS/Standard 5.8-14   Fri Mar 17 20:00:07 est
Step: Bend-2: Apply 2nd Bend   Increment   34: Step Time =   0.4992
Primary Var: LE, LE11
Deformed Var: U   Deformation Scale Factor: +1.000e+00

Figure B10   Normal logarithmic strain in x-direction (LE11) at $\beta = 2\theta = 130.46°$

ABAQUS Standard - Extracted input code

```
*Heading
 reverse bending - isotropic
** Job name: reverse Model name: Model-1
** ─────────────────────────────────────────────
**
** PART INSTANCE: specimen-1
**
*Node
       1,     0.0131298,      0.009525,        0.01905
       2,     0.0124483,   -0.000225631,      0.01905
       3,     0.0202011,    -0.00327268,      0.01905
       4,          0.03,   -0.000881565,      0.01905
       5,          0.03,      0.009525,        0.01905
       6,    0.00859666,      0.009525,        0.01905
       7,      0.009525,    3.46945e-18,       0.01905
       8,     0.0260228,     -0.009525,        0.01905
       9,          0.03,     -0.009525,        0.01905
      10,   3.35276e-10,      0.009525,        0.01905
      11,   3.35276e-10,    3.93837e-18,       0.01905
------------------------------------------------------------------------------------
    2423,    0.00622298,    0.00328513,          0.
    2424,    0.00543274,    0.00295102,          0.
    2425,    0.00467797,    0.00268108,          0.
    2426,     0.0077741,    0.00552579,          0.
    2427,    0.00809923,    0.00365237,          0.
    2428,    0.00711735,    0.00132877,          0.
    2429,    0.00609784,     0.0010879,          0.
    2430,    0.00510446,   0.000959522,          0.
*Element, type=C3D8R
     1,   167,   184,   222,   183,     5,    22,    60,    21
     2,   183,   222,   223,   182,    21,    60,    61,    20
     3,   182,   223,   224,   181,    20,    61,    62,    19
     4,   181,   224,   220,   166,    19,    62,    58,     4
     5,   184,   185,   233,   222,    22,    23,    71,    60
     6,   185,   186,   234,   233,    23,    24,    72,    71
     7,   186,   187,   235,   234,    24,    25,    73,    72
     8,   187,   188,   236,   235,    25,    26,    74,    73
     9,   188,   189,   237,   236,    26,    27,    75,    74
    10,   189,   190,   225,   237,    27,    28,    63,    75
------------------------------------------------------------------------------------
1897, 2364, 2378, 2428, 2383, 2202, 2216, 2266, 2221
1898, 2378, 2379, 2429, 2428, 2216, 2217, 2267, 2266
1899, 2379, 2380, 2430, 2429, 2217, 2218, 2268, 2267
1900, 2380, 2365, 2369, 2430, 2218, 2203, 2207, 2268
1901, 2383, 2428, 2325, 2275, 2221, 2266, 2163, 2113
1902, 2428, 2429, 2324, 2325, 2266, 2267, 2162, 2163
1903, 2429, 2430, 2323, 2324, 2267, 2268, 2161, 2162
1904, 2430, 2369, 2322, 2323, 2268, 2207, 2160, 2161
*Nset, nset=specimen-1._G4, generate
     1,   2430,       1
*Elset, elset=specimen-1._G4, generate
     1,   1904,       1
**
** SECTIONS
**
** Section: SolidSection
*Solid Section, elset=specimen-1._G4, material=Steel
1.,
** ─────────────────────────────────────────────
**
** PART INSTANCE: Rigid_body-1
```

```
**
*System
      0.03,            0.,    0.009525,          1.03,           0.,     0.009525
*Node
   2431,         0.0716,            0.,       -0.009525
*Nset, nset=Rigid_body-1-RefPt_
 2431,
*System
*Nset, nset=_G11
    10,    11,    40,    41,    42,    43,    44,    45,    46,    47,    48,    49,   172,   173,   202,   203
   204,   205,   206,   207,   208,   209,   210,   211,   334,   335,   364,   365,   366,   367,   368,   369
   370,   371,   372,   373,   496,   497,   526,   527,   528,   529,   530,   531,   532,   533,   534,   535
------------------------------------------------------------------------------------------
 2148, 2149, 2150, 2151, 2152, 2153, 2154, 2155, 2278, 2279, 2308, 2309, 2310, 2311, 2312, 2313
 2314, 2315, 2316, 2317
*Elset, elset=_G11
    56,    57,    58,    59,    60,    81,    82,    83,    84,    85,    86,   192,   193,   194,   195,   196
   217,   218,   219,   220,   221,   222,   328,   329,   330,   331,   332,   353,   354,   355,   356,   357
------------------------------------------------------------------------------------------
 1579, 1580, 1581, 1582, 1688, 1689, 1690, 1691, 1692, 1713, 1714, 1715, 1716, 1717, 1718, 1824
 1825, 1826, 1827, 1828, 1849, 1850, 1851, 1852, 1853, 1854
*Nset, nset=_G12, generate
 2269,  2430,     1
*Elset, elset=_G12, generate
 1769,  1904,     1
*Nset, nset=_G13
 2431,
*Nset, nset=_G14
 2431,
*Nset, nset=_G15
 2431,
*Nset, nset=_G68, generate
 2269,  2430,     1
*Elset, elset=_G68, generate
 1769,  1904,     1
*Nset, nset=_G69
 2431,
*Nset, nset=_G70, generate
 2269,  2271,     1
 2274,  2276,     1
 2278,  2286,     1
 2290,  2301,     1
 2304,  2430,     1
*Elset, elset=_G70, generate
 1769,  1904,     1
*Nset, nset=_G79
 2431,
*Nset, nset=_G85
 2431,
*Nset, nset=_G86
 2431,
*Nset, nset=All_Surface
     1,     2,     3,     4,     5,     6,     7,     8,     9,    10,    11,    12,    13,    14,    15,    16
    17,    18,    19,    20,    21,    22,    23,    24,    25,    26,    27,    28,    29,    30,    31,    32
------------------------------------------------------------------------------------------
 2401, 2402, 2403, 2404, 2405, 2406, 2407, 2408, 2409, 2410, 2411, 2412, 2413, 2414, 2415, 2416
 2417, 2418, 2419, 2420, 2421, 2422, 2423, 2424, 2425, 2426, 2427, 2428, 2429, 2430
*Elset, elset=All_Surface
     1,     2,     3,     4,     5,     6,     7,     8,     9,    10,    11,    12,    13,    14,    15,    16
    17,    18,    19,    20,    21,    22,    23,    24,    25,    26,    27,    28,    29,    30,    31,    32
------------------------------------------------------------------------------------------
 1881, 1882, 1883, 1884, 1885, 1886, 1887, 1888, 1889, 1890, 1891, 1892, 1893, 1894, 1895, 1896
 1897, 1898, 1899, 1900, 1901, 1902, 1903, 1904
*Nset, nset=DataPlane
    10,    11,    40,    41,    42,    43,    44,    45,    46,    47,    48,    49,   172,   173,   202,   203
   204,   205,   206,   207,   208,   209,   210,   211,   334,   335,   364,   365,   366,   367,   368,   369
------------------------------------------------------------------------------------------
```

```
 2148, 2149, 2150, 2151, 2152, 2153, 2154, 2155, 2278, 2279, 2308, 2309, 2310, 2311, 2312, 2313
 2314, 2315, 2316, 2317
*Elset, elset=DataPlane
    60,    81, 1828, 1849
*Nset, nset=DataPoint
    10,    11, 2278, 2279
*Nset, nset=Monitor
 2431,
*Amplitude, name=My_Ramp, smooth=0.25
0., 0., 0.1, 0., 0.5, 1.25, 1.1, 1.25
**
** MATERIALS
**
*Material, name=Steel
*Density
7833.,
*Elastic
 2.06e+11, 0.3
*Plastic
 3.810E+08,   0.
 3.850E+08,   0.0002
 3.900E+08,   0.0005
 3.990E+08,   0.001
 4.120E+08,   0.002
 4.400E+08,   0.005
 4.670E+08,   0.01
 5.110E+08,   0.02
 5.770E+08,   0.05
 6.160E+08,   0.1
 6.580E+08,   0.2
 7.800E+08,   0.5
 1.153E+09,   1.4
 4.717E+09,   10.
*Surface Interaction, name=_Tied
**
** PHYSICAL CONSTANTS
**
*Physical Constants, absolute zero=0., stefan boltzmann=0.
**
** BOUNDARY CONDITIONS
**
** BC: Rail Type: Displacement
*Boundary
_G69, 1, 1
_G69, 2, 2
_G69, 3, 3
_G69, 4, 4
_G69, 5, 5
_G69, 6, 6
** BC: Symmetry-X Type: Typed
*Boundary
_G11, XSYMM
** BC: Symmetry-Z Type: Typed
*Boundary
_G70, ZSYMM
*Elset, elset=_Specimen_S6
      1,     2,     3,     4,    46,    47,    48,   137,   138,   139,   140,   182,   183,   184,   273,   274
    275,   276,   318,   319,   320,   409,   410,   411,   412,   454,   455,   456,   545,   546,   547,   548
    590,   591,   592,   681,   682,   683,   684,   726,   727,   728,   817,   818,   819,   820,   862,   863
    864,   953,   954,   955,   956,   998,   999,  1000,  1089,  1090,  1091,  1092,  1134,  1135,  1136,  1225
   1226,  1227,  1228,  1270,  1271,  1272,  1361,  1362,  1363,  1364,  1406,  1407,  1408,  1497,  1498,  1499
   1500,  1542,  1543,  1544,  1633,  1634,  1635,  1636,  1678,  1679,  1680,  1769,  1770,  1771,  1772,  1814
   1815,  1816
*Surface Definition, name=Specimen
_Specimen_S6, S6
*Rigid Surface, type=CYLINDER, name=Rigid, ref node=Rigid_body-1-RefPt_
0.03, 0., 0.009525, 100.03, 0., 0.009525
```

```
0.03, 0., -99.9905
START,            0.,      -0.009525
 LINE,            0.,       0.009525
 LINE,        0.0716,             0.
 LINE,            0.,      -0.009525
** Interaction: Tied
*Contact Pair, tied, adjust=0.0001, interaction=_Tied
Specimen, Rigid
** ─────────────────────────────
**
** STEP: Combine
**
*Step
Combine: Establish Combine
*Static
0.1, 1., 1e-06, 1.
**
** OUTPUT REQUESTS
**
*Restart, write, frequency=1
*Monitor, dof=6, node=Monitor, frequency=1
*Output, field, op=NEW, frequency=99999
*Node Output
U, RF, CF
*Element Output
S, E, PE, PEEQ, PEMAG, LE
*Contact Output
CSTRESS, CDISP
*Output, history, op=NEW, frequency=1
*Node Output, nset=Monitor
UR3,
*El Print, freq=999999
*Node Print, freq=999999
*End Step
** ─────────────────────────────
**
** STEP: Bend-1
**
*Step, nlgeom, inc=200
Bend-1: Apply 1st Bend
*Static
0.1, 1., 1e-06, 1.
**
** BOUNDARY CONDITIONS
**
** BC: Rail Type: Displacement
*Boundary, op=NEW
_G69, 2, 2
_G69, 3, 3
_G69, 4, 4
_G69, 5, 5
** BC: Rotation Type: Velocity
*Boundary, op=NEW, type=VELOCITY
_G15, 6, 6, 0.4019
** BC: Symmetry-X Type: Typed
*Boundary, op=NEW
_G11, XSYMM
** BC: Symmetry-Z Type: Typed
*Boundary, op=NEW
_G70, ZSYMM
**
** OUTPUT REQUESTS
**
*Restart, write, frequency=1
*Output, field, op=NEW, frequency=1
*Node Output, nset=All_Surface
U, RF, CF
```

```
*Element Output, elset=All_Surface
S, E, PE, PEEQ, PEMAG, LE
*Output, history, op=NEW, frequency=1
*Element Output, elset=DataPlane
S11, S22, S33, S12, S13, S23, SP, MISES, PRESS, PE11, PE22, PE33, PE12, PE13, PE23, PEP
PEEQ, PEMAG, LE11, LE22, LE33, LE12, LE13, LE23, LEP
*Node Output, nset=DataPoint
U2, U3
*Node Output, nset=Monitor
U1, UR3
*El Print, freq=999999
*Node Print, freq=999999
*End Step
** ─────────────────────────────
**
** STEP: Bend-2
**
*Step, inc=200
Bend-2: Apply 2nd Bend
*Static
0.1, 1., 1e-06, 1.
**
** BOUNDARY CONDITIONS
**
** BC: Compression Type: Velocity
*Boundary, op=NEW, type=VELOCITY
_G85, 1, 1, -0.087
** BC: Rail Type: Displacement
*Boundary, op=NEW
_G69, 2, 2
_G69, 3, 3
_G69, 4, 4
_G69, 5, 5
** BC: Rotation Type: Velocity
*Boundary, op=NEW
** BC: Symmetry-X Type: Typed
*Boundary, op=NEW
_G11, XSYMM
** BC: Symmetry-Z Type: Typed
*Boundary, op=NEW
_G70, ZSYMM
**
** OUTPUT REQUESTS
**
*Restart, write, frequency=1
*Output, field, op=NEW, frequency=1
*Node Output, nset=All_Surface
U, RF, CF
*Element Output, elset=All_Surface
S, E, PE, PEEQ, PEMAG, LE
*Output, history, op=NEW, frequency=1
*Element Output, elset=DataPlane
S11, S22, S33, S12, S13, S23, SP, MISES, PRESS, PE11, PE22, PE33, PE12, PE13, PE23, PEP
PEEQ, PEMAG, LE11, LE22, LE33, LE12, LE13, LE23, LEP
*Node Output, nset=DataPoint
U2, U3
*Node Output, nset=Monitor
U1, UR3
*El Print, freq=999999
*Node Print, freq=999999
*End Step
** ─────────────────────────────
**
** STEP: Extention
**
*Step, inc=200
Extention: Extension
```

```
*Static
0.1, 1., 1e-06, 1.
**
** BOUNDARY CONDITIONS
**
** BC: Compression Type: Velocity
*Boundary, op=NEW
** BC: Pull Type: Velocity
*Boundary, op=NEW, type=VELOCITY
_G86, 1, 1, 0.087
** BC: Rail Type: Displacement
*Boundary, op=NEW
_G69, 2, 2
_G69, 3, 3
_G69, 4, 4
_G69, 5, 5
** BC: Symmetry-X Type: Typed
*Boundary, op=NEW
_G11, XSYMM
** BC: Symmetry-Z Type: Typed
*Boundary, op=NEW
_G70, ZSYMM
**
** OUTPUT REQUESTS
**
*Restart, write, frequency=1
*Output, field, op=NEW, frequency=1
*Node Output, nset=All_Surface
U, RF, CF
*Element Output, elset=All_Surface
S, E, PE, PEEQ, PEMAG, LE
*Output, history, op=NEW, frequency=1
*Element Output, elset=DataPlane
S11, S22, S33, S12, S13, S23, SP, MISES, PRESS, PE11, PE22, PE33, PE12, PE13, PE23, PEP
PEEQ, PEMAG, LE11, LE22, LE33, LE12, LE13, LE23, LEP
*Node Output, nset=DataPoint
U2, U3
*Node Output, nset=Monitor
U1, UR3
*El Print, freq=999999
*Node Print, freq=999999
*End Step
```

Appendix C Bending Strain of Wide Plates

1.   Introduction

In bending and reverse bending using a specimen whose thickness was reduced in the middle part, the strain history was calculated using plate bending theory. For the rough surface such as "as-rolled surface," electrical strain gauges are no longer stuck on the surface. Further, there is no strain gauge to measure the high strain of more than 0.2.

Since the middle part with thickness reduced is considered to be plane strain, the classical plane strain bending plate theory by Hill (1950) and Lubahn and Sachs (1950) was used to calculate the bending strain. Equations and variable expressions in Sections 2 and 3 were taken from Chakrabarty (1987, pp 741-744). In Section 4, the relation between bending angle and bending strain was derived. In Section 5, the relation between bending angle and end displacement was derived, and the reverse strain was obtained in terms of the end displacement.

2.   Bending Stress

Consider the pure bending of a metal plate which is so wide that the strain in the width direction is negligible. The material is assumed to be nonhardening (perfectly plastic) in plane strain, and an uncracked continuum. In the region well away from the loaded ends, the distributions of stress and strain must be identical for all transverse sections of the plate. The original plane surfaces of the plate are assumed to be cylindrical due to bending, the radii of curvature of the internal and external surfaces at any stage being a and b respectively (Figure C1). The principal stresses in the plane of bending act in the radial and circumferential directions, and the equation of equilibrium is

$$\frac{\partial \sigma_r}{\partial r} = \frac{\sigma_\theta - \sigma_r}{r} \tag{C1}$$

where (r, θ) are the polar coordinates with respect to the instantaneous center of curvature. If c denotes the radius of the instantaneous neutral surface, the yield criterion becomes

$$\sigma_r - \sigma_\theta = 2k \qquad a \le r \le c$$
$$\sigma_\theta - \sigma_r = 2k \qquad c \le r \le b \tag{C2}$$

All elements inside the neutral surface are momentarily compressed, and those outside the

neutral surface are momentarily extended. Substituting in (C1) from above, and using the boundary conditions $\sigma_r = 0$ on $r = a$ and $r = b$, gives

$$\sigma_r = -2k\ln\frac{r}{a} \quad \sigma_\theta = -2k\left(1+\ln\frac{r}{a}\right) \quad a \leq r \leq c$$

$$\sigma_r = -2k\ln\frac{b}{r} \quad \sigma_\theta = 2k\left(1-\ln\frac{b}{r}\right) \quad c \leq r \leq b \tag{C3}$$

The magnitude of the hoop stress steadily increases toward $r = c$ in the region of compression, and decreases toward $r = c$ in the region of tension. The condition of continuity of the radial stress across the neutral surface gives

$$\frac{c}{a} = \frac{b}{c} \quad \text{or} \quad c = \sqrt{ab} \tag{C4}$$

The radial stress has its greatest numerical value $k\ln(b/a)$ on the neutral surface, where the jump in the circumferential stress is of the amount $4k$. It follows from (C1) that

$$\int_a^b \sigma_\theta dr = \int_a^b \frac{\partial}{\partial r}(r\sigma_r)\,dr = [r\sigma_r]_a^b = 0 \tag{C5}$$

The condition of zero resultant force across any section is therefore automatically satisfied. The applied couple per unit width is

$$M = \int_a^b \sigma_\theta r\,dr = \frac{1}{2}k\left(a^2+b^2-2c^2\right) = \frac{1}{2}k(b-a)^2 \tag{C6}$$

3.   Bending Strain

The associated velocity field should correspond to a circumferential extension of elements outside the neutral surface, and contraction of elements inside the neutral surface. Since the material is incompressible and isotropic with no shear strains, the components of the strain rate must satisfy the relations $\dot{\varepsilon}_r + \dot{\varepsilon}_\theta = 0$ and $\dot{\gamma}_{r\theta} = 0$. If the radial and circumferential velocities are denoted by u and v respectively, the velocity equations become

$$\frac{\partial u}{\partial r} + \frac{u}{r} + \frac{1}{r}\frac{\partial v}{\partial \theta} = 0 \quad \frac{\partial v}{\partial r} - \frac{v}{r} + \frac{1}{r}\frac{\partial u}{\partial \theta} = 0 \tag{C7}$$

The solution of these equations, giving an axially symmetrical distribution of velocities, with the center of curvature momentarily assumed to be fixed in space, may be written as

$$u = -\frac{1}{2\alpha}\left(r + \frac{c^2}{r}\right) \quad v = \frac{r\theta}{\alpha} \tag{C8}$$

where θ is measured from the vertical axis of symmetry, and α denotes the angle of bending per unit length, i.e., curvature. The components of the corresponding strain rate are found from the definition of strain in curvilinear coordinates (e.g. Chakrabarty 1987 p779) to be

$$-d\varepsilon_r = d\varepsilon_\theta = \left(1 - \frac{c^2}{r^2}\right)\frac{d\alpha}{2\alpha} \quad d\gamma_{r\theta} = 0 \tag{C9}$$

Since u depends only on r, the surfaces of the plate remain cylindrical, in accordance with the initial assumption. In view of the linear variation of v with r, the radial planes remain plane during the bending. It follows from (C8) that the instantaneous rates of change of the internal and external radii are

$$da = -\left(a + \frac{c^2}{a}\right)\frac{d\alpha}{2\alpha} = -\frac{a+b}{2\alpha}da \qquad db = -\left(b + \frac{c^2}{b}\right)\frac{d\alpha}{2\alpha} = -\frac{a+b}{2\alpha}da \tag{C10}$$

Thus $db - da = dh = 0$, which indicates that the plate thickness $h = b - a$ remains unchanged. The couple M is therefore independent of the amount of bending, the material being nonhardening. Denoting the original length of the plate by s, and equating the initial and final volumes, gives

$$s(b - a) = \frac{1}{2}(b^2 - a^2)s\alpha \quad \text{or} \quad \alpha = \frac{2}{a+b} \tag{C11}$$

It follows that the element which currently coincides with the central surface has undergone zero resultant change in length due to equal amounts of compression and extension during the bending.

Consider the movement of a typical element situated at a distance $eh/2$ from the central plane in the unbent state $(-1 \leq e \leq 1)$. Let r denote the current radius of the element in the bent state. Since the element divides the section into areas that remain constant during the bending,

$$\frac{r^2 - a^2}{b^2 - r^2} = \frac{1+e}{1-e} \tag{C12}$$

or

$$r^2 = \frac{1}{2}\left\{(b^2 + a^2) + e(b^2 - a^2)\right\} \tag{C13}$$

The original central element $(e = 0)$ moves to the convex side during bending, its radius of curvature in the final state being

$$r_0 = \sqrt{\frac{a^2 + b^2}{2}} \qquad\qquad (C14)$$

The initial position of the element finally coinciding with the neutral surface $(r = c)$ corresponds to $e = -(b-a)/(b+a)$. The neutral surface itself approaches the inner boundary from its initial position which coincides with the central plane. Hence, all elements initially above the central plane are progressively extended, while all elements finally inside the neutral surface are progressively compressed. The elements which are contained in the region corresponding to

$$-\left(\frac{b-a}{b+a}\right) < e < 0 \quad \text{or} \quad c < r < \sqrt{\frac{a^2 + b^2}{2}} \qquad\qquad (C15)$$

are first compressed and then extended, being overtaken by the neutral surface at some intermediate stage. In actual practice, therefore, these elements would be subjected to the Bauschinger effect.

At each stage of the bending, there is one element which has undergone equal amounts of compression and extension, and whose resultant change in length is zero. The radius of this element is, from (C11),

$$r = \frac{1}{\alpha} = \frac{1}{2}(a+b) \qquad\qquad (C16)$$

Thus, the element which has undergone no resultant change in length is that which coincides, at the moment under consideration, with the central surface of the plate. The initial position of the element that suffers equal amounts of extension and contraction is obtained by inserting (C16) into (C13): $2e = -(b-a)/(b+a)$. Since the bending occurs under constant couples form (C6), the work done per unit width is $M\alpha s$, and its value per unit volume is equal to $k(b-a)/(b+a)$. Figure C2 shows the initial and final positions of the unstretched element as well as those which define the region of reversed loading. Let the bent angle of the plate β. Since the unstretched element is at the center of the thickness, the lengths of the inside and outside elements are respectively

$$s - \frac{h\beta}{2}, \quad s + \frac{h\beta}{2}. \qquad\qquad (C17)$$

The strain distribution is linear across the thickness and the engineering strains of inside and outside are

$$\varepsilon_i = -\frac{h\beta}{2s}, \quad \varepsilon_o = \frac{h\beta}{2s}. \qquad\qquad (C18)$$

The true strains are

$$\varepsilon_{i,true} = \ln\left(1 - \frac{h\beta}{2s}\right), \quad \varepsilon_{o,true} = \ln\left(1 + \frac{h\beta}{2s}\right).$$ (C19)

4.   Bending Angle and Bending Strain

The thickness of the middle of the bending specimen was reduced, and fillets were introduced to reduce strain concentration. To calculate bending strains resulting from specimen bending, model the specimen as three parts, one uniformly bending part and two rigid parts, which are shown in Figure C3. The bending part has a thickness of h and length of s_{eff}. The rigid parts have a length l_{eff}. These effective lengths are functions of the geometry shown in Figure C3 and C4, i.e.,

$$s_{eff} = f\left(s_h, h, R_C\right), \quad l_{eff} = g\left(s_h, h, h_p, R_C, l_p\right)$$ (C20)

where l_p is half of the pin hole distance. For a more precise evaluation, s_{eff} and l_{eff} should also be functions of bend angle β. However, in the following analyses, the variation of them during bending was assumed small enough to be neglected.

Let the inside and outside radii of the bent part be R_i and R_o respectively. The radius of unstretched plane is

$$R_u = \frac{R_i + R_o}{2} \quad \text{where} \quad R_0 = R_i + h$$ (C21)

From now on, redefine θ to be the angle of the bent specimen shown in Figure C3. The relation between θ and the bending angle β is

$$\theta + \beta = \pi .$$ (C22)

From (C18), the inside and outside strains are

$$\varepsilon_i = -\frac{h(\pi - \theta)}{2s_{eff}}, \quad \varepsilon_o = \frac{h(\pi - \theta)}{2s_{eff}} .$$ (C23)

Using the radii,

$$\varepsilon_o, -\varepsilon_i = \frac{h}{2R_u} = \frac{R_0 - R_i}{R_0 + R_i}$$ (C24)

5.   Bending Angle Increment and Bending Strain Increment

137

Consider a bending increment $\Delta\alpha$ of either sign on a bent plate whose central length is s, curvature is α_0, and inner and outer radii are a_0 and b_0 as mentioned in Section 3. After the bending increment, the curvature becomes

$$\alpha_1 = \alpha_0 + \Delta\alpha,$$

(C25)

and the radii become a_1 and b_1. Equating the volumes before and after the bending increment gives

$$\frac{1}{2}\left(b_0^2 - a_0^2\right)s\alpha_0 = \frac{1}{2}\left(b_1^2 - a_1^2\right)s\alpha_1$$

(C26)

From Equations in (C10), the plate thickness remains unchanged during any increment of bending:

$$h = b_0 - a_0 = b_1 - a_1$$

(C27)

With Equations (C11) and (C27), (C26) turns out to be

$$\alpha_1 = \frac{\alpha\left(b_0 + a_0\right)}{b_1 + a_1} = \frac{2}{b_1 + a_1}$$

(C28)

It follows again that the element whose length is s still coincides with the central surface after the bending increment.

Consider the current bent plate shown in Figure C1. The inside and outside radii are

$$a = \frac{1}{\alpha} - \frac{h}{2}, \quad b = \frac{1}{\alpha} + \frac{h}{2}$$

(C29)

By an infinitesimal increment of bending angle, the curvature of the central plane increases by $d\alpha$. The increment of strain on the inside and outside surfaces are, from (C9) and (C4),

$$d\varepsilon_i = \left(1 - \frac{c^2}{a^2}\right)\frac{d\alpha}{2\alpha} = \left(1 - \frac{b}{a}\right)\frac{d\alpha}{2\alpha} = \left(1 - \frac{2/h + \alpha}{2/h - \alpha}\right)\frac{d\alpha}{2\alpha}$$

$$= \frac{-d\alpha}{2/h - \alpha}$$

(C30)

$$d\varepsilon_o = \left(1 - \frac{c^2}{b^2}\right)\frac{d\alpha}{2\alpha} = \left(1 - \frac{a}{b}\right)\frac{d\alpha}{2\alpha} = \left(1 - \frac{2/h - \alpha}{2/h + \alpha}\right)\frac{d\alpha}{2\alpha}$$

$$= \frac{d\alpha}{2/h + \alpha}$$

(C31)

Integrating (C30) and (C31) respectively from α_0 to α_1 gives

$$\Delta\varepsilon_i = \ln\left(\frac{1 - \alpha_1 h/2}{1 - \alpha_0 h/2}\right)$$

(C32)

$$\Delta\varepsilon_o = \ln\left(\frac{1+\alpha_1 h/2}{1+\alpha_0 h/2}\right) \tag{C33}$$

To derive the relation between the end displacement and additional strain increment in the following section, dimensional variables are introduced here. Furthermore, a linear expression for the additional strain versus the additional bending angle will be derived. For the bent plate whose arc length is s_{eff} and pre-bend angle is β_{pre}, the inside and outside strains due to the bending increment $\Delta\beta$, i.e., for the bend angle $\beta = \beta_{pre}+\Delta\beta$, is

$$\Delta\varepsilon_i = \ln\left(\frac{1-\beta/s_{eff}\cdot h/2}{1-\beta_{pre}/s_{eff}\cdot h/2}\right) = \ln\left(1 - \frac{\Delta\beta/s_{eff}}{2/h - \beta_{pre}/s_{eff}}\right) \tag{C34}$$

$$\Delta\varepsilon_o = \ln\left(\frac{1+\beta/s_{eff}\cdot h/2}{1+\beta_{pre}/s_{eff}\cdot h/2}\right) = \ln\left(1 + \frac{\Delta\beta/s_{eff}}{2/h + \beta_{pre}/s_{eff}}\right) \tag{C35}$$

These are exact solutions for strain increments. Figure C5 shows the inside increment strain vs. the reversed bending angle increment $-\Delta\beta$. Equations (C34) and (C35) can be expanded in the following form of series because the absolute values of the second terms are smaller than unity.

$$\Delta\varepsilon_i = -\frac{\Delta\beta/s_{eff}}{2/h - \beta_{pre}/s_{eff}} - \frac{1}{2}\left(\frac{\Delta\beta/s_{eff}}{2/h - \beta_{pre}/s_{eff}}\right)^2 - \cdots - \frac{1}{n}\left(\frac{\Delta\beta/s_{eff}}{2/h - \beta_{pre}/s_{eff}}\right)^n - \cdots \tag{C36}$$

$$\Delta\varepsilon_o = \frac{\Delta\beta/s_{eff}}{2/h + \beta_{pre}/s_{eff}} - \frac{1}{2}\left(\frac{\Delta\beta/s_{eff}}{2/h + \beta_{pre}/s_{eff}}\right)^2 + \cdots + (-1)^{n-1}\frac{1}{n}\left(\frac{\Delta\beta/s_{eff}}{2/h + \beta_{pre}/s_{eff}}\right)^n + \cdots \tag{C37}$$

For the practical range of β_{pre} = 60 to 135 degrees and $\Delta\beta$ = 0 to –80 degrees with s_{eff} = 25.4 mm and h = 9.525 mm of the reverse bending conditions, (C34) is well approximated within 7 % of the largest strain increment by using the first term of (C36) modified by the factor of 0.88, (see Figure C5)

$$\Delta\varepsilon_i = -\frac{0.88\,\Delta\beta/s_{eff}}{2/h - \beta_{pre}/s_{eff}} \tag{C38}$$

6. End Displacement and Reverse Bending Strain

Consider the changing separation x between the two pins. The additional bending strain resulting from the change of the separation will be obtained here. For increasing x, the angle of the bent specimen θ increases and the bend angle β decreases. For the angle increment of $\Delta\theta$

139

from the pre-strain bend angle β_{pre}, the inside strain increment is, from (C38)

$$\Delta\varepsilon_i = \frac{0.88\Delta\theta/s_{\mathit{eff}}}{2/h - \beta_{pre}/s_{\mathit{eff}}}$$ (C39)

From geometry in Figure C3,

$$w = 2\left(\frac{s_{\mathit{eff}}}{\beta} + \frac{h}{2}\right)\sin\frac{\beta}{2} = \left(\frac{2s_{\mathit{eff}}}{\pi-\theta} + h\right)\cos\frac{\theta}{2}$$ (C40)

$$2l_{\mathit{eff}}\sin\frac{\theta}{2} = x - w$$ (C41)

The pin separation is now expressed as

$$x = 2l_{\mathit{eff}}\sin\frac{\theta}{2} + \left(\frac{2s_{\mathit{eff}}}{\pi-\theta} + h\right)\cos\frac{\theta}{2} \,.$$ (C42)

In the range from θ = 45 to 120 degrees with l_{eff}= 90 mm, s_{eff}= 25.4 mm and h = 9.525 mm, the change of the second term w is less than 0.9% of x and almost constant compared with the first term. Therefore, (C42) can be well approximated as

$$x = 2l_{\mathit{eff}}\sin\frac{\theta}{2} + w_0 \quad \text{where } w_0 \text{ is a constant.}$$ (C43)

Consider the pin separation increment Δx from the initial value x_0, and the corresponding angle increment $\Delta\theta$ from θ_0. Equation (C43) results in:

$$x_0 + \Delta x = 2l_{\mathit{eff}}\sin\frac{\theta_0 + \Delta\theta}{2} + w_0$$ (C44)

$$x_0 = 2l_{\mathit{eff}}\sin\frac{\theta_0}{2} + w_0 \quad \Delta\theta = 0$$ (C45)

Subtracting the both sides of (C45) from (C44) gives

$$\Delta x = 2l_{\mathit{eff}}\left[\sin\left(\frac{\theta_0 + \Delta\theta}{2}\right) - \sin\frac{\theta_0}{2}\right]$$ (C46)

Solution for $\Delta\theta$ is

$$\Delta\theta = 2\arcsin\left(\frac{\Delta x}{2l_{\mathit{eff}}} + \sin\frac{\theta_0}{2}\right) - \theta_0$$ (C47)

Combining (C39) and (C47) with (C22), for an increment of end displacement Δx, the additional bending inside strain is

$$\Delta\varepsilon_i = \frac{0.88}{s_{\mathit{eff}}/h - \pi/2 + \theta_0/2}\left[\arcsin\left(\frac{\Delta x}{2l_{\mathit{eff}}} + \sin\frac{\theta_0}{2}\right) - \frac{\theta_0}{2}\right]$$ (C48)

For positive Δx, the additional strain is reversed strain in the bent part. Figure C6 shows examples of reverse strain to the end displacement from various initial angles for l_{eff}= 90 mm, s_{eff} = 25.4 mm and h = 9.65 mm as an average of thickness after bending tests.

References

CHAKRABARTY, J.   1987   *Theory of Plasticity*, McGraw-Hill, N.Y., pp 741–746

HILL, R.   1950   *The Mathematical Theory of Plasticity*, pp 287-294, Clarendon Press, Oxford.

LUBAHN, J. D. AND SACHS, G.   1950   *Trans. ASME*, **72**, 201
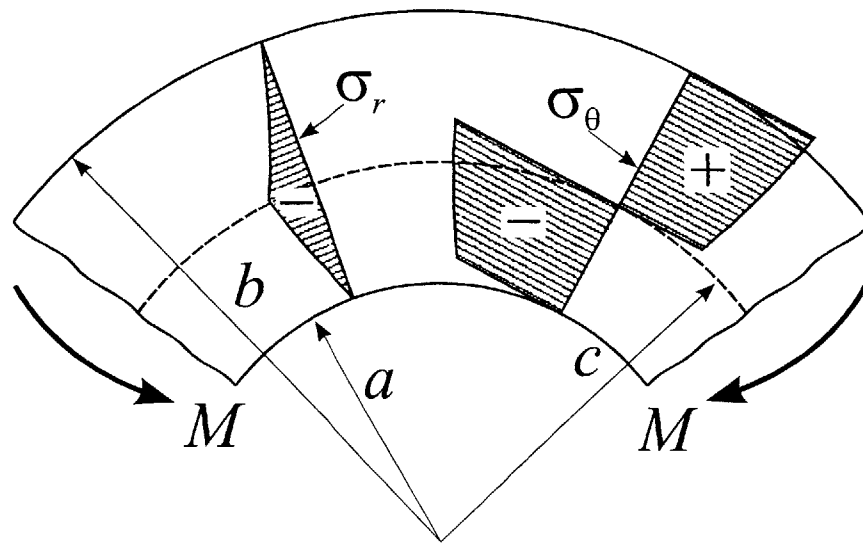
Figure C1   Stress distribution in the plane strain bending of a wide plate.
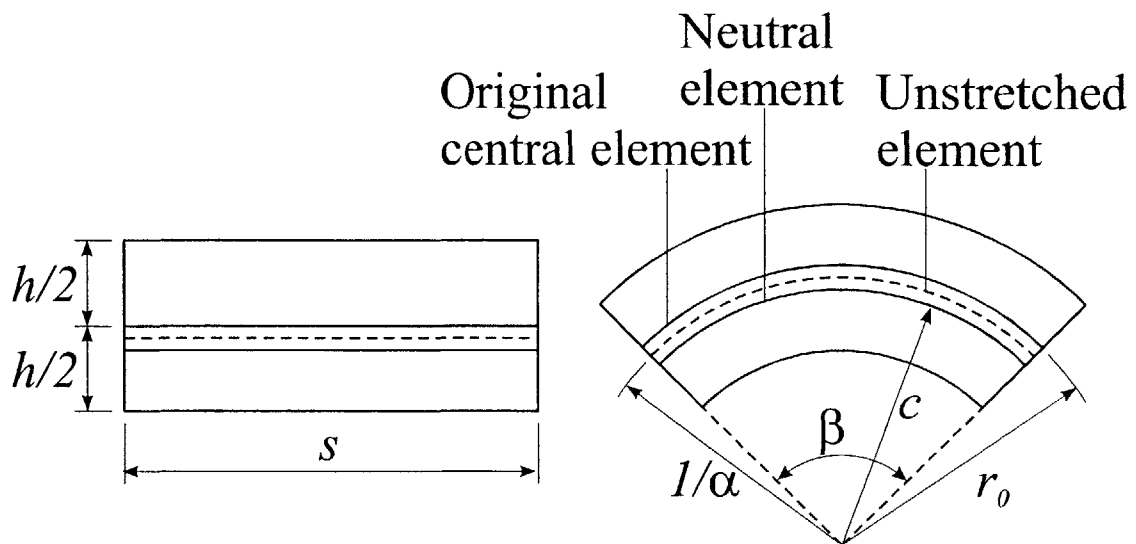
Figure C2   Relative movement of selected longitudinal elements in plate bending.
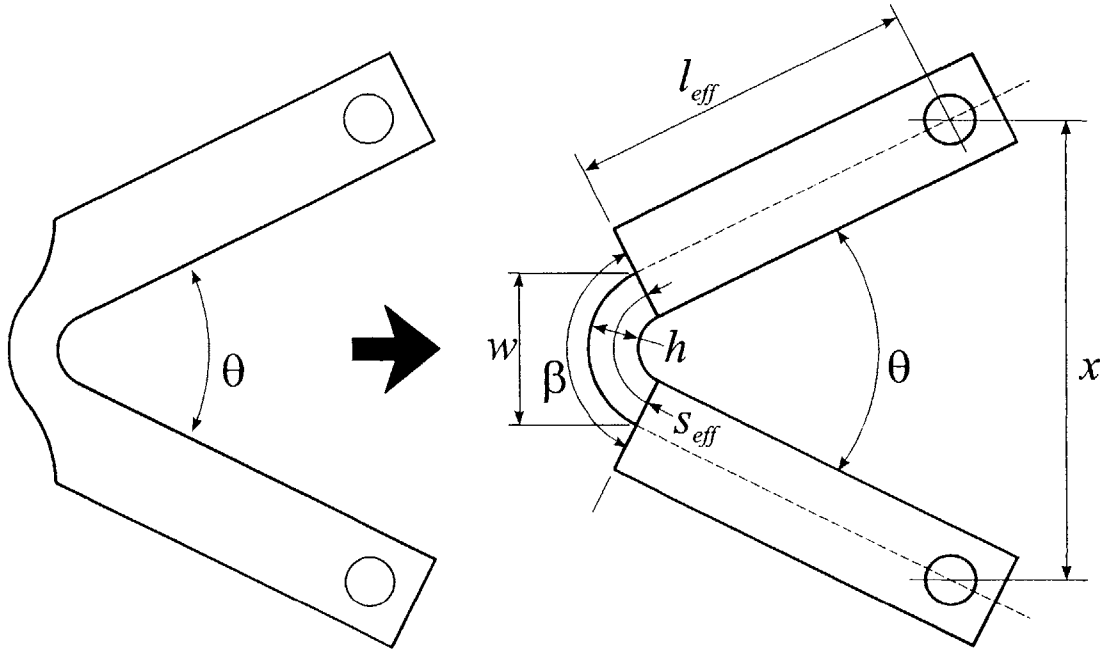
Figure C3   Bending Specimen Modeling
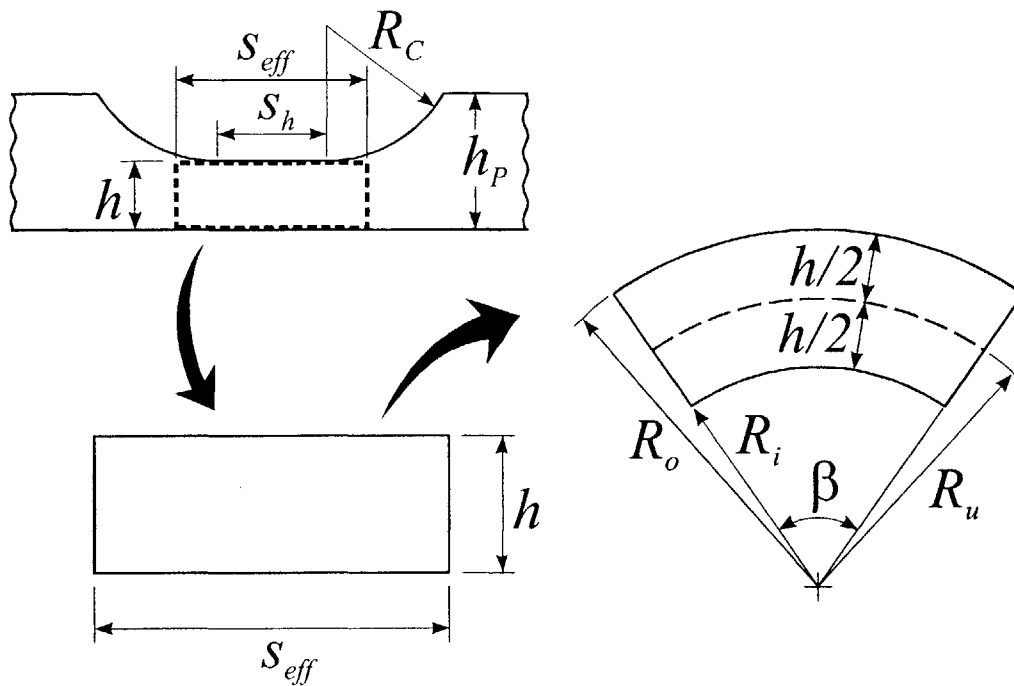
Figure C4   Effective bending portion of bending specimen

143
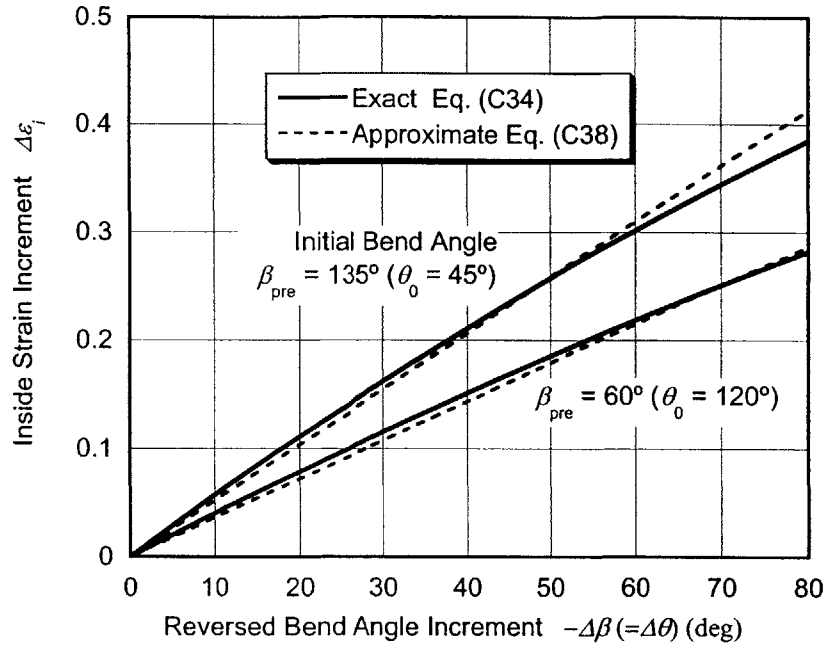
Figure C5　*Inside strain increment from pre-strain bend angle β_{pre} vs. reversed bend angle increment $-\Delta\beta$ $(=\Delta\theta)$, $s/h = 2.67$*
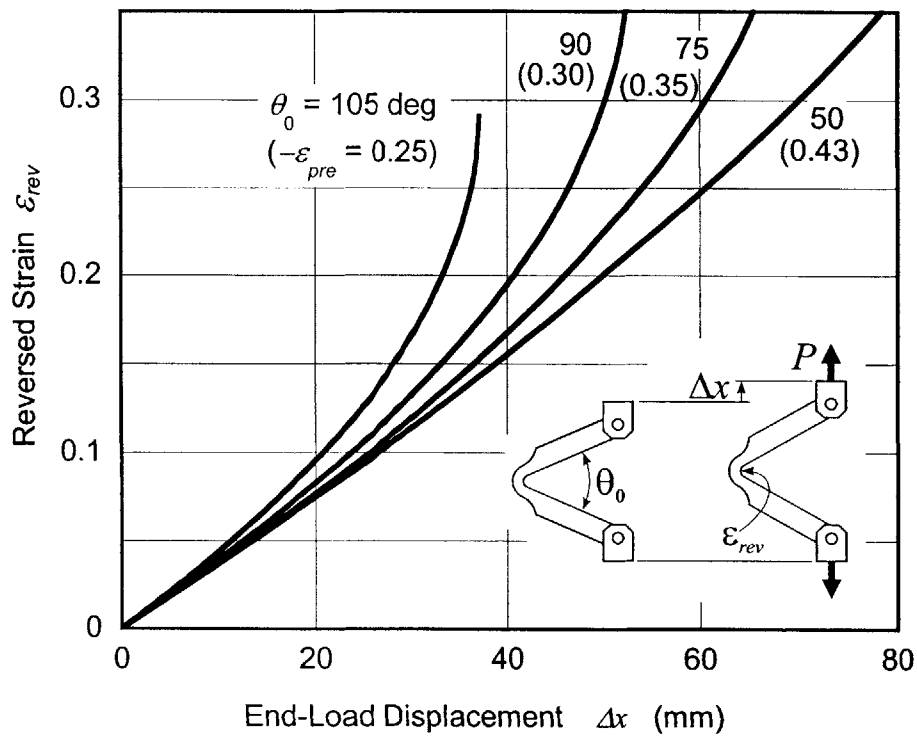
Figure C6　*Reverse strain to end-load displacement $l_{eff} = 90$ mm, $s_{eff} = 25.4$ mm and $h = 9.65$ mm*

Appendix D   Average Grain Size of AH36

Summary

The average grain size of the reverse bending specimen taken from AH36 steel plate was measured based on the ASTM E112-96 (1997). The average grain size was 0.0696±0.0064 mm with 95% confidence. The ASTM grain size number was 5.7.

1.   Objective

It is well known that there is a correlation between the toughness of steel and its grain size. The average grain size of ABS AH36 steel plate, from which the reverse bending specimens were taken, was measured for the future reference. The observed surface was the L-S plane, parallel to the rolling direction and perpendicular to the rolled surface. The plane coincides with the crack surface of the reverse bending tests. The measurement followed ASTM (1997) to give the ASTM grain size number.

2.   Specimen Sampling

A microscopic observational sample was taken from one Charpy V-notch specimen tested at –25 °C as shown in Figure D1. The observational section is taken on the plane normal to T-direction and perpendicular to plate surface. It coincides with the crack surfaces of the reverse bending specimens and the Charpy V-notch specimens. The observed point was taken 7 mm below the hot-rolled surface.

3.   Grain Counting

The whole test method followed ASTM E112-96 (1997).

The magnification ×80 was used. The three photomicrographs taken from the observed section point are shown in Figure D2.

The intercept procedures specified by ASTM E112 were employed to measure the grain

size. Five horizontal and five vertical straight lines were randomly drawn on each photomicrograph.

On measurements, each variable is defined as follows.

$\overline{D}$	mean spatial (volumetric) grain diameter
G	ASTM grain size number
$\overline{\ell}$	mean lineal intercept length
s	standard deviation
95%CI	95% confidence interval
%RA	percent relative accuracy

$$\overline{\ell} = \frac{\sum \ell_i}{n}$$

where ℓ_i represents an individual value of ℓ, $\overline{\ell}$ is the mean and n is the number of measurements. The other values are defined as follows.

$$s = \left[\frac{\sum \left(\ell_i - \overline{\ell}\right)^2}{n-1} \right]^{1/2}$$

$$95\%CI = 1.96 \frac{s}{\sqrt{n}}$$

$$\%RA = \frac{95\%CI}{\overline{X}} \cdot 100$$

$$\overline{D} = 1.571 \overline{\ell}$$

$$G = -6.643856 \log_{10} \overline{\ell} - 3.288, \quad \overline{\ell} \text{ in mm}$$

4. Results

The grain shapes were equiaxed. Ferrite, pearlite and bainite grains were observed exclusively. Each of the ferrite, pearlite or bainite grains was counted as one grain.

The results are:

Number of photomicrographs		3
Number of lines		30
Number of intercepts counted		821
Mean lineal intercept length	$\overline{\ell}$	0.0443 mm

Standard deviation for $\bar{\ell}$	s	0.0115 mm
95% confidence interval for $\bar{\ell}$	95%CI	0.0041 mm
Percent relative accuracy for $\bar{\ell}$	%RA	9.29 %
Mean spatial (volumetric) grain diameter	$\bar{D}$	0.0696±0.0064 mm
ASTM grain size number	G	5.71±0.27

The percent relative accuracy was less than the ASTM requirement of 10%, and the grain size number can be expressed as a single number.

5.   Conclusions

The average volumetric grain diameter of the reverse bending specimen made of AH36 measured by the intercept method specified by ASTM E112 was 0.0696±0.0064 mm with 95% confidence. The corresponding ASTM grain size number is 5.7±0.27 (95%).

Reference

ASTM E112-96   1997   Standard Test Methods for Determining Average Grain Size, *Annual Book of ASTM Standards*, **03.01** July
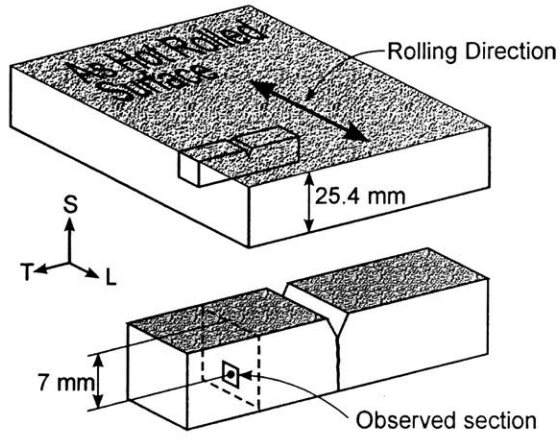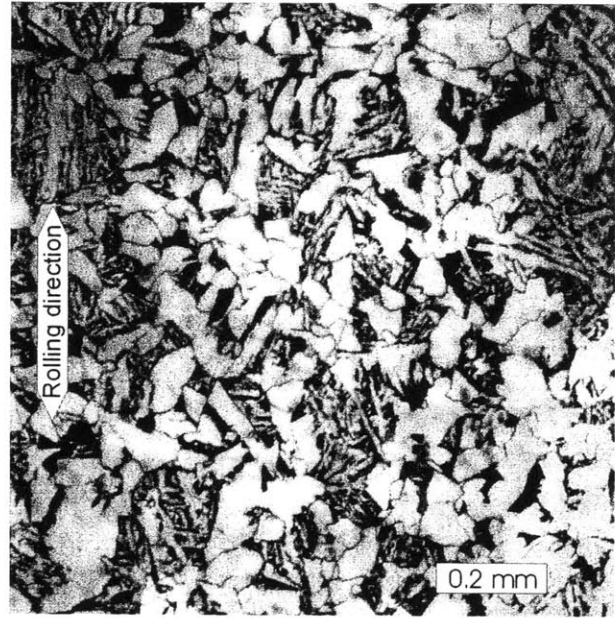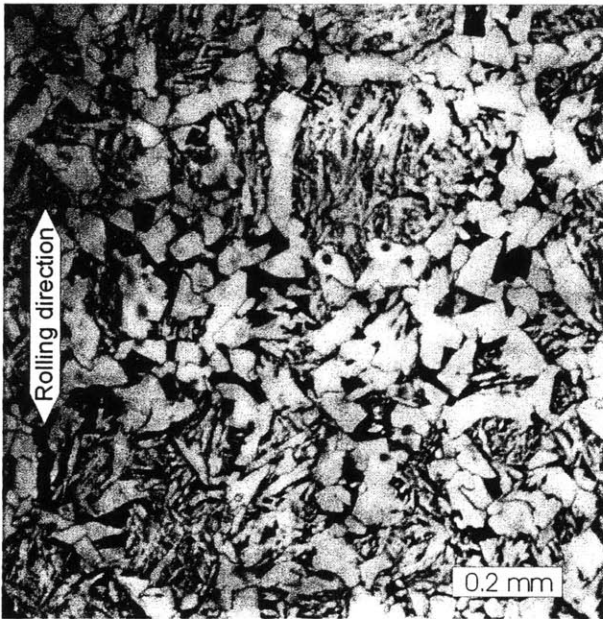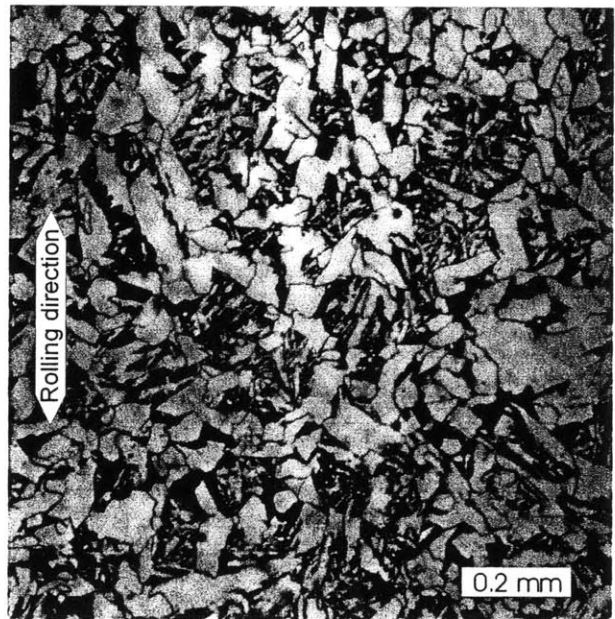
Figure D1   Specimen sampling

(a) Photo 1

(b) Photo 2

(c) Photo 3

Figure D2   Magnified grain images on the plane normal to the transverse direction

Appendix E   Stress - Strain Curve of AH36

Summary

To obtain mechanical properties of the high-strength ship steel AH36 in the transverse direction, tensile tests were carried out. The 0.2 % offset yield strength was 322 MPa, the tensile strength was 621 MPa, and the fracture strength was 1112 MPa.

1.   Objective

To obtain reference data for the reverse bending cleavage tests using high-strength structural steel for hulls, AH36, tensile tests were carried out. The tensile specimens were taken parallel to the transverse rolling direction so that the largest strain occurs in the same direction as in the bending tests. The stress-strain curve, 0.2 % offset yield strength, tensile strength, elongation and fracture strength were obtained.

2.   Specimen

Three round specimens with 6.35 mm diameter, shown in Figure E1, were machined from a one-inch-thick AH36 steel plate, which was in the same heat as the plate for the bending speci-mens. The specimens were taken in the middle of the plate thickness, and their long direction coincided with the transverse rolling direction. Table E1 shows the properties of AH36 provided by the supplier. Note that the carbon content 0.179 % is rather high for ABS and ASTM stan-dards which specify the maximum of carbon content is 0.18 %.

3.   Tensile Test Procedure

The tensile strain up to 20 % nominal strain was measured by an extensometer with a 25.4 mm gauge length. The machine head displacement was also recorded to extrapolate the tensile strain above the range of the extensometer. The tensile load was measured by the 100 kN load cell of the testing machine.

The head motion was controlled at a constant rate of 1 mm/min up to about 3 % strain, and

2 mm/min after that. The data were recorded every 1.9 seconds until the specimens fractured.

4. Results

The tensile test setup with the extensometer is shown in Figure E2. The detailed data are shown in Table E2. No yield point was observed. Therefore, yield stresses were taken as 0.2 % strain stresses.

Nominal strains were calculated as follows.

For the gauge length l_G (= 25.4 mm), the effective specimen length L_{eff} (= 76.2 mm), and the machine head displacement u,

$$\varepsilon \equiv \frac{\Delta l_G}{l_G} \qquad \text{for } \varepsilon < \varepsilon_{MAX} \tag{E1}$$

$$\varepsilon \equiv \varepsilon_{MAX} + \Delta \varepsilon \quad \text{for } \varepsilon \geq \varepsilon_{MAX} \tag{E2}$$

$$\text{where} \quad \varepsilon_{MAX} \equiv \frac{\Delta l_G}{l_G} \text{ at the maximum load} \tag{E3}$$

$$\Delta \varepsilon \equiv \frac{u_{MAX} - u}{L_{eff}} \tag{E4}$$

and u_{MAX} is the machine head displacement at the maximum load. (Note: To compare with a standard specimen, Leff should be modified appropriately based on ASTM E8-96a (1997) or ASTM E8-97 (1997).

The diameter of the fracture sections was measured with a vernier caliper.

The nominal elongation to fracture was measured over 63.5 mm (2.5 in) using the machine head displacement corrected at the maximum load with readings from the extensometer.

Tensile strengths, fracture strengths and fracture strains were calculated using the following equations.

Tensile strength

$$\sigma_u = \frac{P_{MAX}}{A_0} \tag{E5}$$

Fracture strength

$$\sigma_f = \frac{P_f}{A_f} \tag{E6}$$

Fracture strain

$$\varepsilon_f = \frac{A_0}{A_f} - 1 \tag{E7}$$

where P_{MAX} is the maximum load, P_f is the load at fracture, A_0 is the initial sectional area, and A_f is the sectional area at fracture.

Nominal and true stress strain curves are shown in Figures E4 to E9. The true stresses σ_{true} and the true strains ε_{true} before necking were calculated from nominal stresses $\sigma_{nominal}$ and strains $\varepsilon_{nominal}$ using the following equations, and shown as solid lines in those figures.

$$\sigma_{true} = \sigma_{nominal}\left(1 + \varepsilon_{nominal}\right) \tag{E8}$$

$$\varepsilon_{true} = \ln\left(1 + \varepsilon_{nominal}\right) \text{ before necking} \tag{E9}$$

$$\sigma_{nominal} = \frac{P}{A_0} \tag{E10}$$

where P is the load, and A_0 is the initial sectional area.

After necking, nominal stresses were calculated still using Equation (E10). The curves for true stresses and strains, shown by broken lines in the figures, were drawn to connect the solid lines and their fracture points smoothly on the plots. For comparison, the stress strain curves for the all three specimens are superimposed in Figures E10 and E11.

For the plastic strains larger than 0.002 obtrained by the tensile specimens, the best fit power-low curve yields a power hardening exponent $N = 0.187$ to 0.154.

$$\sigma_{true} = 1045\left(\varepsilon_{true}\right)^{0.187} \sim 990\left(\varepsilon_{true}\right)^{0.154} \tag{E11}$$

The comparison of measured and power-low curves is shown in Figure E12 with the fracture points.

5. Conclusion

While the yield stress and tensile strength for AH36 provided by the supplier were 380.6 MPa and 590.9, those obtained by the tensile tests were 322.2 MPa and 621.1 MPa. Note that, although there was no information about the orientation of tensile specimens in the data from the supplier, it seems to be rolling direction and the data obtained here were for the transverse to the rolling direction. The power hardening exponent was 0.187.

Reference

ASTM E8-96a 1997 Standard Test Methods for Tension Testing of Metallic Materials, *Annual*

Book of ASTM Standards, **03.01** July

ASTM E8-97   1997   Standard Test Methods for Tension Testing of Metallic Materials [Metric],
   Annual Book of ASTM Standards, **03.01** July
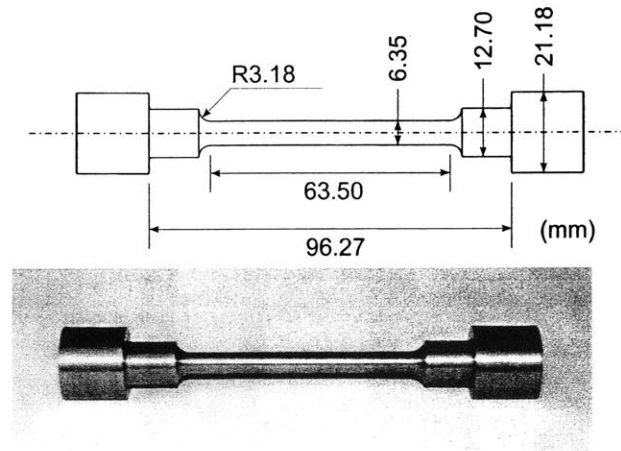
Figure E1   *Tensile specimen taken from AH36 steel*

Table E1   *Properties of high strength steel AH36 (supplier's data)*

Chemical composition, %								
C	Mn	Si	P	S	Cr	Ni	Al	Cu
0.179	1.56	0.441	0.016	0.006	0.03	0.18	0.053	0.153
Ti	N	Nb	V	Mo	Ca	Sn	B	
0.003	0.007	0.003	0.005	0.054	0.0002	0.002	0.0002	

Mechanical Parameters in L-direction (rolling direction)		
Yield Point MPa	Tensile Strength MPa	
380.6	590.9	

Table E2   *Mechanical parameters of high strength steel AH36 in T-(long transverse) direction (measured data)*

	Final Load (N)	Fracture Section Diameter (mm)	Elongation over 2.5 in. (%)	0.2% Yield Strength (MPa)	Tensile Strength (MPa)	True Fracture Strength (MPa)	True Fracture Strain (%)
Specimen 1	15101.	4.12	18.4	309.6	615.8	1133.	137.5
Specimen 2	16001.	4.35	19.6	334.2	620.2	1077.	113.1
Specimen 3	15672.	4.21	21.1	322.8	621.9	1126.	127.5
Average	15591.	4.23	19.7	322.2	621.1	1112.	126.0
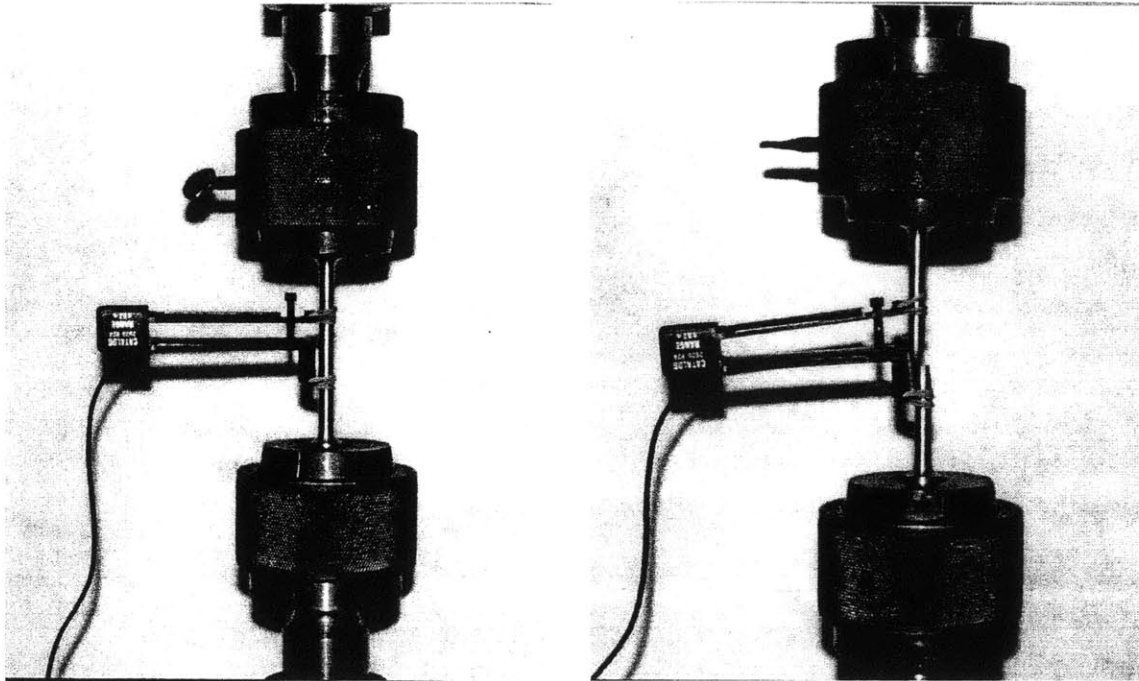
Figure E2   *Tensile test setup with an extensometer*

(1)   (2)   (3)
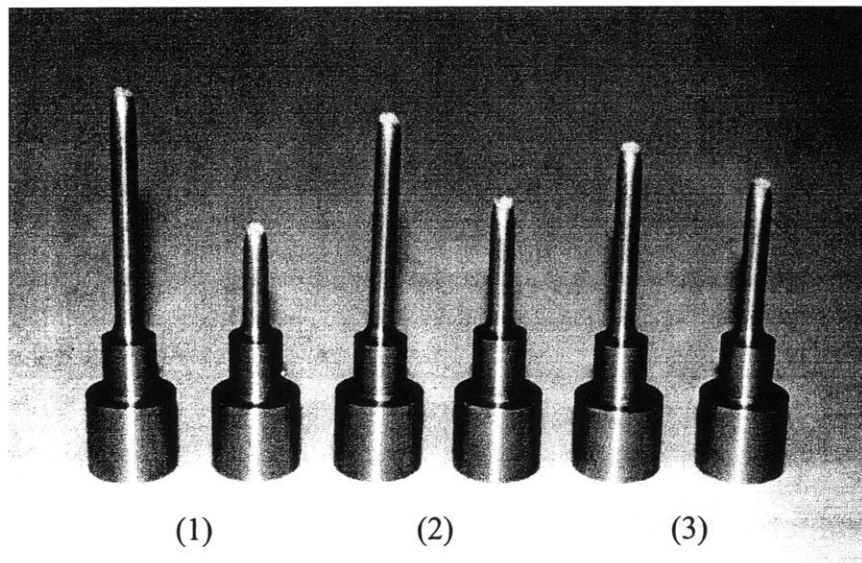
Figure E3   *Tested specimens*
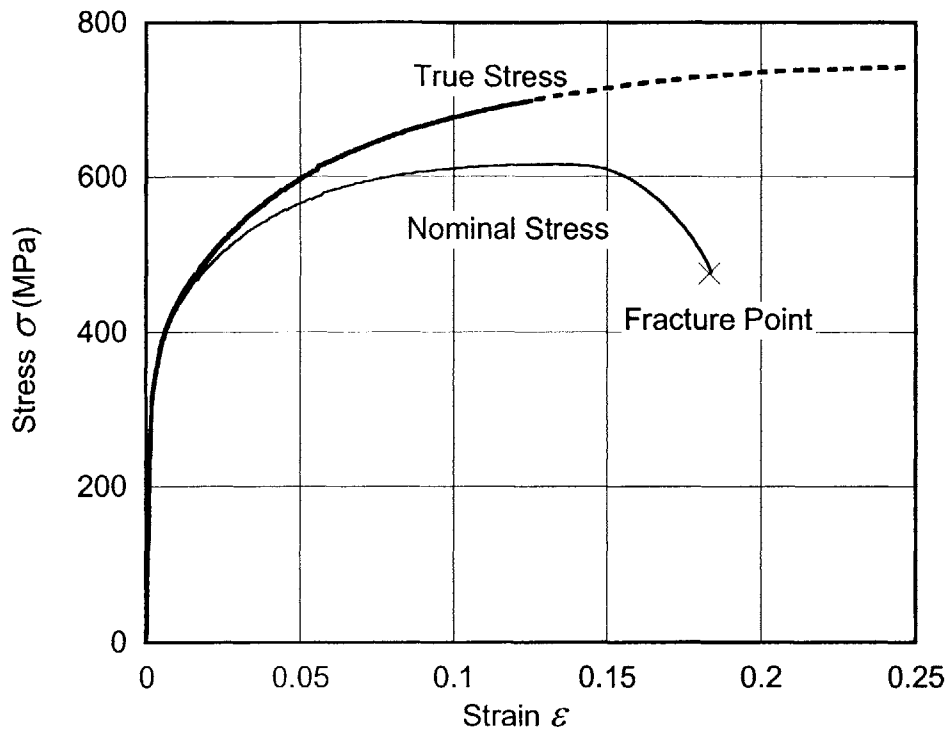
Figure E4   Stress strain curves for specimen 1 (up to ε = 0.25)
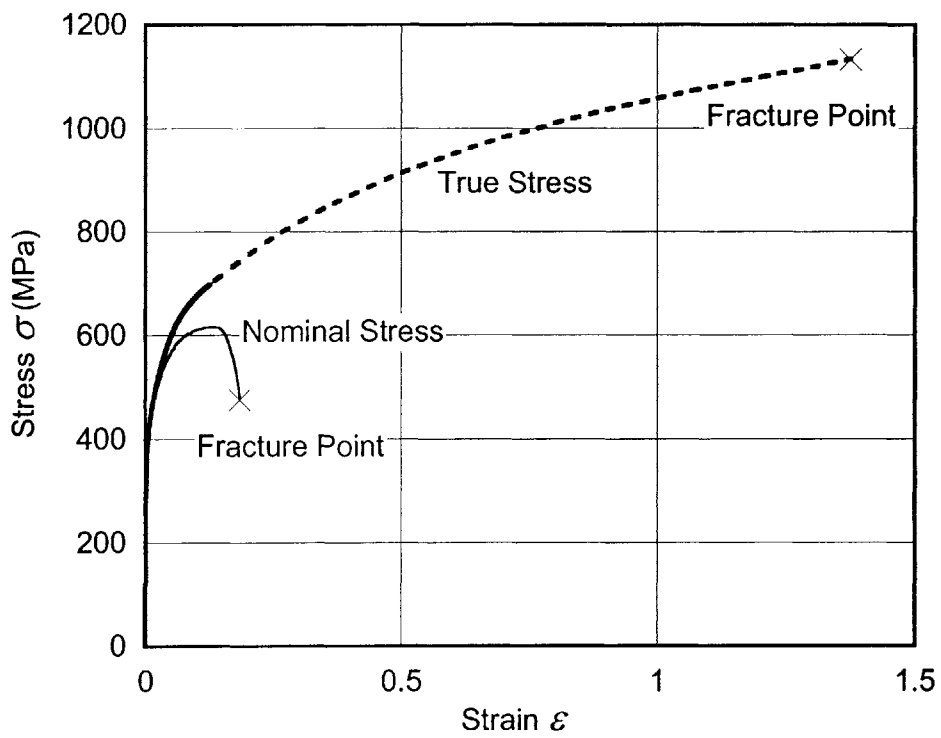
Figure E5   Stress strain curves for specimen 1 (up to ε = 1.5)
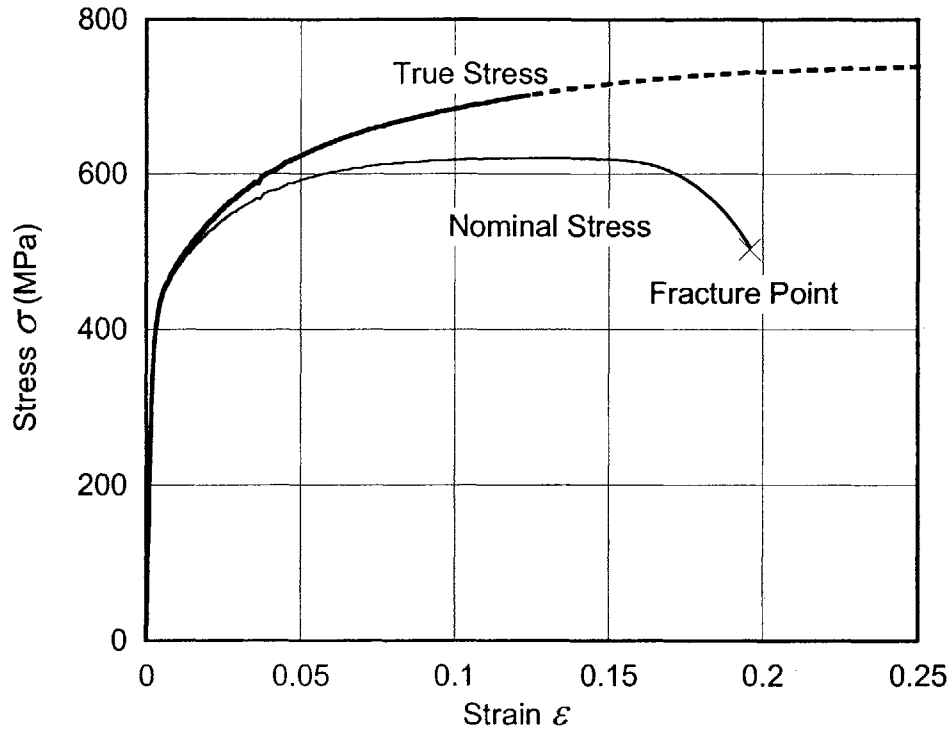
Figure E6   *Stress strain curves for specimen 2 (up to $\varepsilon = 0.25$)*
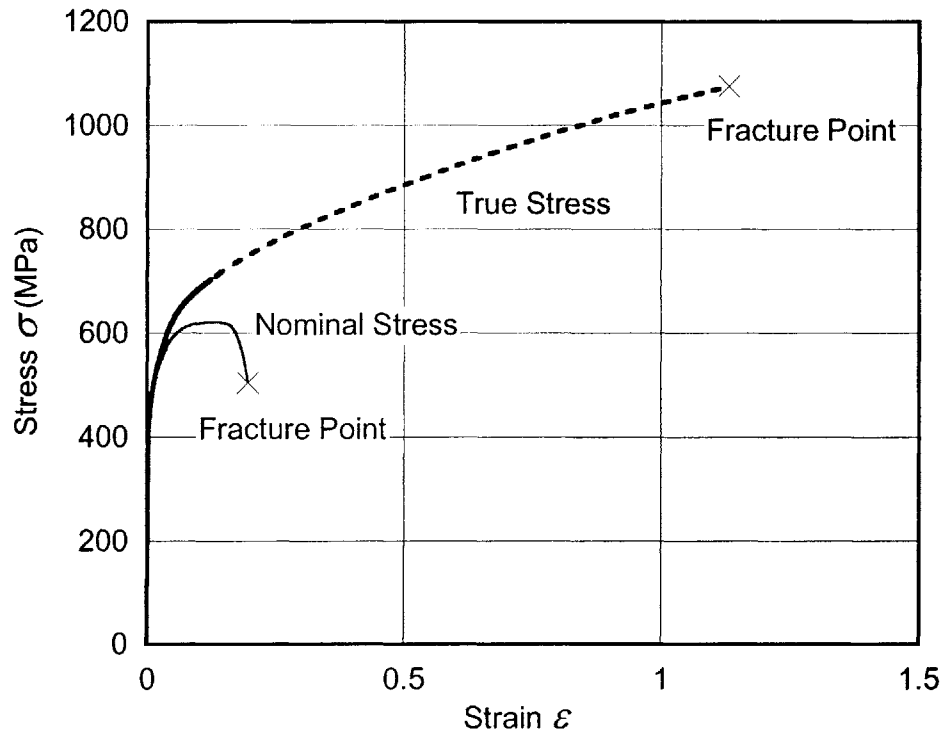
Figure E7   *Stress strain curves for specimen 2 (up to $\varepsilon = 1.5$)*
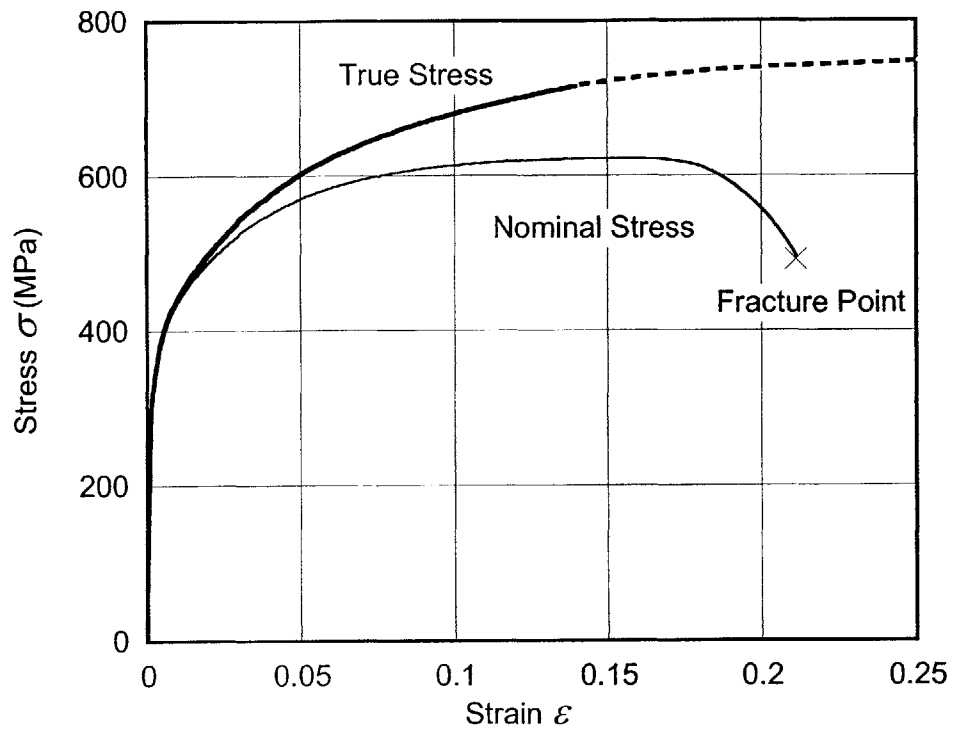
Figure E8   *Stress strain curves for specimen 3 (up to ε = 0.25)*
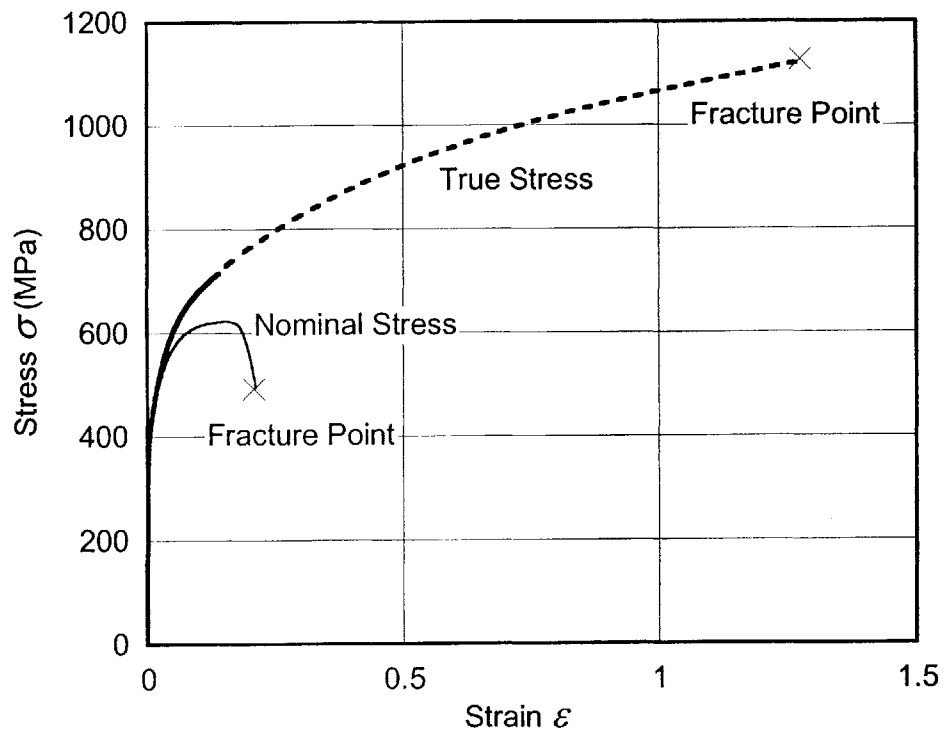
Figure E9   *Stress strain curves for specimen 3 (up to ε = 1.5)*
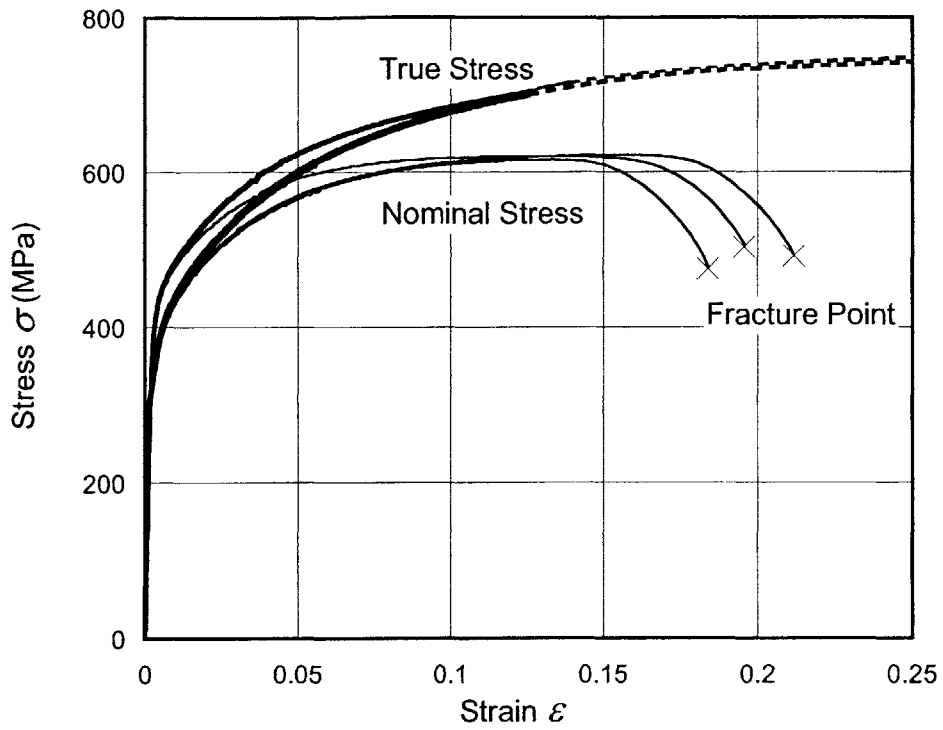
Figure E10   *Stress strain curves for all 3 specimens (up to ε = 0.25)*
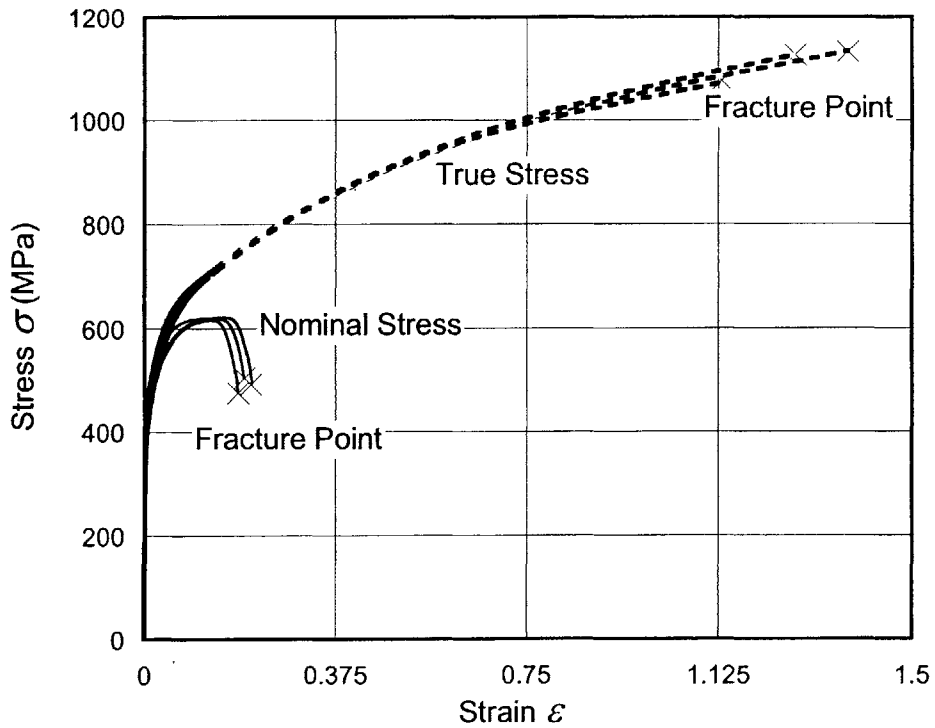
Figure E11   *Stress strain curves for all 3 specimens (up to ε = 1.5)*
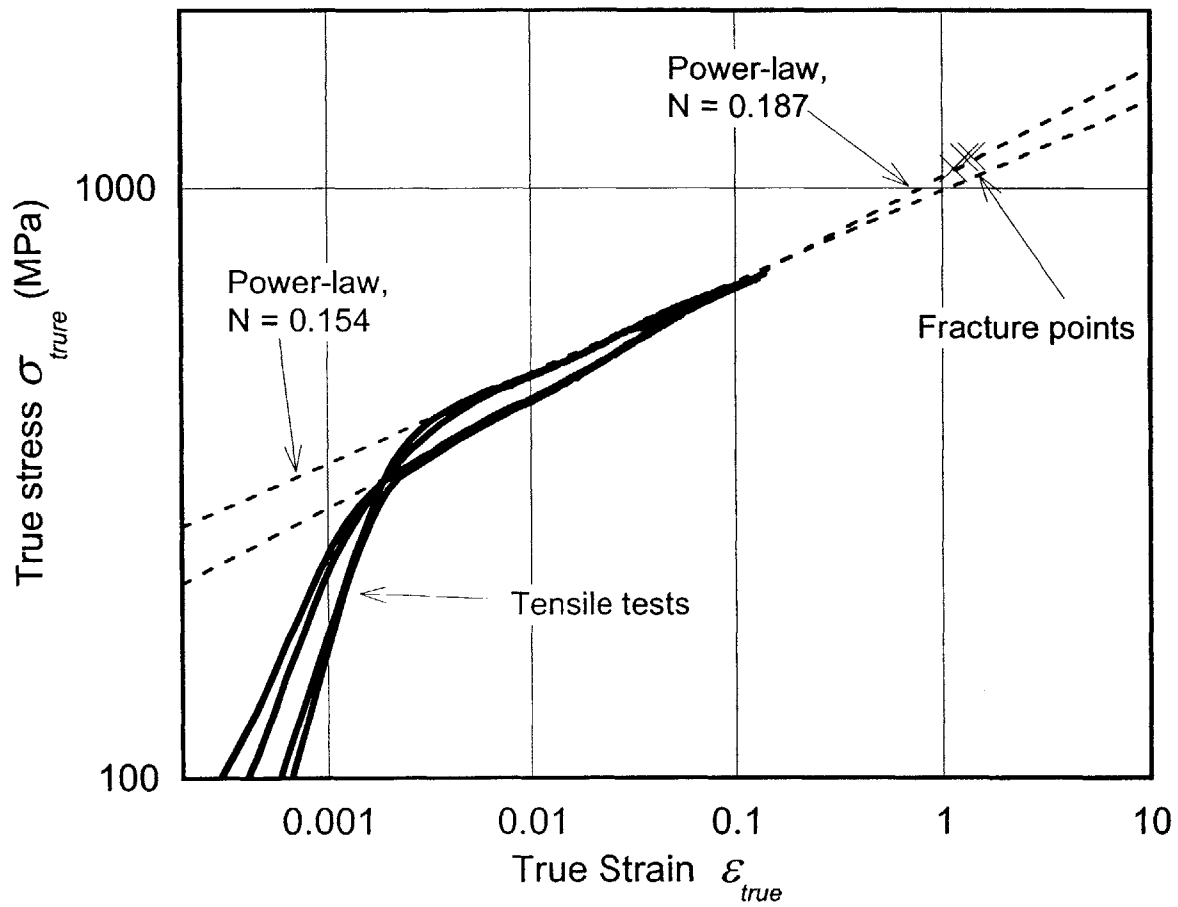
Figure E12   Stress - strain curves by tests and by power law with N = 0.154 and 0.187

Appendix F   Charpy V-notch Impact Tests

1.   Summary

Charpy V-notch impact tests were carried out to obtain the Charpy work transition temperature of the high tensile strength steel ABS AH36. The transition occurred over –25 to 100 °C. There was no difference between longitudinal and transverse specimens.

2.   Introduction

When a brittle-to-ductile transition in the fracture modes is described for steels, impact tests such as Charpy work are usually referred. In the reverse bending cleavage tests using plate specimens, the temperature and the pre-strain are the essential parameters that rule the cleavage conditions to cause cleavage fracture on reversed bending. There was also a fracture mode transition temperature in the reverse bending tests. To compare the reverse bending transition with the standard Charpy work transition temperature, Charpy V-notch impact tests were carried out using transverse and longitudinal specimens. They were taken from the same AH36 steel plate as the bending specimens.

3.   Method

The Charpy specimens were machined from the ABS AH36 plate from which the reverse bending test specimens were cut. The sampling map is shown in Figure F1. The reverse bending specimens were cut along the as-rolled plate surface in the transverse direction (see Figure I1 in Appendix I). This gives the impending crack surface normal to the transverse direction, and crack growth direction normal to the plate (T-S orientation). For the consistency of material composition and crack growth direction, all Charpy specimens were cut out along the plate surface, with notches machined on the original rolled surface, as shown on the sampling map of Figure F1. Twelve were in the transverse direction T, and six were in the longitudinal direction L, along the rolling direction. These give T-S and L-S cracking orientations. While the ABS (1984) and ASTM E23-96 (1997) specify that the length along the notch is to be perpendicular to the original rolled surface (T-L or L-T orientation), here the twelve specimens were chosen with

the T-S orientation for consistency with the reversed bending plate specimens.

The temperature range was taken from –25 to 145 °C.

4. Results

Table F1 shows all results obtained. Figure F2 shows the plot for the results. The Charpy work transition ranged approximately from –25 to 100 °C. There was no statistically significant difference between the transverse and longitudinal specimens. Grouping the two together gives the following.

Average values of Charpy work:

at –25 °C	9.5 J (single data)
at 0 °C	16.6 ± 2.7 J (95% confidence)
at 25 °C	35.3 ± 4.9 J (95% confidence)
at 50 °C	64.3 ± 5.5 J (95% confidence)
at 75 °C	109.8 J (single data)
at 100 °C	141.0 J (single data)
at 145 °C	135.6 J (single data point on upper shelf)

Four kinds of crack surfaces for different temperatures are shown in Figure F3. The entire surface of the specimen fractured at 100 °C showed a ductile fracture appearance. Approximately 60% of the surface of 50 °C specimen was covered by brittle fracture appearance. More than 95% of the surface was covered by brittle fracture appearance for 0 °C. For –25 °C, the entire surface was a brittle fracture appearance. Comparison these results with Figure F2 shows that the crack surface appearance transition was approximately the same as the Charpy work transition.

5. Conclusion

The Charpy V-notch impact work transition ranged approximately from –25 to 100 °C. There was no statistically significant difference between the two orientations, i.e., transverse and longitudinal crack directions. The crack surface appearance transition was approximately the same as the Charpy work transition.

References

ABS   1984   Material for Hull Construction and Equipment, *Rules for Building and Classing Steel Vessels*, American Bureau of Shipping, Section **43**

ASTM E23-96   1997   Standard Test Methods for Notched Bar Impact Testing of Metallic Materials, *Annual Book of ASTM Standards*, **03.01** July
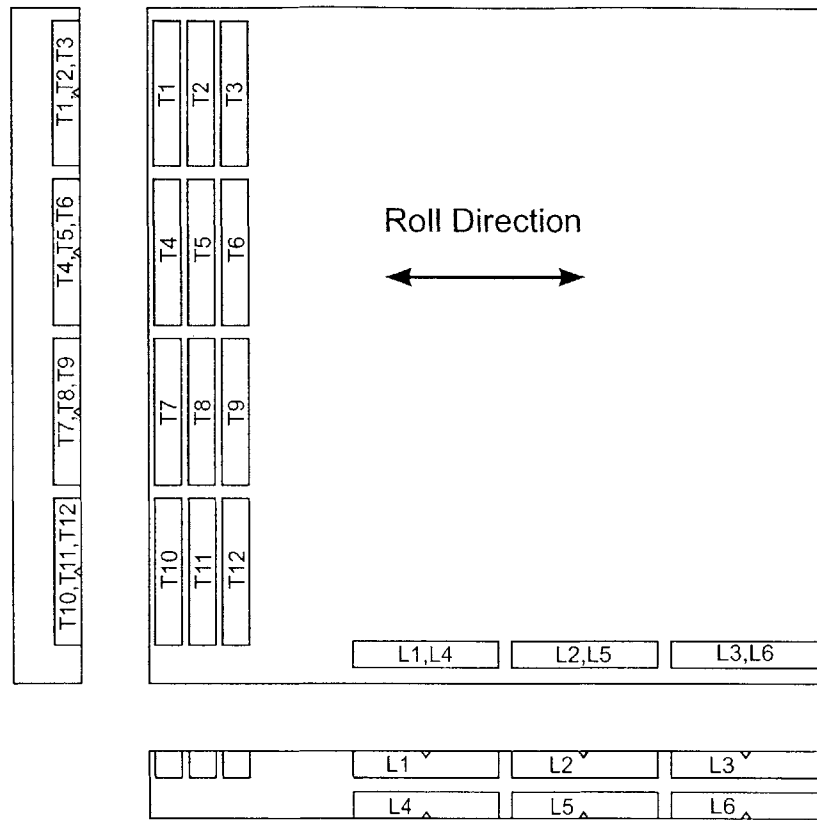
Figure F1   *Charpy V-notch specimen sampling map with the rolling direction (T: transverse, L: longitudinal)*

Table F1   *All results of Charpy V-notch impact tests for AH36*

Longitudinal Specimen#	Temperature (°C)	Work (J)	Transverse Specimen#	Temperature (°C)	Work (J)
T1	0	16.3	L1	25	43.4
T2	25	38.0	L2	50	59.7
T3	50	73.2	L3	0	14.9
T4	-25	9.5	L4	0	16.3
T5	75	109.8	L5	25	31.2
T6	100	141.0	L6	50	58.3
T7	145	135.6			
T8	50	62.4			
T9	50	67.8			
T10	25	33.9			
T11	25	29.8			
T12	0	19.0			
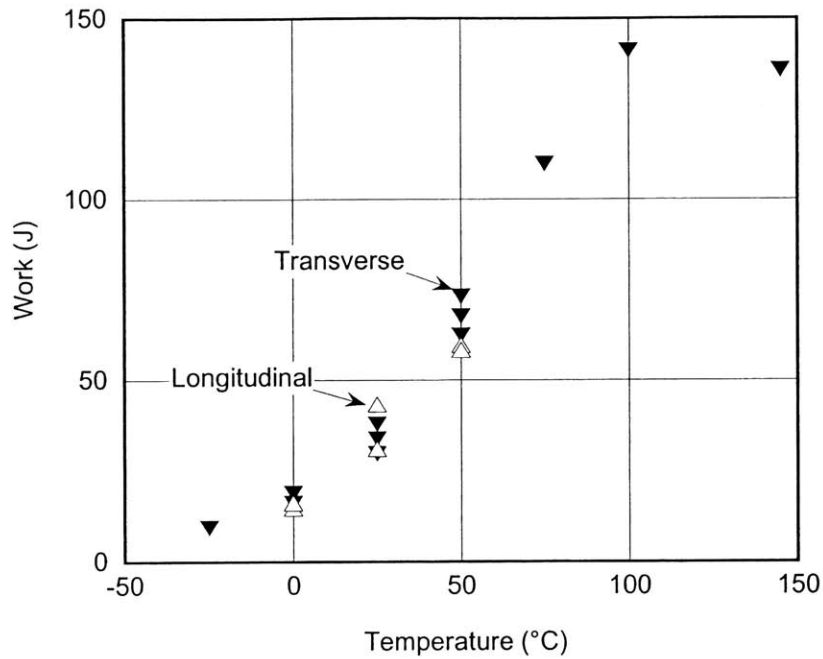
Figure F2   *Charpy V-notch impact work transition curve for AH36*
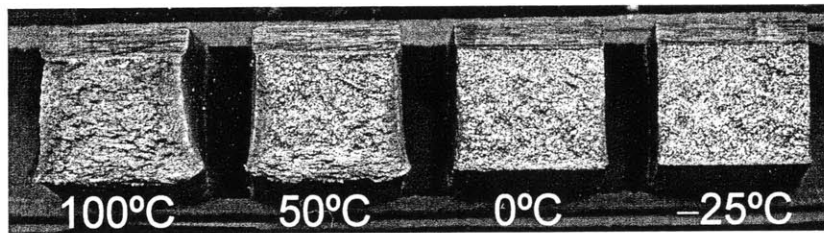
Figure F3   *Crack surfaces of Charpy V-notch specimen for different temperatures (from a digital scanner)*

Appendix G   Aging Effect on Hardness of Strain Hardened Steel

1.   Summary

Rockwell hardness and a modified low-strain superficial hardness were measured on tetragonal coupon specimens after compressing and aging. There was no significant aging effect on the hardness of strain hardened AH36 steel.

2.   Introduction

In order to find out whether the time between the first bending and the reverse bending has an effect, Rockwell hardness tests were carried out on compressed specimens after various aging times. The tetragonal specimens were machined out of the same plate from which the reverse bending specimens were cut. Aging effects are mostly observed on the upper yield point although the deformation in the Rockwell hardness test goes far beyond that. To observe the stress change close to the upper yield point, large ball Rockwell superficial hardness tests were also carried out.

3.   Method

The tetragonal coupon specimens (for dimensions, see the next section) were made from the same ABS AH36 steel plate as the reverse bending specimens. The coupon specimens were compressed in the direction transverse to rolling, which gives the same orientation as inside of the curved bending specimen. They were subjected to a compressive strain of $\varepsilon = -0.1$ or -0.5. Two kinds of hardness were measured at four times: before compression, right after compression, and after one day, one week and one month after compression.

One of the measurements was a standard Rockwell hardness B (H_{RB}) and the other was a modified large ball Rockwell superficial hardness (H_{MS}), both described below.

All procedures were carried out at room temperature.

3.1   Specimens

The tetragonal specimens were $10W \times 10D \times 20H$ mm as shown in Figure G1. One of the side faces was left as-rolled. After compression, the hardness was measured on the **L** (roll direction) and **S** (short transverse or plate) surfaces. Four coupon specimens were prepared according to the specification given in Table G1.

3.2   Material Hardness

From Paxton and Bear (1955), Figure G2(a) shows an yield phenomenon in a single crystal of iron containing 0.003 % carbon extended at 195 °K at a strain rate of 10^{-5}/sec. Figure G2(b) shows a yield phenomenon in a normalized specimen of 1020 steel strained at a rate of 10^{-5}/sec. Path A represents unloading and immediate reloading. Unloading with a 10-minute treatment at 100 °C has produced a new yield phenomenon (path B). Even a one-minute treatment at 100 °C brings back part of the yield phenomenon (path C).

Comparing path A (without aging) and B (with aging) in Figure G2 (b), shows that aging affects the upper yield point.

In Rockwell B, the maximum strain reaches up to $\varepsilon = 0.4$, which is far beyond the upper yield point, according to FEM analysis (see Appendix H).

To measure the hardness around upper yield point at the strain of $\varepsilon_0 = 0.01$, as in Figure E4 in Appendix E, the ball indenter is pushed against the material so lightly that the material around the contact barely reaches the yield strength. This condition can be realized by using a larger spherical indenter than the standard superficial Rockwell. The modified Rockwell superficial hardness test described in subsection (2) was carried out.

(1)   Rockwell B (H_{RB})

This hardness measure is ASTM Standard E18-94 (1994), and its definition and measuring method are shown schematically in Table G2 and Figure G3.

(2)   Modified Superficial Hardness (H_{MS})

To get a few times beyond the yield strain, the appropriate diameter of the indenter and the applied force are estimated below.

From Appendix E, the AH36 did not show a yielding point. Its 0.2 % yield strength was $Y =$ 322.2 MPa. For spherical indentation, the strain under the indentation can be approximately expressed in terms of the indenter diameter D and indentation diameter d (McClintock and Argon, 1999, p.458).

$$\varepsilon = 0.2(d/D) \tag{G1}$$

Experimental results by Tabor (1956) for non-strain-hardening materials obtained using a Vickers diamond indenter on fully cold-worked materials showed that the relation between the material hardness H and the flow strength Y is nearly $H = 3.2Y$ in the plastic range for a variety of materials of widely different hardness.

For non-strain-hardening materials, the presence of a built-up nose makes the conical solutions valid for spherical indenters if the friction is high enough or the penetration small enough. A ratio $H = 3.2Y$ is again expected, where Y is a uniaxial yield stress (McClintock and Argon, 1999, p456-457).

The indenter pushing load P is expressed in terms of the average normal stress q_0,

$$P = q_0 \frac{\pi d^2}{4} \tag{G2}$$

The average of normal stress right under the indenter will be approximately 3.2 times Y.

$$P = 3.2Y \frac{\pi d^2}{4} = 0.8\pi d^2 Y \tag{G3}$$

When strain hardening occurs, the flow stress increases. When the indenter pushes the material surface, the pressure under the indenter may go beyond the upper yield point.

To obtain very shallow indentation for a small strain, the largest available ball was chosen as an indenter, whose diameter is 1/2 inch ($D = 0.0127$ m), instead of the standard diameter of 1/16 inch (0.001588 m).

In order for the pressure to go beyond the yield strength and for the strain to reach a few times beyond the yield strain, $\varepsilon = 0.01$ was taken as the target strain. By Equation (G1),

$$\begin{aligned}
d &= \frac{\varepsilon D}{0.2} \\
&= \frac{0.01 \cdot 0.0127}{0.2} \\
&= 0.635 \times 10^{-3} \ (m)
\end{aligned} \tag{G4}$$

Thus, the pushing load is from Equation (G3)

$$P = 0.8 \cdot \pi \cdot \left(0.635 \times 10^{-3}\right)^2 \cdot 322.2 \times 10^6$$
$$= 326.5\,(N)$$
$$= 33.3\,(kgf) \tag{G5}$$

The closest existing choice of loading weights furnished in the superficial Rockwell testing machine is 30 kgf (294.2 N). Then, the radius of the surface of contact is using Equation (G3) again:

$$d = \sqrt{\frac{P}{0.8\pi Y}}$$
$$= \sqrt{\frac{294.2}{0.8\pi \times 322.2 \times 10^6}}$$
$$= 0.603 \times 10^{-3}\,(m) \tag{G6}$$

From the FEM analysis using bilinear strain-hardening steel, the diameter of the indent was obtained as 0.6 mm (see Appendix H). The estimate by non-hardening assumption shows a good approximation.

By the FEM analysis, the load-displacement curve was also obtained and shown in Figure G4 with an elastic solution given by (see Timoshenko and Goodier, 1970, p376)

$$a = 1.109\sqrt[3]{\frac{PR}{E}}, \quad q_0 = 0.388\sqrt[3]{\frac{PE^2}{R^2}} \tag{G7}$$

where R is the radius of the ball indenter and E is Young's modulus.

Accordingly, using these dimensions above, the measuring method is specified as shown schematically in Table G3 and Figure G5.

3.3 Procedure

(1) Compression

Specimens were compressed in the T-direction (Figure G1) using a universal testing machine (Figure G6). No lubricant was used between the specimens and liners, which were laid to prevent damage on the machine heads.

The compressive direction is the same as the direction of compression on the bending specimens. Two coupon specimens were compressed by 10 % and two by 50 % of their height, which gave nominally 10 % and 50 % strains on the T-direction. Because of no lubricant, the specimens bulged to the S- and L-directions as shown in Figure G7. Therefore, true strains on

the **S**- and **L**-surfaces are smaller than nominal values; however, the exact strain amounts are not so important for the purpose of measuring the aging effect.

(2) Hardness Measurement

The opposite side of measured surface of each specimen was machined flat. Hardness was measured five times and taken an average for each surface of the **S** and **L** surfaces and for each aging period.

1) Rockwell B

ASTM specifies that the distance between the centers of two adjacent indentations shall be at least three times the diameter of the indentation. However, the surfaces are curved due to bulging and the area for indenting measurement was limited. From the results of the numerical analysis (Appendix H), the distance between indentation centers of 1 mm was found to be long enough for the present purpose with the diameter of indentation 0.84 mm.

Accordingly, the center distance of 1.5 times indentation diameter, which is approximately 1.3 mm, was taken for any pair of two indentations. All indentations were located near the center of the bulging surfaces.

2) Modified Superficial Rockwell

Compared with Rockwell B, the strained region is smaller and, according to the previous analysis the indentation diameter is 0.6 mm. Therefore, the same distance of 1.3 mm was taken for any pair of two indentations. All indentations were located near the center of the bulging surfaces.

4. Results

The results of measurements of aging effect on strain hardening for Rockwell B and Modified Superficial Hardness are shown in Figure G8 and G9 respectively. In the figures, **L** represents the rolling direction and **S** represents the short transverse direction. All recorded data are gathered in Table G4.

In Figure G8, there seems to be no special tendency for change of hardness over various aging times although all H_{RB} measurements increased on compression.

In Figure G9, there seems to be no special difference in strain hardening due to compression or with subsequent time.

5. Conclusion

No significant room temperature aging effect was observed on hardness of strain hardened ABS AH36 steel material with nominal strain 0.1 and 0.5. Therefore, in reverse bending tests, the effect of the time span between the first bending and the reverse bending does not have to be considered for each bending specimen.

References

ASTM E18-94   1994   Standard Test Methods for Rockwell Hardness and Rockwell Superficial Hardness of Metallic Materials, *Annual Book of ASTM Standards*, **03.01** July

McCLINTOCK, F. A. AND ARGON, A. S.   1999   *Mechanical Behavior of Materials, Reprinted with corrections and errata*, Ceramic Book and Literature Service, Marietta, OH

PAXTON, H. W. AND BEAR, I. J.   1955   Further Observation on Yield in Single Crystals of Iron, *J. Metals Trans.* **7**, pp 989–994

TABOR, D.   1956   The Physical Meaning of Indentation and Scratch Hardness, *British J. Appl. Phys.* **7**, pp 159–166

TIMOSHENKO, S. P. AND GOODIER, J. N.   1970   *Theory of Elasticity, 3rd edition*, McGraw-Hill, New York
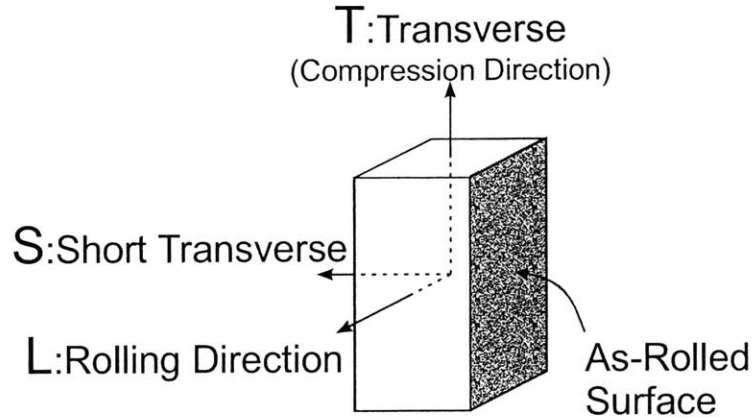
Figure G1   *Tetragonal coupon specimen*

Table G1   *Specimen and test cases*

Specimen #	1	2	3	4
Compressive Strain	0.1	0.5	0.1	0.5
Hardness	H_{MS}		H_{RB}	
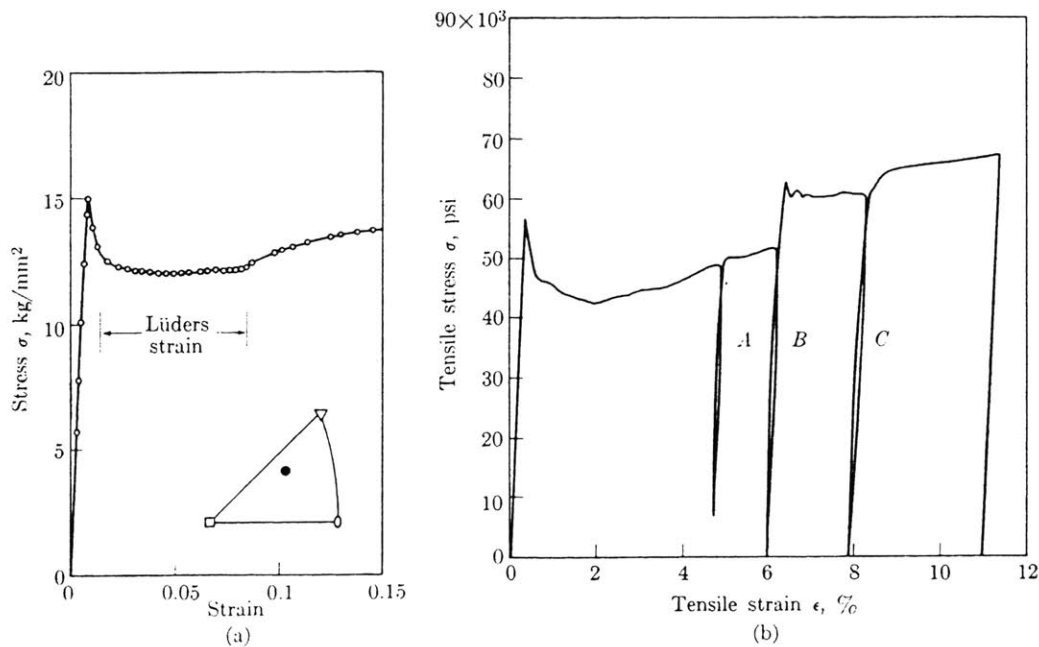
Figure G2   *Yield phenomena, (a) single crystal of iron containing 0.003 % carbon, (b) 1020 steel, 100 °C for 10 min on unloading at B; 1 min at C (McClintock & Argon (1999), p186)*

Table G2 Symbols and designations for Rockwell hardness B, Figure G3

Number	Symbol	Designation
1	D	Diameter of ball = 1/16 in. (1.588 mm)
3	P_0	Preliminary Test Force = 10 kgf (98 N)
4	P_1	Additional force = 90 kgf (883 N)
5	P	Total Test Force = $P_0 + P_1$ = 10 + 90 = 100 kgf (981 N)
6	-	Depth of penetration under preliminary test force before application of additional force
7	-	Increase in depth of penetration under additional force
8	e	Permanent increase in depth of penetration under preliminary test force, the increase being expressed in units of 0.002 mm
9	H_{RB}	Rockwell B hardness = 130 - e
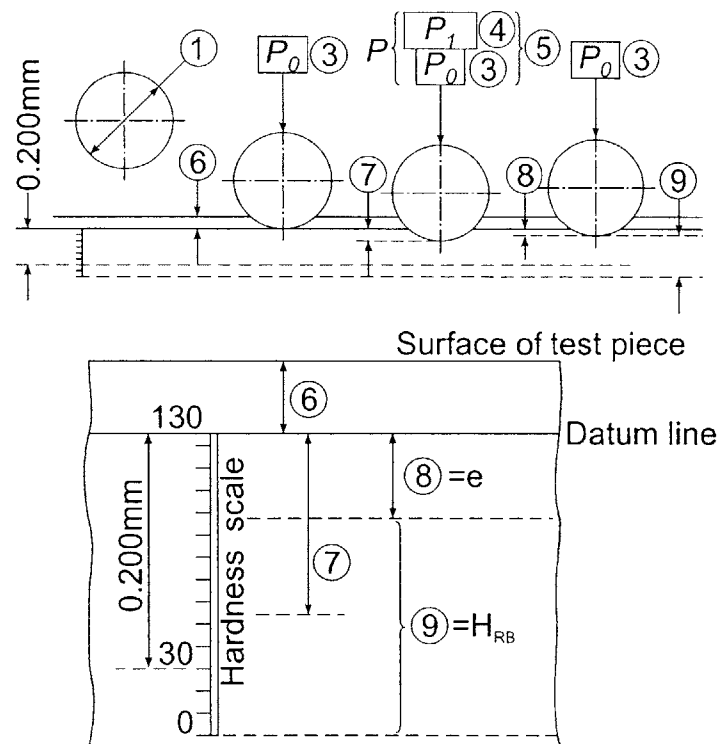
Figure G3 Physical and enlarged displacement in a Rockwell hardness B test (H_{RB}) (from ASTM, 1994)
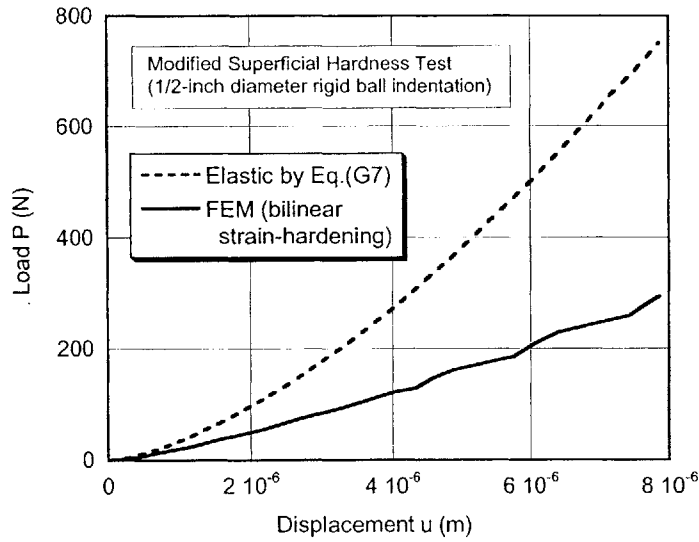
Figure G4   Loading curve of the modified superficial hardness test

Table G3   Symbols and designations for low-strain superficial hardness, Figure G5

Number	Symbol	Designation
1	D	Diameter of ball = 1/2 in. (12.7 mm)
3	P_0	Preliminary Test Force = 3 kgf (29 N)
4	P_1	Additional force = 27 kgf (265 N)
5	P	Total Test Force = $P_0 + P_1$ = 3 + 27 = 30 kgf (294 N)
6	-	Depth of penetration under preliminary test force before application of additional force
7	-	Increase in depth of penetration under additional force
8	e	Permanent increase in depth of penetration under preliminary test force, the increase being expressed in units of 0.001 mm
9	H_{MS}	Modified Superficial Hardness = 100 - e
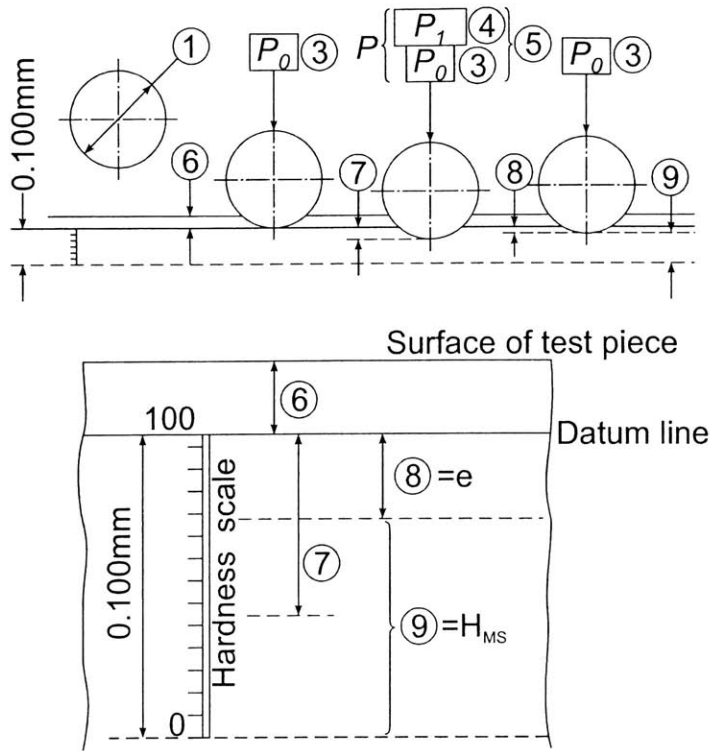
Figure G5   *Physical and enlarged displacement in a modified Rockwell hardness test (H_{MS})*
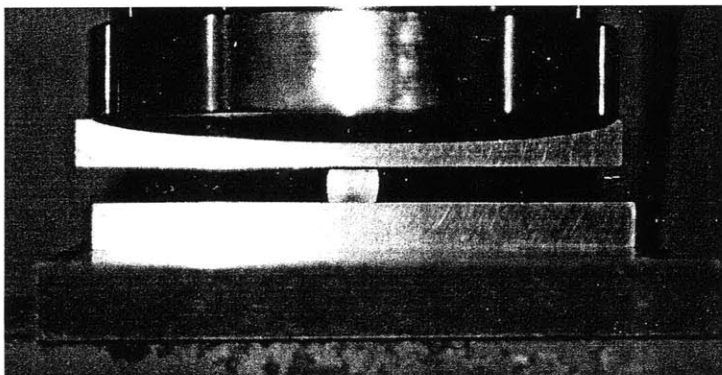
Figure G6   *Specimen Compression*
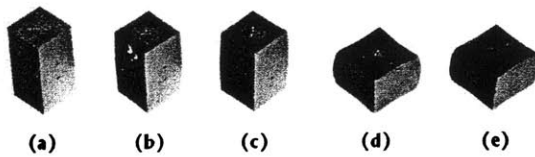
Figure G7   *Specimens (a: uncompressed, b&c: 10 % compressed, d&e: 50 % compressed)*
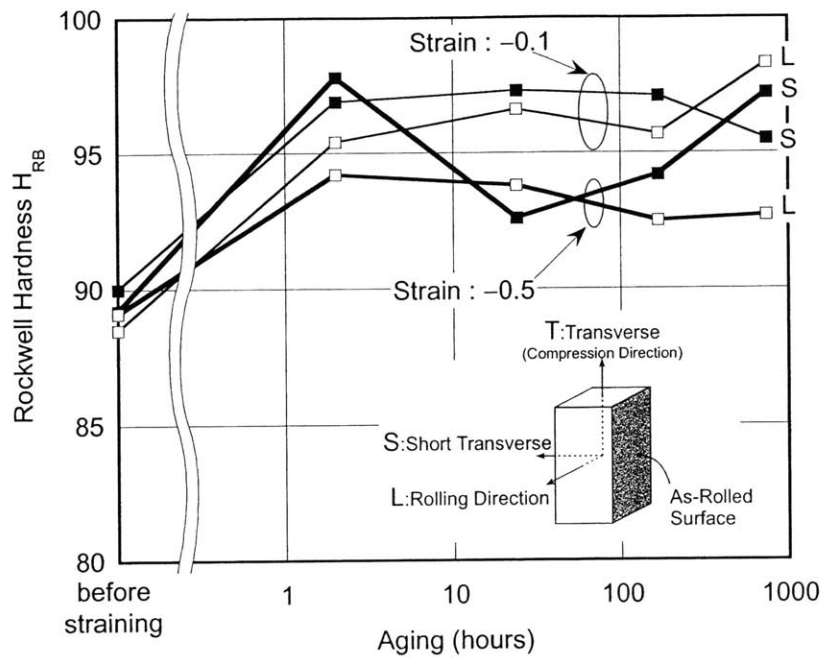
Figure G8   Aging of Rockwell B hardness H_{RB} of AH36 steel after straining by -0.1 and -0.5 in transverse direction
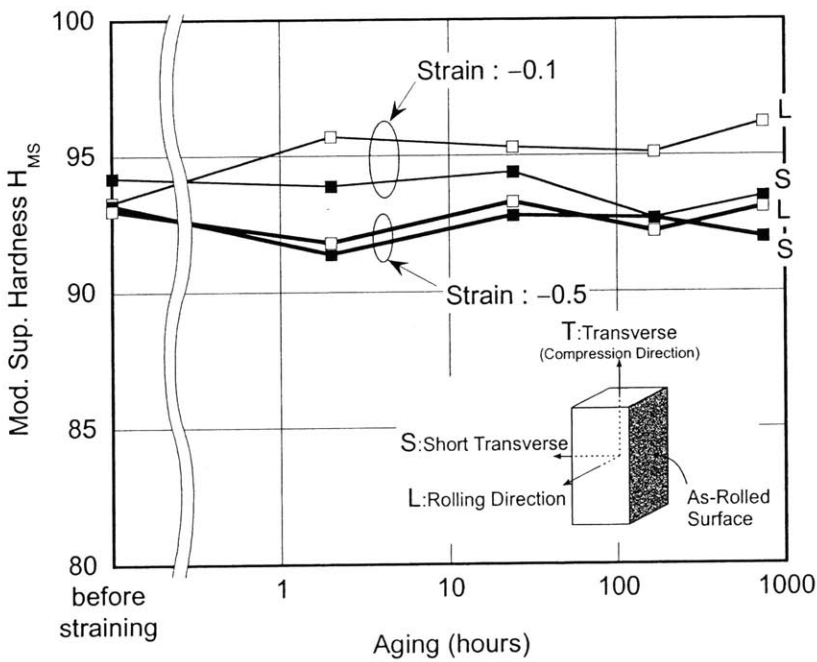
Figure G9   Aging of low-strain modified superficial hardness H_{MS} of AH36 steel after straining by -0.1 and -0.5 in transverse direction

Table G4   Measured data

Specimen #	1		2		3		4		
Plate	From the plate from which specimens #22 to 26 were cut out								
Nominal Strain	0.1		0.5		0.1		0.5		
Initial height(mm)	20.09	20.08	20.10	20.11	20.12	20.11	20.08	20.07	
Compressed height(mm)	18.07	18.07	10.33	10.33	17.49	17.50	10.02	10.03	
Edge length D&W(mm)	10.13	10.13	10.13	10.13	10.13	10.13	10.13	10.13	
Comp'd edge length(mm)	10.45	10.47	10.58	10.53	10.56	10.61	10.50	10.49	
Ctr swelling(mm)	10.78	10.80	15.24	15.21	11.01	11.02	15.54	15.42	
Dots distance(mm)	before	after	before	after	before	after	before	after	Strain was
Surface(1)	3.47	3.06	3.55	1.75	3.48	2.94	3.56	1.52	measured
Surface(2)	3.49	3.03	3.46	1.75	3.48	2.94	3.44	1.73	from two
Surface(3)	3.56	3.05	3.37	1.86	3.36	2.81	3.49	1.65	dots.
Measured Strain		0.131		0.483		0.158		0.532	
Superficial/Normal	Superficial B scale		Superficial B scale		Normal(2min) Rockwell B		Normal(2min) Rockwell B		
Ball size(in) & Load(kgf)	1/2 Ball	30kgf	1/2 Ball	30kgf	1/16 Ball	100kgf	1/16 Ball	100kgf	

| Aging(Hrs)	Surface*	S	L	S	L	S	L	S	L	Date
Before	Reading1	93.7	89.6	94.8	88.5	88.8	87.0	87.8	87.0	11/10/1999
	2	94.5	93.7	92.4	93.5	90.3	87.9	89.3	89.7	
	3	94.3	94.3	90.0	94.1	90.8	89.0	89.6	89.7	
	4	94.1	94.6	94.2	94.2	91.4	89.0	89.0	89.9	
	5	94.5	94.4	94.6	94.5	88.7	89.5	90.5	89.0	
	Ave.	**94.2**	**93.3**	**93.2**	**93.0**	**90.0**	**88.5**	**89.2**	**89.1**	
2	1	88.8	95.3	90.9	90.4	95.1	95.0	99.3	89.0	11/10/1999
	2	95.2	95.4	90.9	93.2	97.6	94.8	97.9	92.7	
	3	94.4	96.2	92.9	93.0	96.6	96.2	99.9	98.0	
	4	95.7	94.6	93.0	91.6	96.5	95.0	95.7	97.9	
	5	95.4	96.9	89.3	91.0	98.7	96.1	96.3	93.6	
	Ave.	**93.9**	**95.7**	**91.4**	**91.8**	**96.9**	**95.4**	**97.8**	**94.2**	
24 (1day)	1	91.3	95.0	94.9	92.8	96.5	93.9	95.2	95.7	11/11/1999
	2	95.0	94.0	93.7	93.0	96.4	96.1	92.2	94.1	
	3	94.8	95.5	91.5	92.5	97.1	97.4	89.3	94.1	
	4	94.5	96.2	91.0	93.2	99.4	98.2	93.0	94.0	
	5	96.3	96.0	93.1	95.2	97.3	97.5	93.5	91.3	
	Ave.	**94.4**	**95.3**	**92.8**	**93.3**	**97.3**	**96.6**	**92.6**	**93.8**	
168 (1wk)	1	86.0	94.2	96.5	92.3	94.0	94.5	99.7	95.4	11/17/1999
	2	94.2	94.8	93.7	91.6	98.1	95.7	98.4	92.7	
	3	94.7	95.5	90.0	94.3	97.1	98.0	86.7	93.8	
	4	94.1	96.1	90.2	92.8	97.3	97.0	93.5	93.1	
	5	94.4	95.1	93.2	90.1	99.0	93.2	92.9	87.3	
	Ave.	**92.7**	**95.1**	**92.7**	**92.2**	**97.1**	**95.7**	**94.2**	**92.5**	
744 (1mth)	1	90.5	96.3	89.6	90.2	91.0	96.8	96.4	90.4	12/11/1999
	2	94.6	96.0	93.8	93.4	93.0	98.7	97.5	93.5	
	3	93.4	96.9	94.6	95.1	96.3	99.6	100.0	93.4	
	4	96.4	95.9	91.1	93.2	98.9	98.0	95.9	92.3	
	5	92.7	95.9	91.1	93.8	98.5	98.4	96.1	93.7	
	Ave.	**93.5**	**96.2**	**92.0**	**93.1**	**95.5**	**98.3**	**97.2**	**92.7**	

* S : Behind of As-rolled Surface, L : Rolling Direction

Appendix H   Ball Indentation Analysis - ABAQUS

Summary

For the standard Rockwell B hardness and the modified large ball superficial hardness of steel ABS AH36, stress, strain, and displacement fields were calculated using FEM analysis code, ABAQUS. The results showed that the plastically strained region around the indentation was almost limited to within 1 mm from the center of indentation.

1.   Objective

In the standard Rockwell B hardness and the modified large ball superficial hardness test using tetragonal coupons of ABS AH36, the specimens bulged due to compression so that the distance between indentations specified in the ASTM standard cannot be taken on the test surface.

In order to find out the size of the plastically strained region around the indenter and to decide the minimum permissible distance between two indentations, an FEM analysis was carried out. For the Rockwell hardness B test and the modified superficial hardness test, 1/16- and 1/2- inch diameter rigid ball indenters are respectively pushed against the plane surface with normal force of 100 kgf and 30 kgf. The fields of stress, strain, and displacement were obtained for the steel material around indenter using an axisymmetric model.

2.   FEM Analysis Model

A static nonlinear analysis was carried out using the axisymmetric model shown in Figure H1. The DOF of outer side and bottom boundaries are all fixed. The stress-strain characteristic was approximated by bilinear strain hardening. The indenter was modeled by an analytical rigid spherical surface of ABAQUS definitions. No contact friction was applied.

The respective parameters were used as follows.

Indenter:
      Rigid bodies with 1/16-inch (1.59 mm) and 1/2-inch (12.7 mm) diameters

Material Properties:

Young's modulus	$E = 206 \times 10^9 \, Pa$
Poisson ratio	$v = 0.3$
Yield strength	$\sigma_Y = 381 \times 10^6 \, Pa$
Strain hardening	$d\sigma/d\varepsilon = 1.802 \times 10^9 \, Pa$ (Linear hardening)

Element type:

CAX4R (4-node bilinear axisymmetric quadrilateral element with reduced integration and hourglass control of the ABAQUS element library)

Number of elements: 1600

Load: 100 kgf (980.665 N) for the Rockwell hardness B

30 kgf (294.2 N) for the modified superficial hardness

Solver: ABAQUS Standard (implicit)

Total CPU time: 415.66 sec for the Rockwell hardness B

208.39 sec for the modified superficial hardness

3.   Results

The results for the Rockwell hardness B and the modified superficial hardness are respectively in (a) and (b) in each figure of Figures H2 to H5. It should be noted that since the magnitudes of the two results are much different, the shaded graphical regions cannot be compared simply each other.

For the Rockwell hardness B, Figure H2(a) shows that the diameter of indentation was 0.84 mm. Figure H3(a) shows von Mises stress, in which yielding is confined in the shaded region. In the outmost the region along the border of the model, the stress remains elastic. On the surface, yielding is within 1 mm from the indenter center. This is also observed in Figure H4(a), equivalent plastic strain distribution.

In Figure H4(a), the maximum equivalent strain $\varepsilon = 0.44$ occurred just under the indenter. The high strain region is confined under the contact area with the indenter. Outside the indentation, the equivalent strain is very small. At the point 1 mm from the center, the equivalent strain is only 0.004, which is only one hundredth of the maximum value.

A scalar of magnitude of deformation is shown in Figure H5(a). The magnitude of displacement at the point 1 mm from the center of indentation is approximately 0.001 mm while the maximum value of 0.1 mm occurs right under the indenter.

180

In the large ball superficial hardness tests, the indentation was very shallow and it is hard to tell the diameter of it. The contact region reached up to 0.3 mm in the radial direction from the center, i.e., a diameter of 0.6 mm, as shown in Figure H2(b). As shown in Figure H3(b) and H4(b), the equivalent stress and strain contours are distributed almost coaxially except for the region right under the contact area, where some kind of rigid cone was built up. It is found that the yielding field is forming almost a sphere with the 0.34 of radius. Furthermore, it is found that the plastically strained region is confined almost under the contact area. This result may suggest that the distance between the neighbor indentations could be taken much closer than that specified by ASTM (the center-to-center distance should be larger than three times the indentation diameter).

The maximum displacement was 0.0079 mm as shown in Figure H5(b).

Figure H6 shows the Load vs. Displacement curves for the both tests. Since the contact area is rapidly spreading with respect to displacement in the modified superficial, the slope of its loading curve is steeper than that of the Rockwell.

The model employed here should have been affected from the rigid boundary conditions to no small extent. For more precise results, the boundary should have been farther away. Extrapolated experiments are suggested to supplement the FEM calculation involving a three dimensional, residual strain problem, which would be very expensive, though.

4.   Conclusions

The diameters of indentations were 0.84 mm and 0.6 mm respectively for the Rockwell hardness B and the modified superficial hardness.

The high strain region is confined under the indentation for the both types of hardness. Judging by the yielding region alone, the neighbor indentation can be taken so that the distance between the two centers is more than 1 mm for the purpose of approximate measurement of the Rockwell B hardness. Further study should confirm this before deviating from ASTM recommendations.
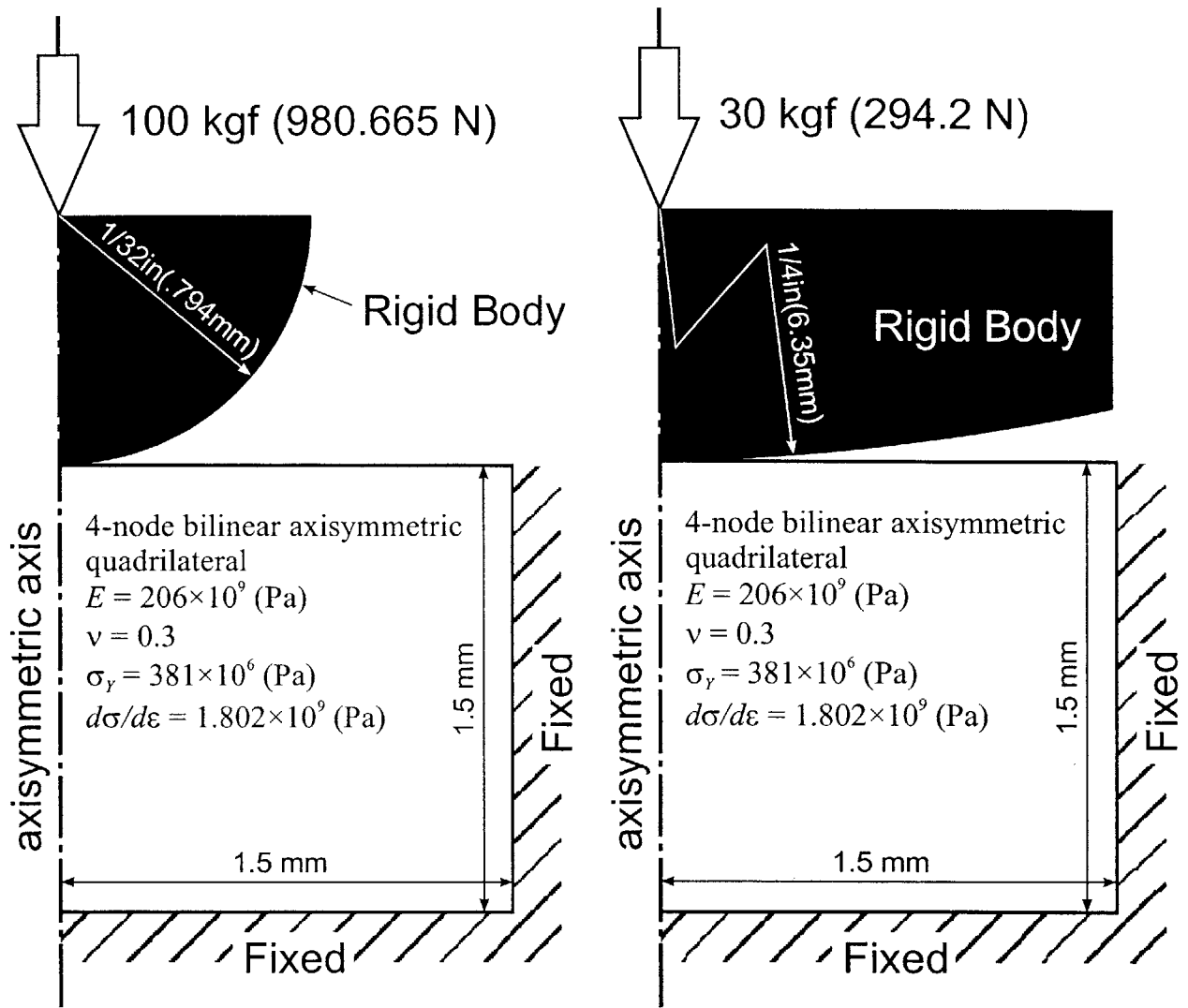
(a) Rockwell B hardness test

(b) Modified superficial hardness test

Figure H1 Axisymmetric analysis model
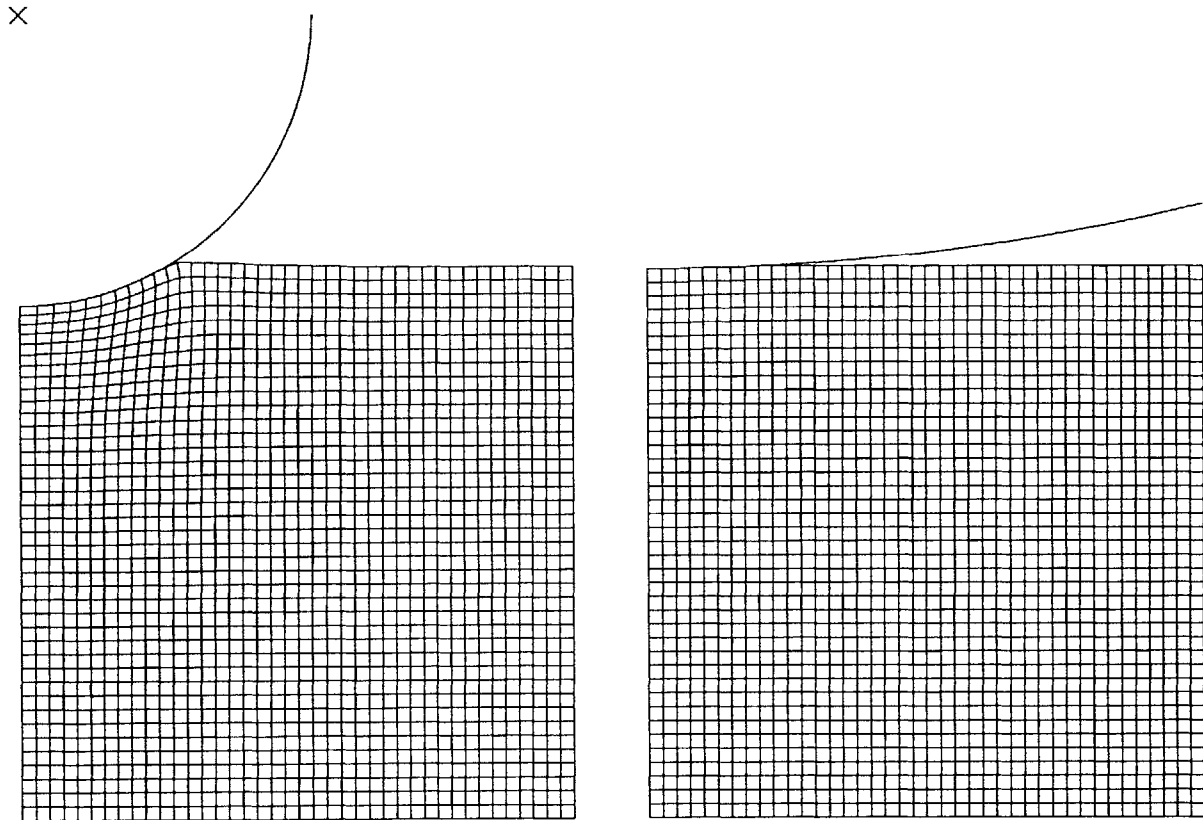
(a) Rockwell B hardness test   *(b) Modified superficial hardness test*

Figure H2   Deformed FEM mesh
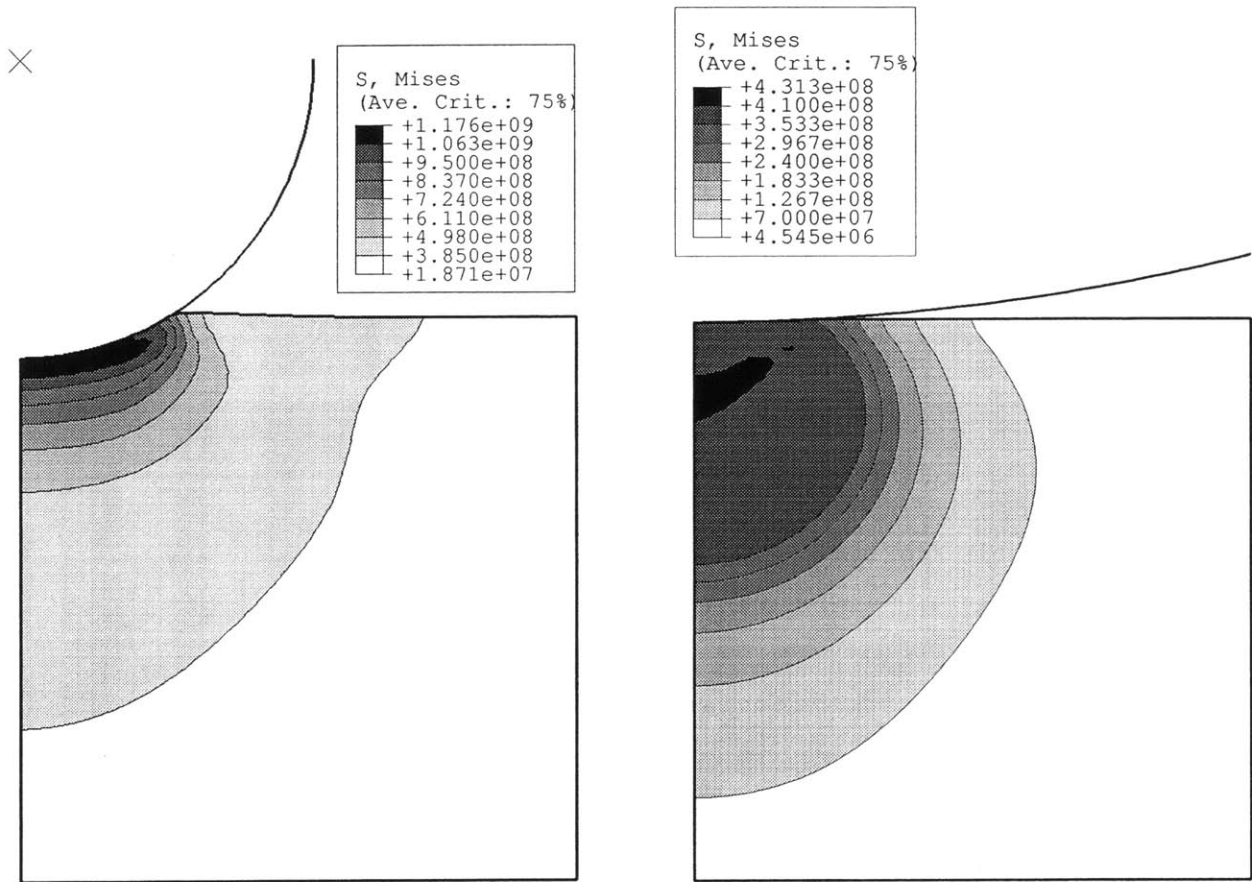
(a) Rockwell B hardness test

(b) Modified superficial hardness test

Figure H3   von Mises stress (unit:Pa)
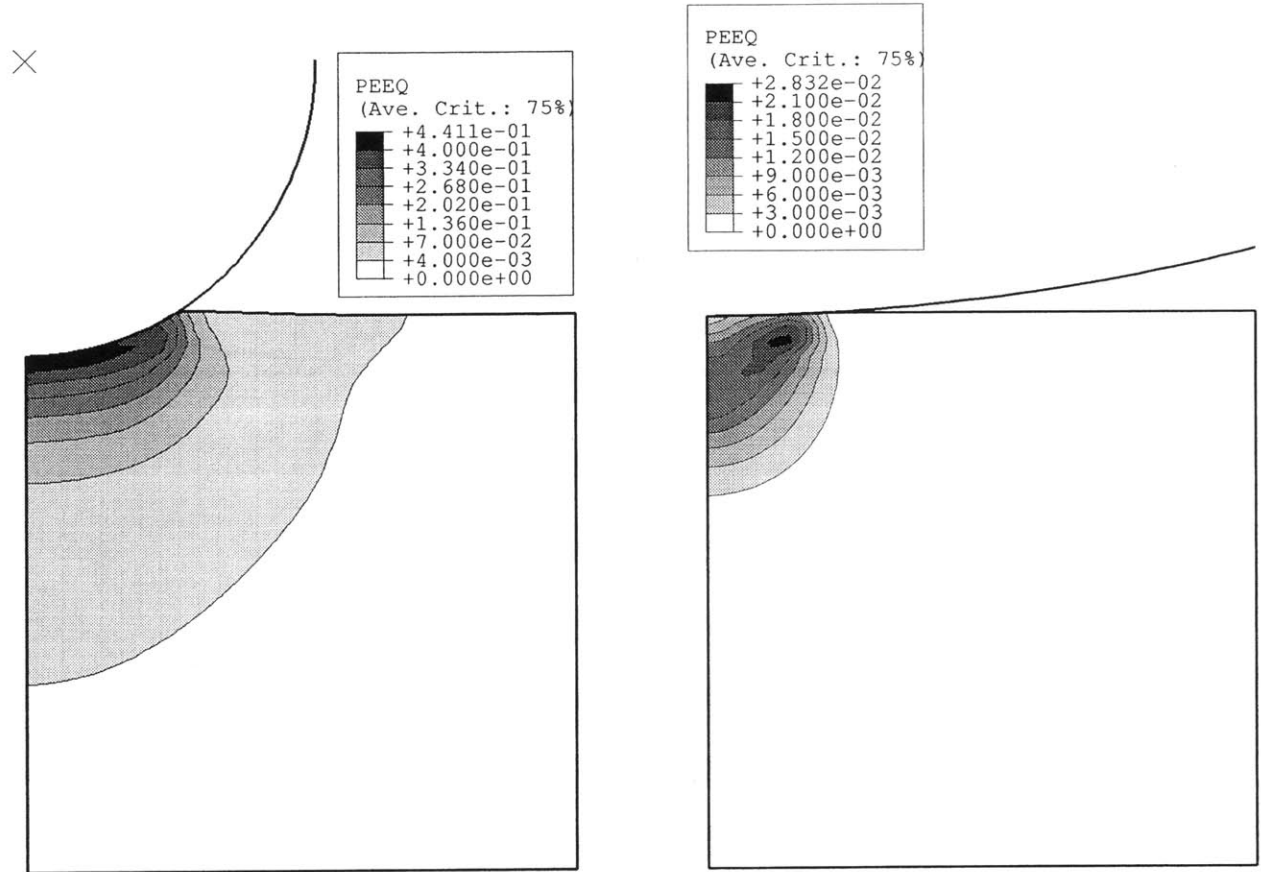
(a) Rockwell B hardness test

(b) Modified superficial hardness test

Figure H4   Equivalent plastic strain

U, Magnitude
+1.042e-04
+8.000e-05
+6.683e-05
+5.367e-05
+4.050e-05
+2.733e-05
+1.417e-05
+1.000e-06
+0.000e+00

U, Magnitude
+7.870e-06
+7.000e-06
+6.000e-06
+5.000e-06
+4.000e-06
+3.000e-06
+2.000e-06
+1.000e-06
+0.000e+00
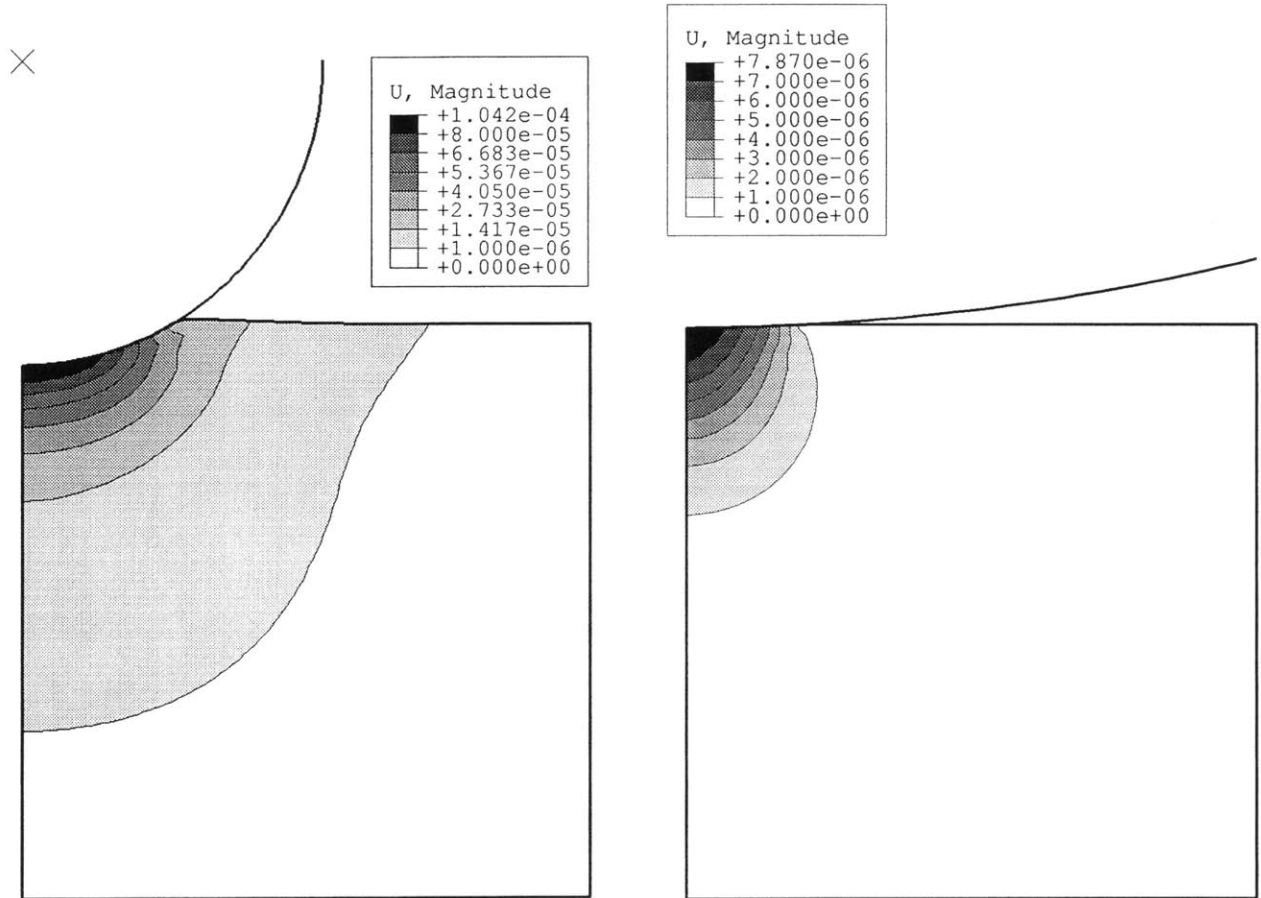
(a) Rockwell B hardness test   *(b) Modified superficial hardness test*

Figure H5   Scalar magnitude of displacement (unit:m)
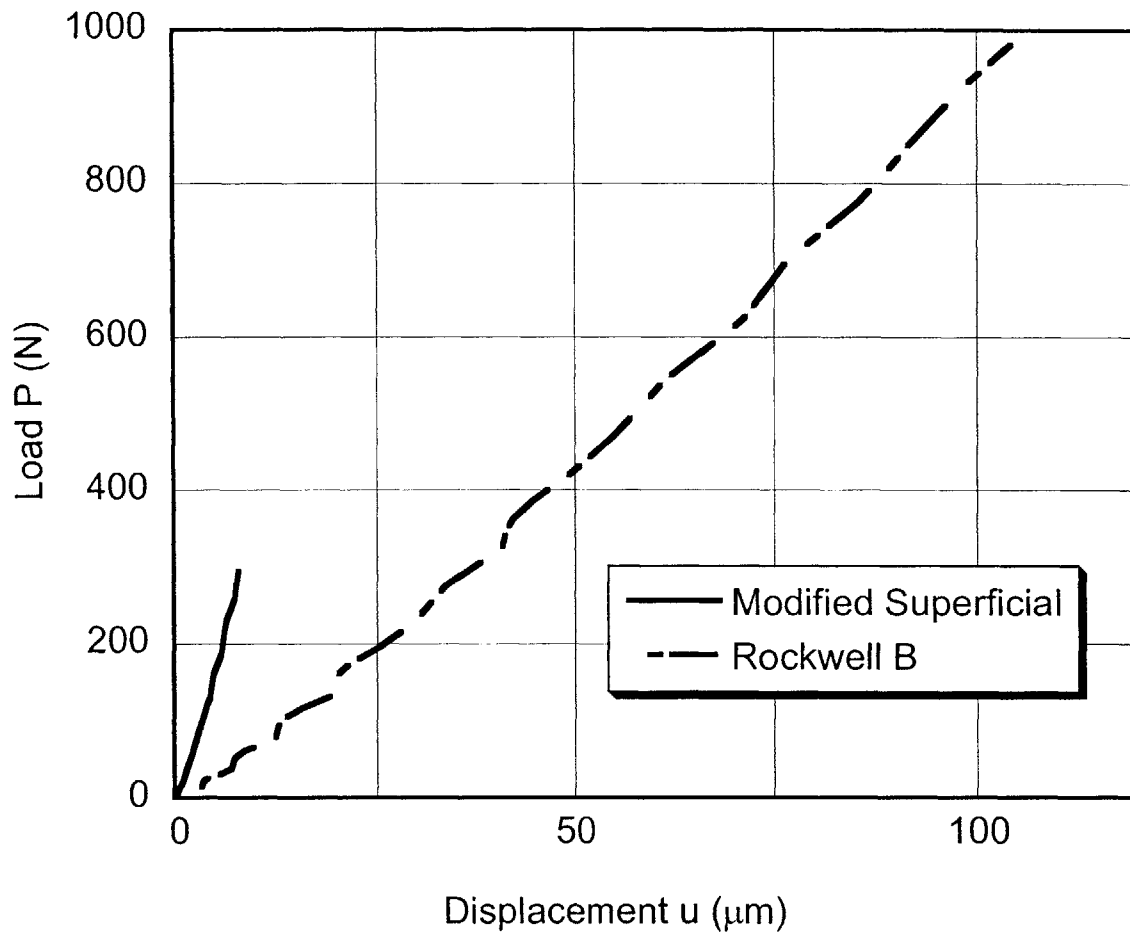
Figure H6   Load – total displacement curves for the two testing methods

Appendix I   Apparatus, Procedures, and Data of Reverse Bending Tests at Various Temperatures

1.   Introduction

When a steel plate made of ABS AH36 was reverse bent, cleavage fracture could be obtained. The details of apparatus, procedures, conditions, and results of the reverse bending test at low temperature are reported with all the data used and obtained.

2.   Specimen

Bending specimens were machined from high tensile steel AH36, 254 mm square, plates of 25.4 mm thickness in the transverse direction as shown in Figure I1. The dimensions of the specimens are shown in Figure I2. One side of the central part was thinned to 9.525 mm to localize the bending curvature. The other side was remained as-rolled or was machined, and it became inside in bending. The central part of the thinned side had curved corners to avoid cracks caused by strain concentration in the pre-bending (except for Specimens #7, #8 and #9, which had sharp corners). The central part with reduced thickness has a rectangular cross section with an aspect ratio of 4 so that on pre-bending its center is approximately in plane strain (McClintock and Argon 1965, pp. 349-353). Twenty-eight specimens had an as-rolled surface, and three specimens had a machined surface. On the outside of the center of each specimen, the gauge marks shown in Figure I3 were drawn with blue resinous paint.

The fronts and backs of three samples with as-rolled and machined surfaces are shown in Figure I4, and all specimens are shown in Figure I5. Properties and parameters of the high tensile steel AH36 are shown in Table I1.

3.   Apparatus

Three stages shown in Figure I6 consist of a) initiating bending the pre-bending in a 4-point fixture, b) completing the pre-bending at room temperature in an end-loading fixture, and c) reverse bending at a low temperature in the end-loading fixture. Details of specifications of each

configuration are described here.

3.1   4-Point Bending

3.1.1   Testing Machine
(1)   Hydraulic Load Frame

Name	:	Instron Load Frame Model No. 1331 (Figure I7)
Location	:	Room 1-034, MIT
		(property of Department of Civil and Environmental Engineering)
Performance	:	
Load Capacity		90 kN

(2)   Load Cell

Name	:	Instron Load Cell Model 2518-611
Performance	:	
Static Rating		±100 kN
Control	:	Instron 8500 Linear

3.12   Fixture

Support type	:	Four cylindrical supports
Support size		Four 25 mmϕ × 77.13 mmL rods
Upper Support Span		60 mm
Lower Support Span		170 mm
Lubricant		None

3.2   End-Loading at Room Temperature

3.2.1   Testing Machine
The same machine for the 4-point bending. See Section 2.1.1.

3.2.2   Fixture

Support type	:	Two pin-pin end-loading
Support size		See Figure I8
Pin Diameter		9.53 mm (3/8 inch)

3.3   End-Loading at Low Temperature

3.3.1 Testing Machine

(1) Screw Drive Load Frame

Name	:	Instron Load Frame Model No.5582 (Figure 19)
Location	:	Room 5-017, MIT
		(property of Department of Mechanical Engineering)

Performance :

Load Capacity	100 kN
Maximum Speed	500 mm/min
Minimum Speed	0.001 mm/min
Maximum Force at Full Speed	75 kN
Maximum Speed of Full Load	250 mm/min
Return Speed	600 mm/min
Position Control Resolution	0.060 mm
Crosshead Speed Accuracy (zero or constant load)	±0.10 mm or 0.15 % of displacement or ± one count on the display (whichever is greater)
Load Measurement Accuracy	±0.4 % of reading down to 1/10 of load cell capacity, ±0.5 % of reading down to 1/100 of load cell capacity. ±1.0 % of reading down to 1/250 of load cell capacity.

(2) Load Cell

Name	:	Instron Load Cell Model 2525-801

Performance :

Static Rating	±100 kN
Sensitivity	2 mv/v
Non-linearity	±0.05 of indicated load to 1/10 of capacity
Hysterisis	less than 0.05 % of full rated output
Creep	less than 0.05 % of full rated output
Temperature Effect on Zero	0.002 % of Full rated output per °F
Temperature Effect on Span	0.002 % of Full rated output per °F
Temperature Compensation Range	7 to 49 °C

Control Software:	Instron MERLIN

(3)   Temperature Chamber

Name   :   Instron 3119-007 Temperature Chamber (Figure I9)

Dimensions

External

Height A	710 mm
Width F	550 mm
Depth H	930 mm
Window-Height C	350 mm
Window-Width D	125 mm
Pullrod port diameter J	67 mm

Internal

Height B	560 mm
Width E	400 mm
Depth G	400 mm
Interior finish	The baffle, fan and rear of chamber have a matt black finish to optimize the performance of optical extensometers

Performance

Temperature range	Ambient to 350 °C
Heat up time, including 10 Kg mass	Better than 40 mins
Method of heating	Forced convection
Temperature stability	±2 °C
Temperature gradient	±1 % of setpoint, after 10 mins stability time, or ±2 °C, whichever is greater.
Temperature	Refer to Table I2

Accuracy

Temperature overshoot setpoint	2 °C maximum

Optional accessories

Carbon Dioxide CO_2	Ambient to –70 °C
Nitrogen N	Ambient to –150 °C

3.3.2 Fixture

The same fixture for the end-loading at room temperature. See Section 3.2.2.

4.   Procedure

The bending specimen was bent first to $\beta = 40$ degrees ($\theta = 140$) by the 4-point bending configuration in Figure I6a. The machine head traveled at a speed of 10 mm per minute, which corresponded to an average strain rate of $d\varepsilon/dt = -0.001$. After that, the specimen was bent in the end-load configuration in Figure I6b up to the planned angle, which gives the planned compressive strain at the inside of the bent specimen by the converting Equation (C23) in Appendix C. For example, a bend angle $\beta = 130$ degrees ($\theta = 50$ degrees) corresponds to the compressive strain $\varepsilon_{pre} = -0.43$ with the assumption of Appendix C. The machine head traveled at a speed of 10 mm per minute, which corresponded to an average strain rate of $d\varepsilon/dt = -0.0006$. After the pre-bending, the size of the deformed strain gauge mark was measured to calculate the pre-strain on the outside surface. The inside radius of curvature and plate thickness were also measured to calculate the nominal pre-strain on both inside and outside surface. A set of drill bits were used to measure the curvature.

The reverse bending in Figure I6c was carried out one day after the pre-bending. An initial tension was applied to the two pins and kept at or below 0.7 kN to hold the specimens stable. The specimens were cooled down in the temperature control chamber using liquid nitrogen. Since the cooling time is long, carbon dioxide was not used. After the atmosphere inside the chamber reached to the set temperature, the temperature was held for 60 minutes before the reverse bending. As the specimen and attachments were cooled down, the load cell detected a rise of tension force by shrinking and the initial tension of 0.7 kN was kept manually.

The 60 minute saturating time was chosen for the following reason. The atmospheric temperature was measured in the chamber by a thermocouple. The load cell detected the increase of tension force due to shrinking of the specimen and its attachment as time went. It is considered that the shrinking continues as long as the temperature distribution inside the specimens is changing. In 60 minutes, the increase of tension force became undetectable. Then the distribution of temperature was considered constant and flat across the cross section of the specimen. According to the temperature equilibration analysis described in Appendix J, the 12 minutes was long enough for the saturation to within 10^{-5} of the initial temperature difference.

After the saturation of the inside temperature distribution, the specimen was extended at 10 mm/min, which corresponded to an average strain rate of $d\varepsilon/dt = 0.0009$ or less. The load and extension were recorded. The extension was continued until the specimen cleaved or the load reached 22 kN as an upper limit by the jig due to the tensile effect in that a mean stress reached

10 % of the tensile strength. Cleavage fracture was detected as a large noise and drop of load. Ductile crack growth was detected by visual observation usually after large deformation. The reversed strain was calculated from the extension of the pin distance by Equation (C35) in Appendix C.

5. Test Conditions

The ranges of variables affecting the cleavage conditions on reversed bending are shown here.

(1) Strains

Pre-Strain $\qquad$ $\varepsilon_{pre} = -0.20, -0.30, -0.35, -0.43$

Reversed Strain $\qquad$ $\varepsilon_{rev} < 0.4$, limited by abrupt load increase (to about 22 kN) on pin separation

(2) Temperatures

Temperature on Pre-Bending $\qquad$ T_{pre} = ambient

Temperature on Reverse Bending $\qquad$ $T_{rev} = -20, -25, -30, -40\ °C$

(3) Others

Surface $\qquad$ As-rolled or machined

Aging $\qquad$ One day between pre-bending and reverse bending

Strain Rate $\qquad$ $d\varepsilon/dt = -0.001$ for 4-point pre-bending

$\qquad$ $d\varepsilon/dt = -0.0006$ for end-loading for pre-bending

$\qquad$ $d\varepsilon/dt = 0.0009$ for end-loading for reverse bending

6. Results

The setups of the 4-point bending before and after bending are shown in Figure 110. After the pre-bending, the sizes of the strain gauge marks on the outside were measured, as well as the plate thicknesses of the central parts of the specimens. Examples of deformed strain marks are shown in Figure 111.

Pre-strains on the outside by mark and on both the inside and outside by curvature were calculated and plotted on Figure 112 to compare with the theory (Appendix C) and FEM (Appendix B) results. At the gauge mark, the transverse strain was about 11 % of the longitudinal strain,

so the condition was nearly plane strain. Specifically, at the bend angle of 130°, the transverse strains were -0.05 ± 0.10 (20 to 1 odds) compared to the longitudinal strains of 0.43 ± 0.05 (20 to 1) for the points in Figure I12. This confirmed the aspect ratio of the net cross section chosen in Section 2 for plane strain.

The plate thickness measured from specimens with a machined surface increased about 1.5 percent for the largest pre-bending of 130°. This justifies the assumption of a constant thickness of bent plate derived in Appendix C for non-hardening material. For the pre-strain calculation, the thickness after pre-bending was used.

Because of the limited number of specimens, first the pre-strain and then the reverse bending temperature was varied while the other was taken to be constant. The nominal pre-strains of -0.2, -0.3, -0.35 and -0.43 were chosen for a constant reverse bending temperature of -40 °C. The temperatures on reverse bending of -20, -25, -30 and -40 °C were used for a constant pre-strain of approximately -0.43. Precise results are shown in Table I3, and the results sorted by pre-strain and temperature during reversal are shown in Table I4.

(1) For Constant Pre-strain of -0.43

For the constant pre-strain of -0.43, the reversed strains to fracture ε_{revf} were plotted in Figure I13 as black circles versus the temperature on reversed bending. For -40 °C, cleavage fractures occurred with reversed strains $\varepsilon_{revf} = 0.113$ or less, and as low as $\varepsilon_{revf} = 0.014$. Below -30 °C, cleavage fractures occurred with reversed strains $\varepsilon_{revf} = 0.209$ or less, and as low as $\varepsilon_{revf} = 0.011$. For -20 °C, it was $\varepsilon_{revf} = 0.25$ or more. When a specimen was reverse bent at room temperature, it did not cleave with $\varepsilon_{rev} = 0.265$, which is also plotted on Figure I13. Although the data shows some scatter, there is a strong tendency for higher reversed strain to fracture at higher temperature.

The results for the specimens with a machined surface were also plotted in the Figure I13 as black triangles. The temperature dependency was weak, and the reversed strain to fracture ε_{revf} was almost constant at $\varepsilon_{revf} = 0.34$ over the temperature of -40 to -20 °C, while that for the as-rolled surface depended strongly on the temperature.

(2) For Constant Temperature of -40 °C

For the constant reverse bending temperature of -40 °C, the reversed strains to fracture ε_{revf} were plotted in Figure I14 versus the pre-strains as black circles. White circles in the figure show that no cleavage fracture occurred, but ductile cracks initiated. While the largest reverse strain to fracture with $\varepsilon_{pre} = -0.43$ was $\varepsilon_{revf} = 0.113$, that with $\varepsilon_{pre} = -0.35$ was 0.254. With $\varepsilon_{pre} = -0.3$ or smaller, no specimen cleaved.

When specimens bent to small angles were reverse bent by end-loading, tensile loading

soon became predominant rather than bending moment at the region of interest. Therefore, for the specimens with $\varepsilon_{pre} = -0.2$, a reversed strain of only $\varepsilon_{rev} = 0.087$ was subjected before the tensile load exceeded 22 kN, while other cleavage occurred at 16 kN or less.

(3)   Other Observations

The as-rolled surface was initially covered with a smooth oxidized scale. When the specimens were pre-bent, the scale came off and a black rough surface appeared on the inside of the bent portion. Machined surfaces on the outside became dim and rough on bending. On the machined surface inside the bent specimen, tiny wrinkles grew and the surface became rough.

When the cleavage fracture occurred with as small as $\varepsilon_{revf} = 0.06$ or less, there was no crack visible on the inside of the bent specimen. For the fracture with a reversed strain more than $\varepsilon_{revf} = 0.06$, some ductile sliding off were observed prior to cleavage. When the specimens with machined surfaces fractured, similar ductile sliding off initiated from the about 0.1 mm wide wrinkles before fractures.

Figure 115 shows the load-displacement curves with specimen numbers for reverse bending in the end-loading configuration. In Figure 115b and 115c for the specimens with an as-rolled surface and $\varepsilon_{pre} = -0.43$, all the curves almost were superposed with different fracture points. The upward curvature of the curves in the later half was caused by the geometric effect of bent specimen. The tensile load for the specimen with a machined surface was 4% larger than that with an as-rolled surface. This was caused because the net thickness of the specimen excluding the oxidized scale was approximately 0.2 mm less than the initial total thickness of 9.525 mm, while the specimen with a machined surface had a net thickness of 9.525 mm.

Figure 116a shows a crack surface which was subjected to $\varepsilon_{pre} = -0.43$ and cleaved at $T_{rev} = -40$ °C giving $\varepsilon_{revf} = 0.019$. Both ends of the crack surface were curled up by the 3-D effect of plate bending, but the central part remained almost flat. The cleavage crack spread over the entire cross section with only a slight ligament on the outside of the bend. There was no initial ductile crack observed at the initiation point on the inside. On another sample of a crack surface in Figure 116b of a specimen that was subjected to $\varepsilon_{pre} = -0.43$ and fractured at $T_{rev} = -20$ °C giving $\varepsilon_{revf} = 0.265$, there were initial micro-ductile wedge openings about 0.2 mm deep on the inside surface prior to cleavage fracture, but no micro-ductile ligament on the crack surface. The cleavage in Figure 116b occurred at a higher tensile load. The higher potential load accomplished the complete fracture without ligament.

Specimen #9 was a preliminary specimen, and it had sharp corners other than round corners. It was pre-strained by −0.36, and reverse bent at room temperature. It did not cleave with reverse strain of $\varepsilon_{rev} = 0.302$ but about 1 mm-deep ductile cracks was initiated and grew. After that, it was rebent up to the same angle as the first pre-bending and reverse bent again. At the second

reverse strain of $\varepsilon_{rev2} = 0.245$, it cleaved. Two cycles of very large straining caused cleavage fracture even at room temperature.

Reference

McCLINTOCK, F. A. AND ARGON, A. S. 1999 *Mechanical Behavior of Materials, Reprinted with corrections and errata*, Ceramic Book and Literature Service, Marietta, OH, p350
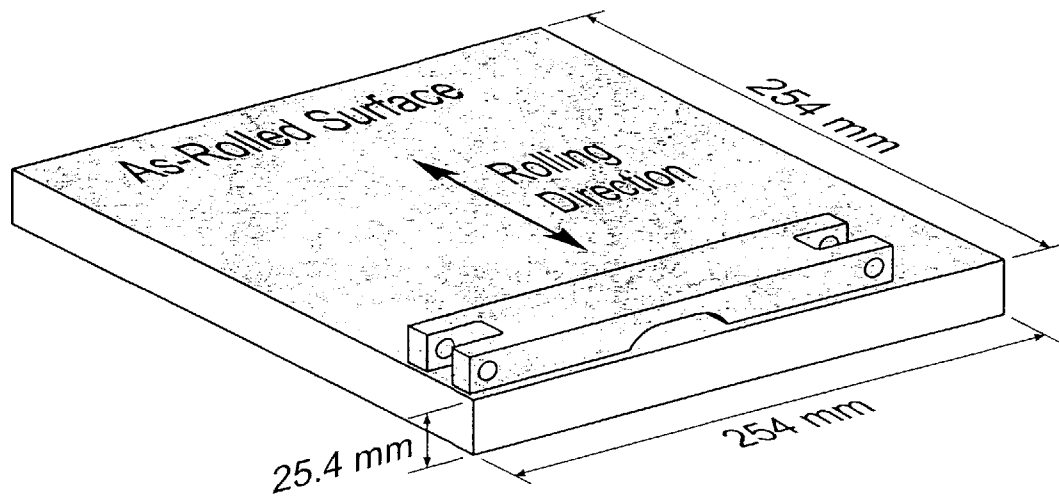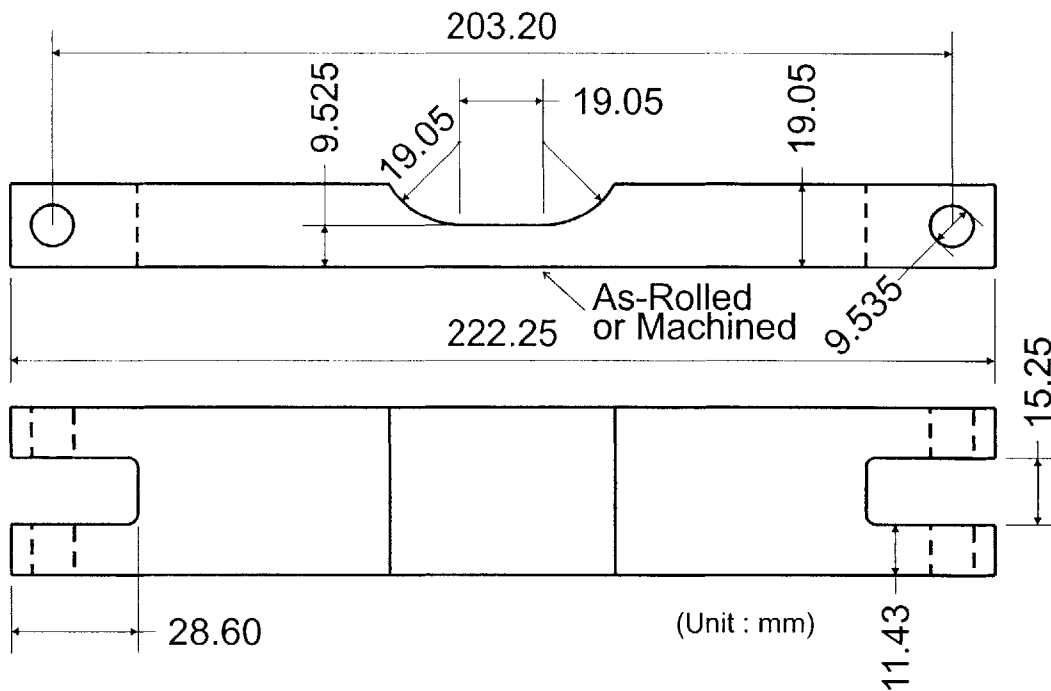
Figure I1   Specimen sampling from AH36 steel plate
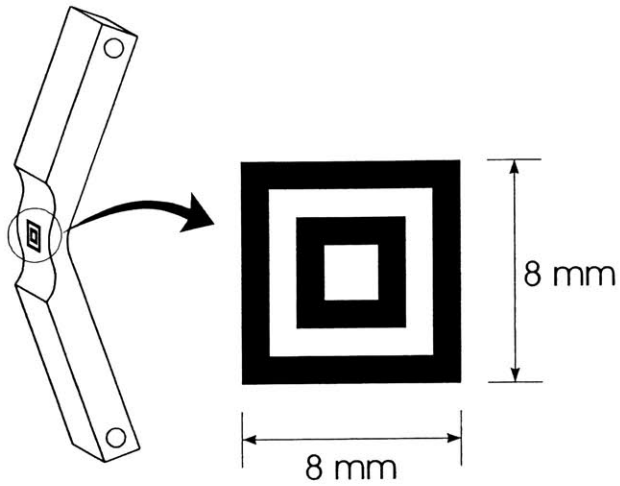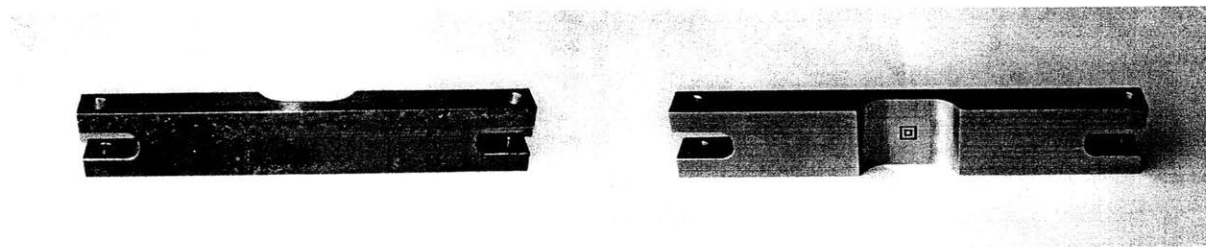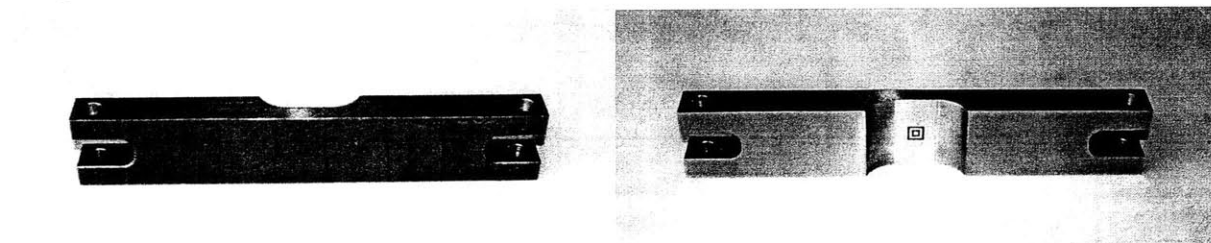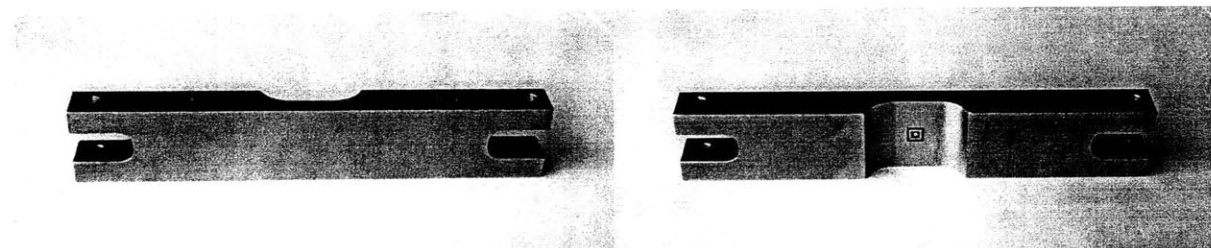

Figure I2   Bending specimen

Figure I3   Strain gauge mark

a. Specimen #12 with as-rolled surface

b. Specimen #13 with as-rolled surface

c. Specimen #14 with machined surface

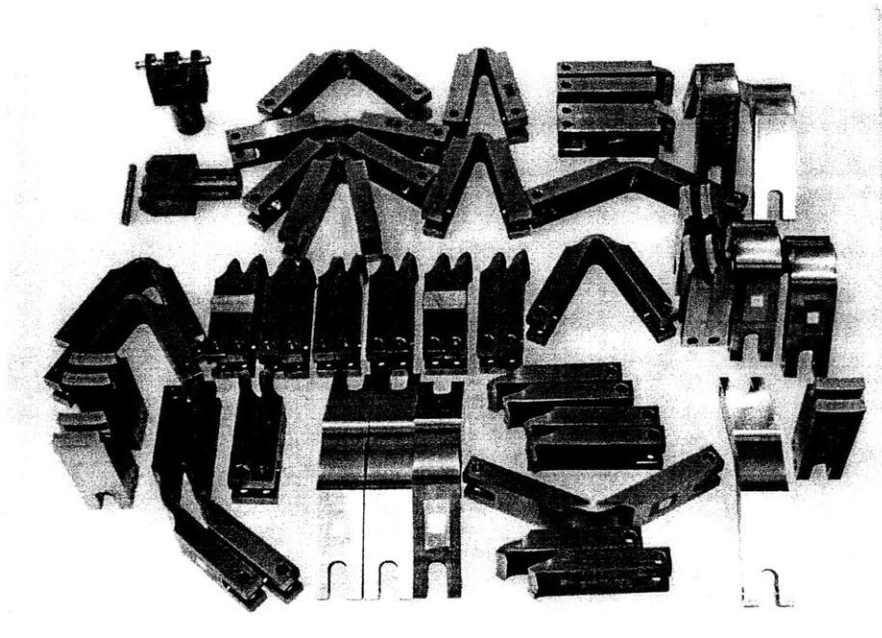*Figure I4   Three samples of reverse bending specimens*

Figure I5   All specimens

Table I1   Properties and parameters of high strength steel AH36

Supplier's Data									
Chemical composition, %									
C	Mn	Si	P	S	Cr	Ni	Al	Cu	
0.179	1.56	0.441	0.016	0.006	0.03	0.18	0.053	0.153	
Ti	N	Nb	V	Mo	Ca	Sn	B		
0.003	0.007	0.003	0.005	0.054	0.0002	0.002	0.0002		

Mechanical Parameters in L-direction (rolling direction)									
Yield Point MPa	Tensile Strength MPa								
380.6	590.9								

Measured Mechanical Parameters in T-direction (long transverse direction)								
Yield Point MPa	Tensile Strength MPa	Elong. 2.5 in %	Charpy V-notch(TS) J			ASTM Grain Size No.*1	Plate Thickness mm	
			-25 ºC	0 ºC	25 ºC			
322.2	621.1	19.7	9.5	16.6	35.3	5.7	25.4	

*1 The ASTM grain size number, G, is defined as $N_{AE} = 2^{G-1}$, where N_{AE} is the number of grains per square inch at 100X magnification.
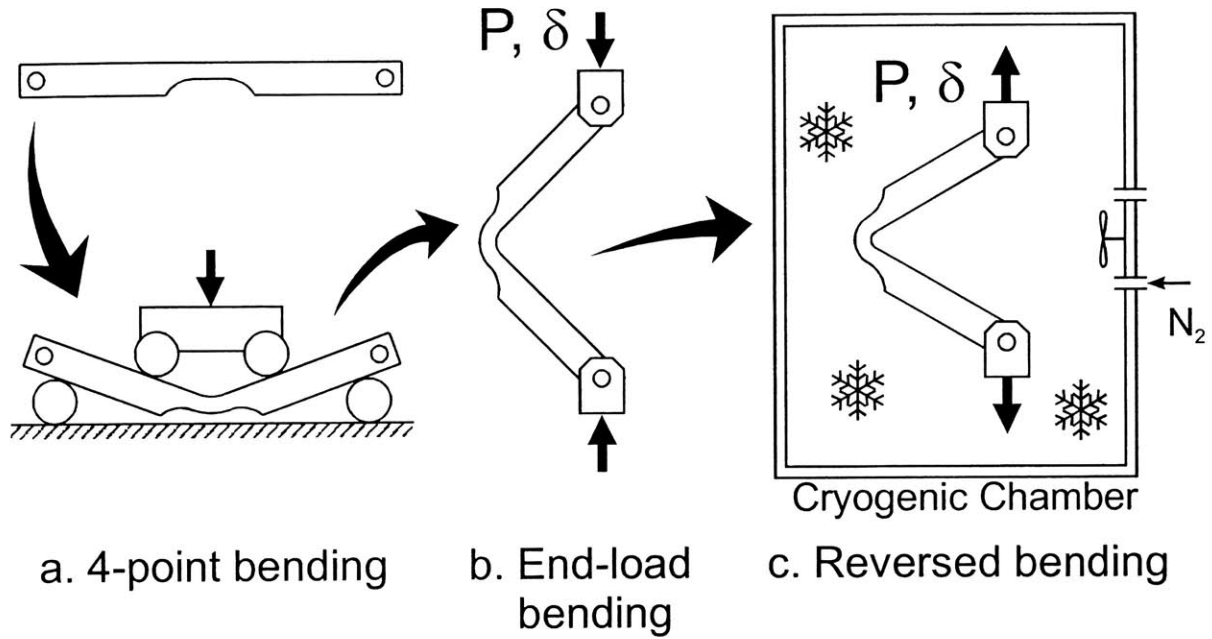
a. 4-point bending   b. End-load   c. Reversed bending
bending

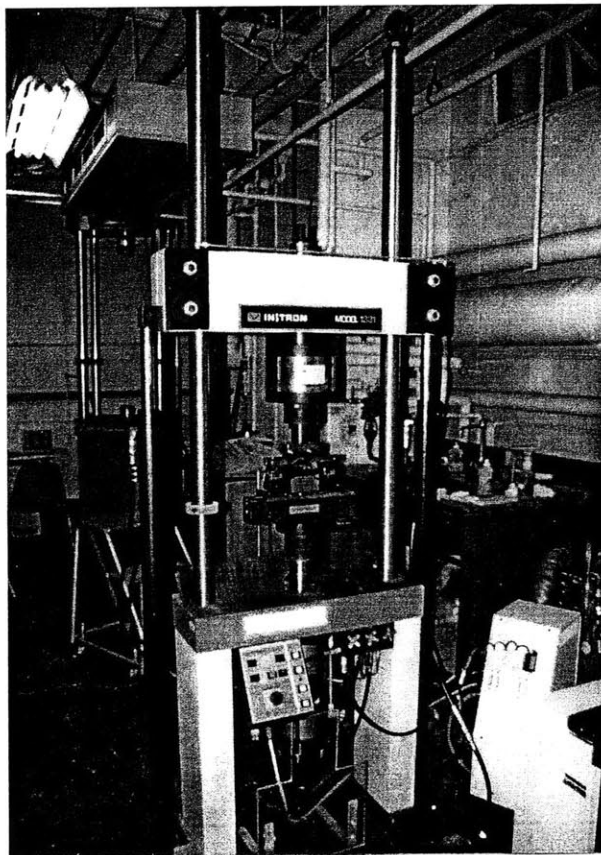*Figure I6   Reverse bending test procedure*

Figure I8   Attachment fixture

*Figure I7   Hydraulic load frame for 4-point bending
configuration*
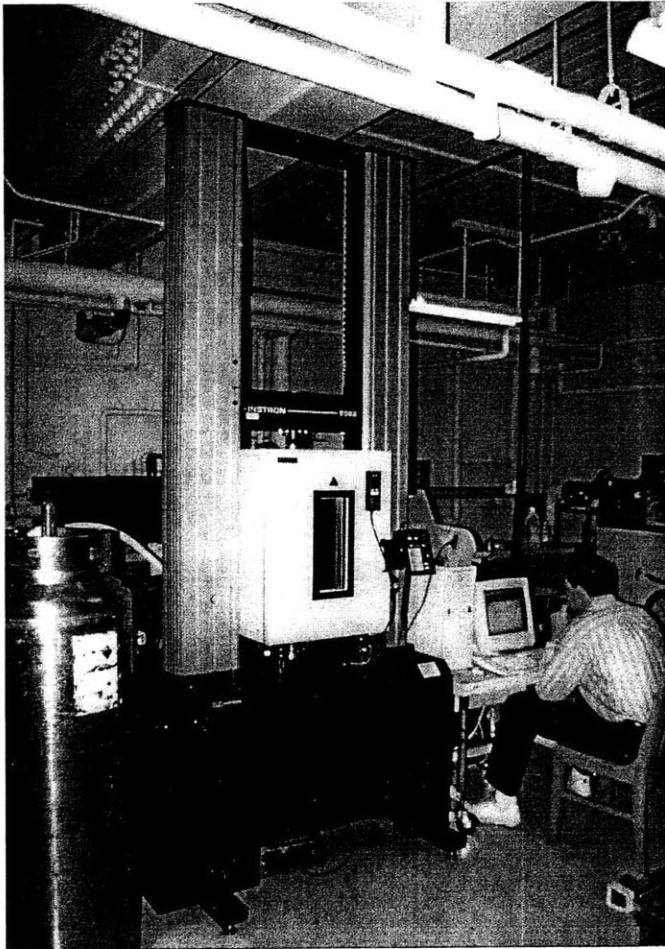
Table I2   Temperature chamber accuracy

Temperature (°C)	Accuracy (°C)
-150	±5.5
-100	±5.0
-40	±3.5
0	±3.5
100	±3.5
200	±3.5
300	±3.5
400	±4.0
500	±5.0
600	±5.5

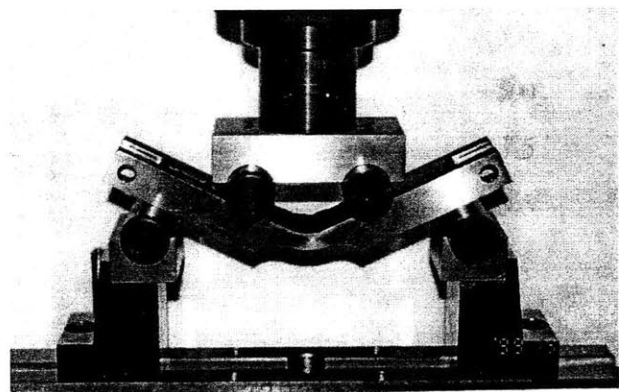*Figure I9   Screw drive load frame with temperature chamber*
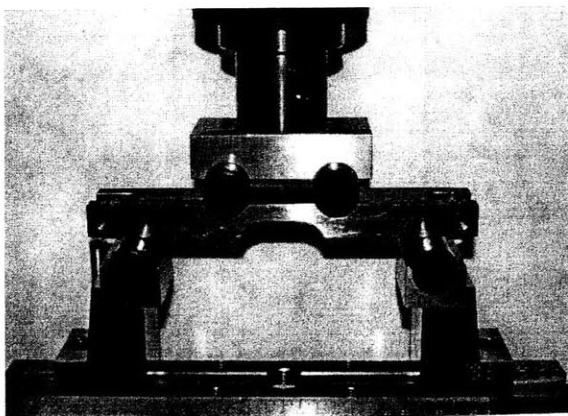

Figure I10   4-point bending configuration
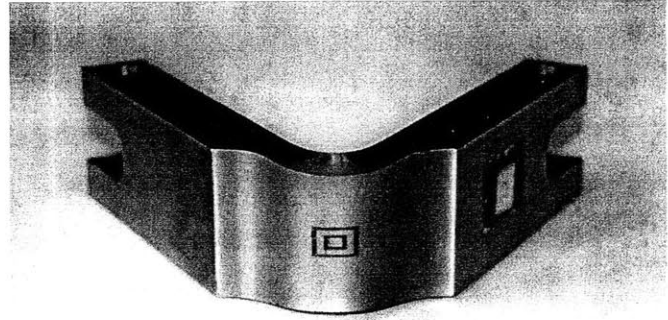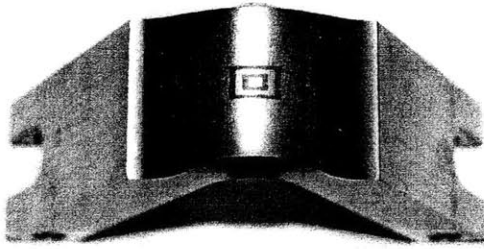
Figure I11   Deformed strain gauge marks on bent specimens

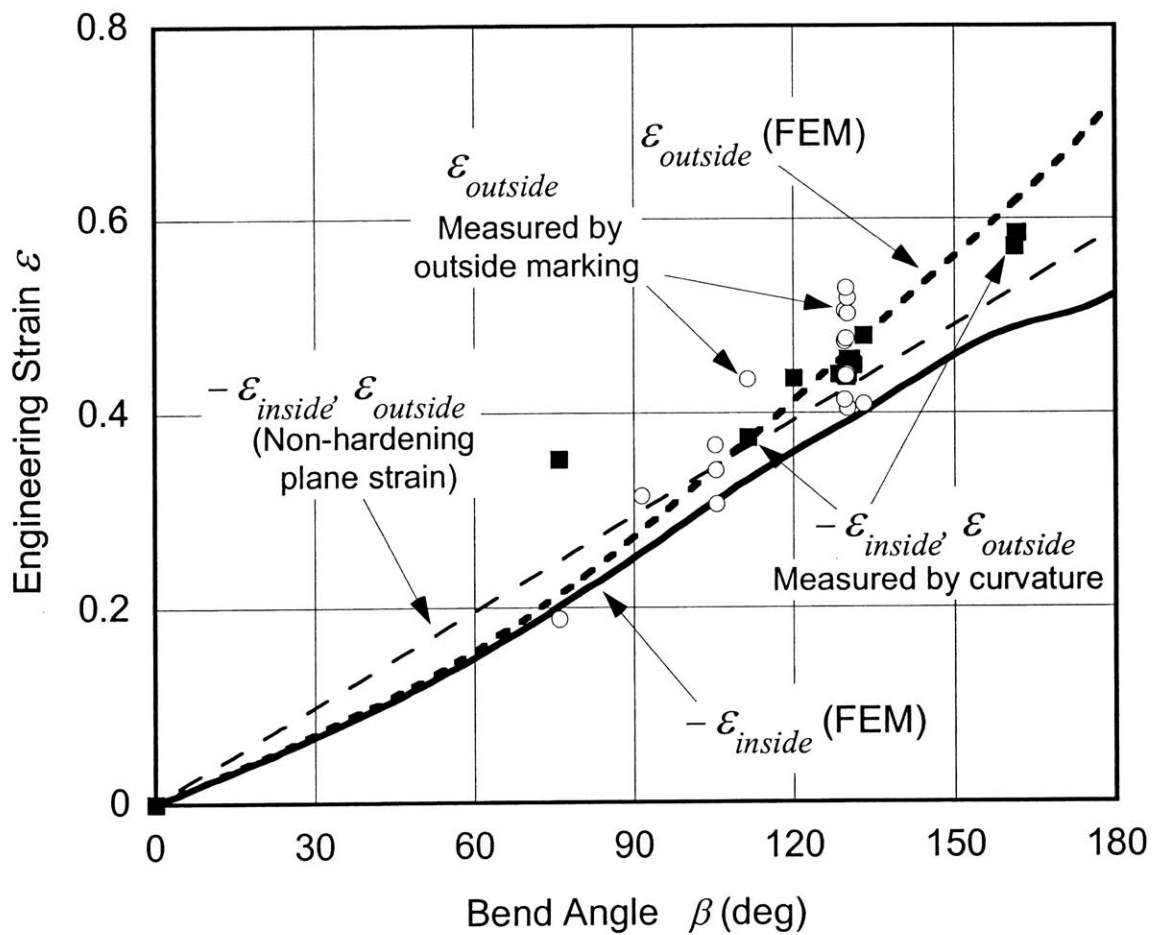*Figure I12   Comparison of bending strain versus bend angle by theory, FEM, and measurement, h = 9.525 mm, s_{eff} = 25.4 mm*

Table I3   *Test results*

Specimen #	Thickness after bending (mm)	Effective Arc Length (mm)	Opening Angle (deg)	Inner Radius (mm)	Extension at cleavage (mm)	Temp. during reversal (°C)	Engineering pre-strain	Reversed strain at cleavage	Surface As-Rolled Machined	Strain mark before (mm)	Strain mark after (mm)	
7*	-	25.4	<60	6.15	65.00	20	-0.393	0.2792	A	2.	-	no cleavage
8*	-	25.4	75.9	8.73	-	20	-0.248	0.0943	A	2.	2.60	no cleavage
9*	-	25.4	68.5	7.94	65.00	20	-0.365	0.3016	A	2.	2.87	no cleavage
10*	-	25.4	47	5.16	65.00	20	-0.435	0.2647	A	2.	3.30	no cleavage
12	9.65	25.4	50.03	5.95	6.66	-30	-0.431	0.0242	A	2.00	2.88	
13	9.71	25.4	48.9	5.95	10.54	-45	-0.437	0.0391	A	2.00	3.24	
14	9.64	25.4	49.23	5.75	29.94	-40	-0.433	0.1135	A	2.00	2.90	
15	9.64	25.4	49.48	5.75	13.27	-40	-0.432	0.0488	A	2.00	2.74	
16	**9.67**	**25.4**	**49.84**	**5.95**	**74.70**	**-40**	**-0.432**	**0.3280**	**M**	**2.00**	**2.81**	
17	9.64	25.4	49.9	5.75	61.07	-20	-0.431	0.2521	A	2.00	3.13	
18	9.63	25.4	49.69	5.75	3.06	-30	-0.431	0.0110	A	2.00	2.98	
19	9.65	25.4	49.88	5.95	3.55	-30	-0.431	0.0129	A	2.00	2.96	
20	9.63	25.4	50.35	6.15	3.81	-40	-0.429	0.0138	A	2.00	3.01	
21	**9.64**	**25.4**	**49.88**	**5.95**	**79.26**	**-20**	**-0.431**	**0.3544**	**M**	**2.09**	**3.14**	
22	9.67	25.4	51.53	6.15	5.15	-40	-0.427	0.0187	A	1.97	3.11	
23	9.66	25.4	50.13	6.15	3.12	-30	-0.431	0.0113	A	2.10	3.27	
24	9.64	25.4	50.16	6.15	4.58	-30	-0.43	0.0166	A	2.10	3.02	
25	9.69	25.4	50.31	6.15	63.13	-20	-0.432	0.2652	A	2.09	3.08	
26	**9.69**	**25.4**	**49.89**	**6.15**	**76.06**	**-30**	**-0.433**	**0.3375**	**M**	**1.93**	**2.93**	
30	9.6	31.75	104.04	-	23.00	-40	-0.200	0.0872	A	2.07	2.46	no cleavage
31	9.64	31.75	103.45	-	23.00	-40	-0.203	0.0868	A	2.12	2.38	no cleavage
32	9.62	31.75	46.82	-	59.06	-40	-0.352	0.1731	A	1.98	2.79	
34	9.7	31.75	66.1	-	63.51	-40	-0.304	0.2197	A	2.20	2.77	no cleavage
35	9.69	31.75	65.89	-	49.46	-40	-0.304	0.1550	A	2.28	2.96	no cleavage
40	9.58	25.4	50.09	6.15	71.24	-25	-0.428	0.3031	A	2.10	3.10	
41	9.62	25.4	50.33	6.15	52.21	-30	-0.429	0.2087	A	2.13	3.01	
42	9.63	25.4	50.11	5.95	24.71	-30	-0.430	0.0924	A	2.10	3.21	
43	9.62	25.4	74.32	-	53.19	-40	-0.349	0.2408	A	2.22	2.90	no cleavage
44	9.61	25.4	74.45	-	14.79	-40	-0.348	0.0551	A	2.17	2.91	
45	9.6	25.4	88.51	-	36.61	-40	-0.302	0.1668	A	2.13	2.80	no cleavage
46	9.61	25.4	74.57	-	55.08	-40	-0.348	0.2537	A	2.10	2.87	

* with sharp corners other than round corners

Table I4   *Test results sorted by pre-strain and temperature during reversal*

Specimen No.	Planned Nominal pre-strain	Engineering pre-strain	Temperature during reversal (°C)	Reversed strain at cleavage	Surface As-Rolled or Machined
7*[1]	-	-0.393	20	0.279*[2]	A
8*[1]	-	-0.248	20	0.094*[2]	A
9*[1]	-	-0.365	20	0.302*[3]	A
10*[1]	-	-0.435	20	0.265*[4]	A
30	-0.20	-0.200	-40	0.087*[5]	A
31	-0.20	-0.203	-40	0.087*[5]	A
34	-0.30	-0.304	-40	0.220*[5]	A
35	-0.30	-0.304	-40	0.155*[5]	A
45	-0.30	-0.302	-40	0.167*[5]	A
32	-0.35	-0.352	-40	0.173	A
43	-0.35	-0.349	-40	0.241*[5]	A
44	-0.35	-0.348	-40	0.055	A
46	-0.35	-0.348	-40	0.254	A
17	-0.43	-0.431	-20	0.252	A
25	-0.43	-0.432	-20	0.265	A
40	-0.43	-0.428	-25	0.303	A
12	-0.43	-0.431	-30	0.024	A
18	-0.43	-0.431	-30	0.011	A
19	-0.43	-0.431	-30	0.013	A
23	-0.43	-0.431	-30	0.011	A
24	-0.43	-0.430	-30	0.017	A
41	-0.43	-0.429	-30	0.209	A
42	-0.43	-0.430	-30	0.092	A
14	-0.43	-0.433	-40	0.113	A
15	-0.43	-0.432	-40	0.049	A
20	-0.43	-0.429	-40	0.014	A
22	-0.43	-0.427	-40	0.019	A
13	-0.43	-0.437	-45	0.039	A
21	-0.43	-0.431	-20	0.354	M
26	-0.43	-0.433	-30	0.338	M
16	-0.43	-0.432	-40	0.328	M

*[1] At end of thinned section, 0.5 mm R corners rather than 19.05 mm R fillets.

*[2] Fractured at fillet on bending after this first reversed strain.

*[3] Shear cracking and instability on second such reversed straining.

*[4] Shear cracking and instability on bending after this first reversed strain.
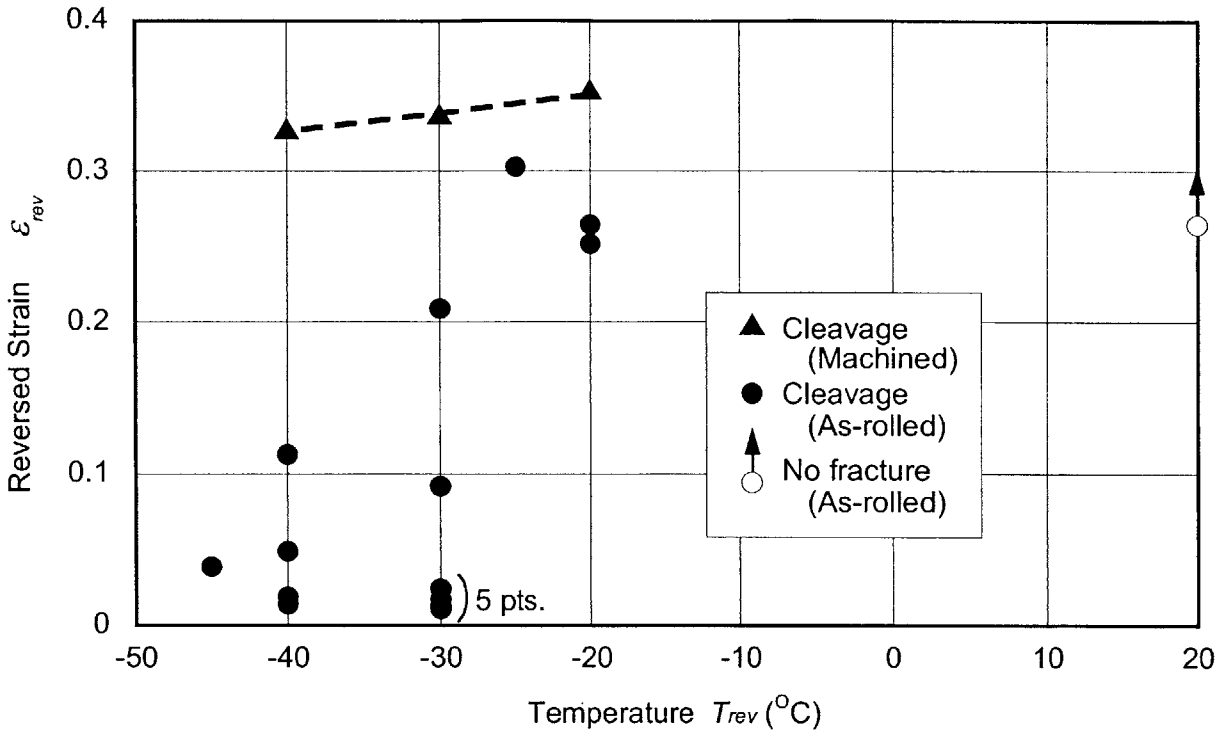
*[5] Stopped at jig limit (22 kN) before fracture.

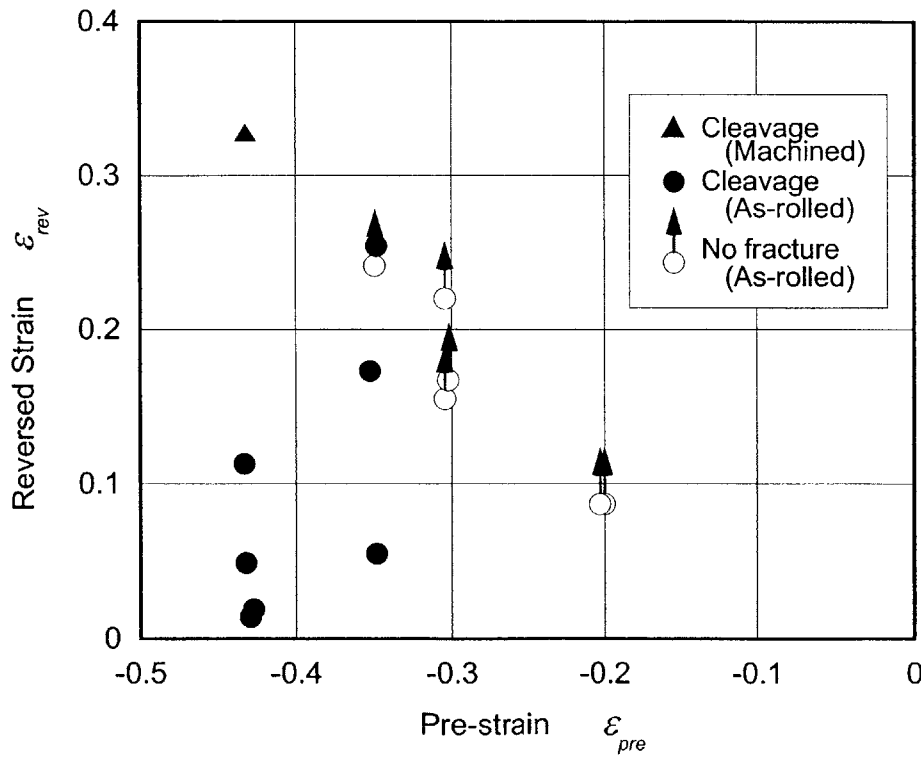*Figure I13*   *Reversed strain to fracture at $\varepsilon_{pre} = -0.43$*

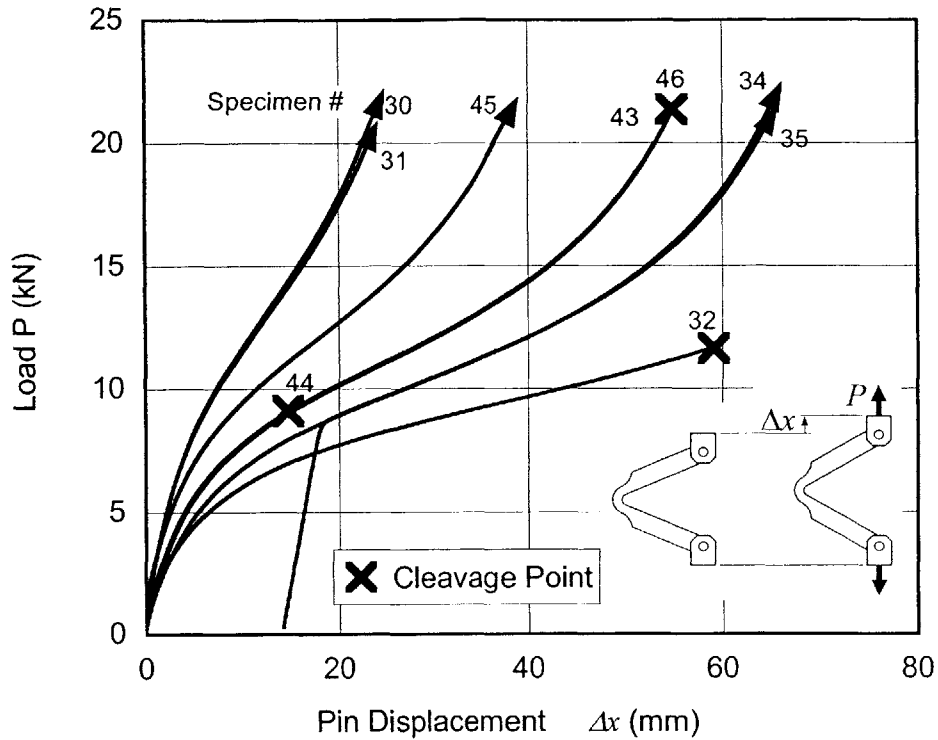*Figure I14*   *Reversed strain to fracture at $T = -40\ °C$*

Figure I15a   Load-displacement curves to fracture,   T = –40 °C   Note: Specimens 30, 31, 32, 34, and 35 had longer effective arc length (Table I3) but same total length.
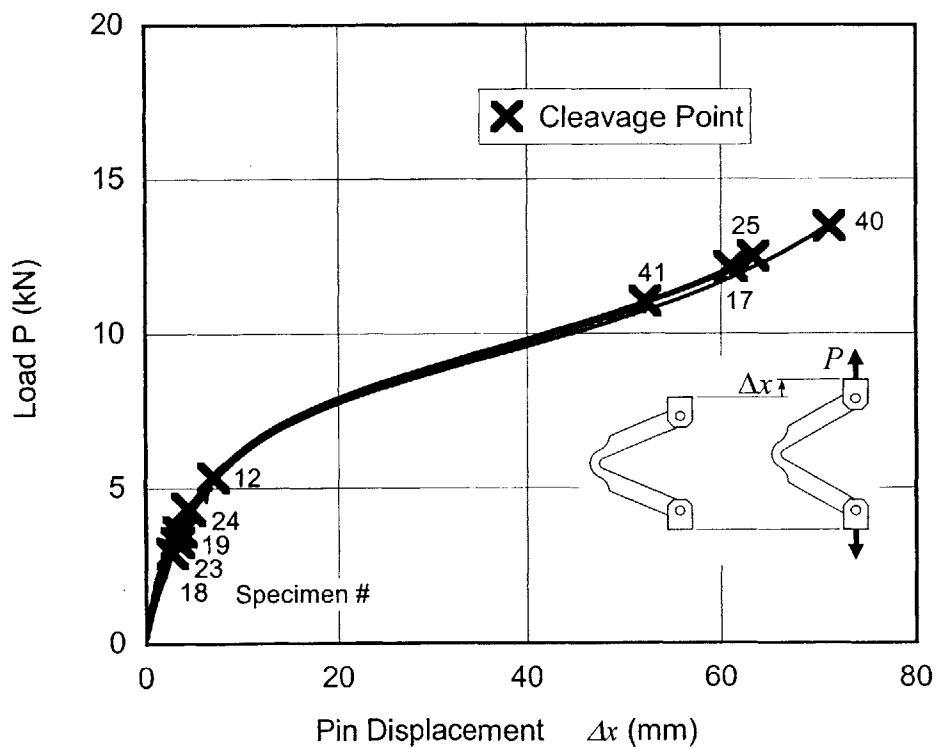

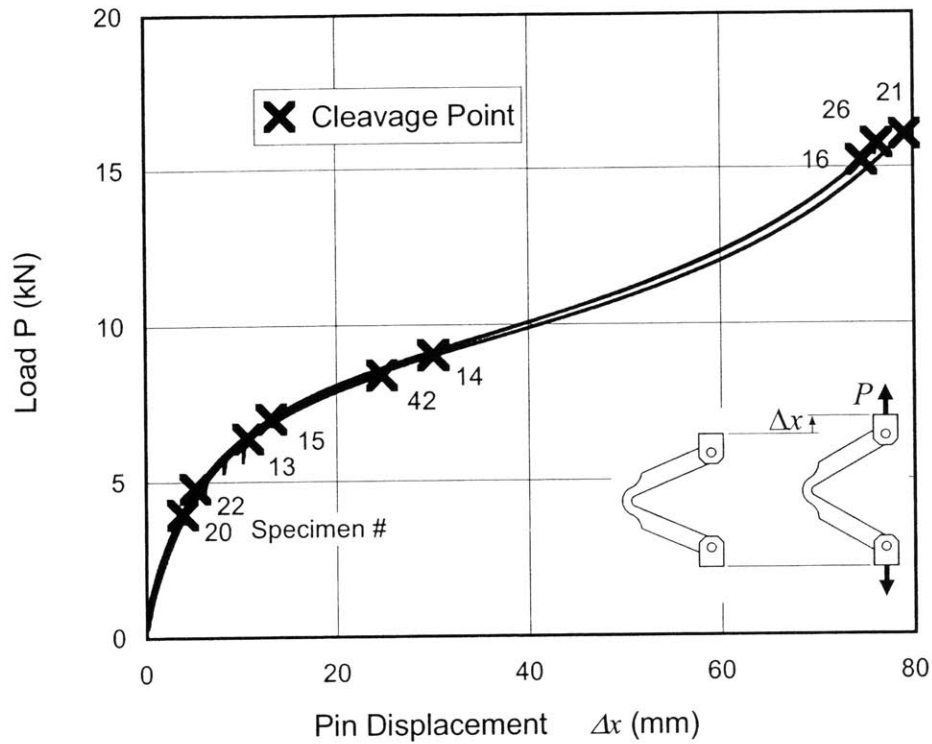*Figure I15b   Load-displacement curves to fracture, ε_{pre} = –0.43 (See also Figure I15c)*

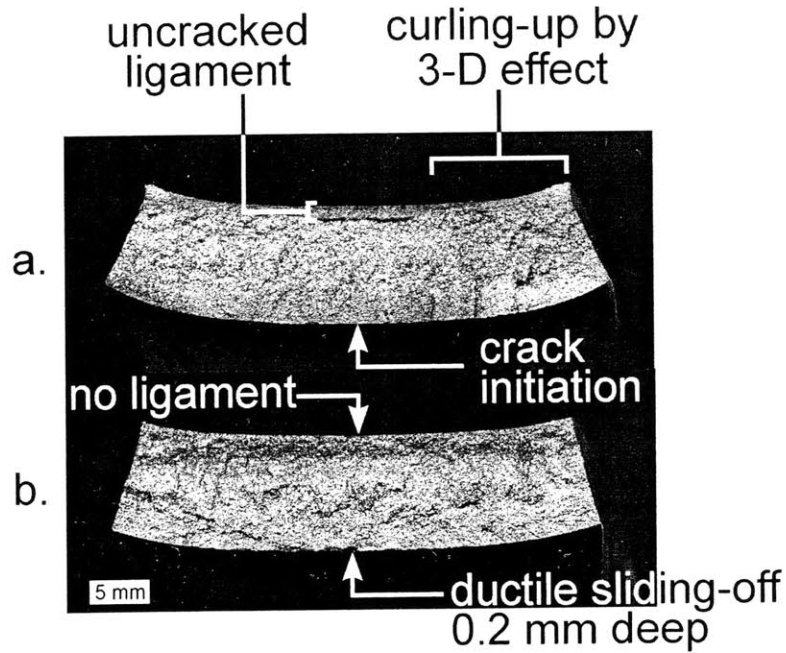*Figure I15c   Load-displacement curves to fracture, $\varepsilon_{pre} = -0.43$*

Figure I16   Cleavage surfaces after pre-strain of $\varepsilon_{pre} = -0.43$, a. $T_{rev} = -40\ °C$ and $\varepsilon_{revf} = 0.019$, b. $T_{rev} = -20\ °C$ and $\varepsilon_{revf} = 0.265$

Appendix J   Temperature Equilibration Inside the Specimen

Abstract

In the reverse bending cleavage tests, the specimen is cooled down to –40 °C. The thermal saturation analysis was done inside the bending specimen. The temperature equilibration was found to be established within 10^{-5} of initial temperature difference in 12 minutes, while the saturation time of 60 minutes was taken for each bent specimen in the tests.

Nomenclature

a_n	nth constant
a_t	thermal diffusivity (m²/sec) $a_t = K/\rho C_P$
Bi	Biot number, e.g. hL/K
C_n	nth constant
C_P	specific heat (J/kg·K)
h	heat transfer coefficient (W/m²·K)
K	thermal conductivity (W/m·K)
l, L	thickness or width
t	time
T	temperature
T_0	initial temperature
T_∞	temperature of heat source
x, y	coordinate
X, Y	independent functions
γ_m	mth characteristic value
λ_n	nth characteristic value
θ	relative temperature
Θ	normalized relative temperature
ρ	density (kg/m³)
τ	independent function

1.   Introduction

In the reverse bending cleavage tests, the reversed strain to cleavage is found as a function of the pre-strain and the reverse bending temperature. The specimen is pre-bent first. After that, the specimen is put in the temperature controlled chamber, and kept in a constant low temperature atmosphere for a certain period to saturate the temperature distribution inside the specimen. After the saturation, the specimen is reverse bent at the low temperature.

The saturation period was verified by thermal conduction analysis.

2.   Analysis

Figure J1 shows the bending specimen. The thickness of the bending specimen is reduced in the middle, and the cross section is rectangular of 38.10 × 9.525 mm. The parallel part is 19.05 mm long. The part is modeled as an infinitely long prism which has a constant cross section. In the following subsections, the transient temperature distribution will be derived starting with a one-dimensional model with infinite and finite heat transfer coefficients. Based on the solution, the solutions for two-dimensional models with infinite and finite heat transfer coefficients will be obtained. Although the author was straightaway devoted to the numerical method, an estimation using charts or handbooks may be recommended for practical applications. Since the aspect ratio of the cross section of the specimen is four, it may be modeled as an infinitely large plate.

2.1   Infinitely large plate with infinite heat transfer coefficient

Consider an infinitely large plate of thickness $2L$. Figure J2 shows its cross section. Assume the heat transfer coefficient is infinitely large. The initial temperature of the plate is T_0. Put the plate in the atmosphere of temperature T_∞ at time $t = 0$. Consider the transition temperature $T(x,t)$ at time t and at a position x from the center plane. Let the relative temperature be $\theta(x,t)$.

$$\theta(x,t) \equiv T(x,t) - T_\infty \tag{J1}$$

The equation of heat conduction in one dimension is

$$\frac{\partial \theta}{\partial t} = a_t \frac{\partial^2 \theta}{\partial x^2} \tag{J2}$$

The initial condition is

$$\theta(x,0) = \theta_0 \equiv T_0 - T_\infty \tag{J3}$$

The boundary conditions are

$$\frac{\partial \theta(0,t)}{\partial x} = 0 \tag{J4}$$

$$\theta(L,t) = 0 \tag{J5}$$

The method of separation of variables consists of seeking particular "product solutions" of (J2) in the form

$$\theta(x,t) \equiv X(x)\tau(t) \tag{J6}$$

where X is a function of x alone and τ is a function of t alone. If (J6) is introduced into (J2), there follows

$$\frac{X''}{X} - \frac{1}{a_t}\frac{\tau'}{\tau} = 0 \tag{J7}$$

If an arbitrary constant λ is introduced, there follows

$$\frac{d^2 X}{dx^2} + \lambda^2 X = 0 \tag{J8}$$

$$\frac{d\tau}{dt} + a_t \lambda^2 \tau = 0 \tag{J9}$$

The boundary conditions (J4) and (J5) give

$$\frac{dX(0)}{dx} = 0 \tag{J10}$$

$$X(L) = 0 \tag{J11}$$

The solution of (J8) is of the form

$$X(x) = C_1 \cos(\lambda x) + C_2 \sin(\lambda x) \tag{J12}$$

The conditions (J10) and (J11) yield

$$C_2 = 0$$
$$0 = C_1 \cos(\lambda L)$$

$$\lambda_n L = \frac{2n+1}{2}\pi \quad (n = 0,1,2,\cdots) \tag{J13}$$

The solution of (J9) is of the form

$$\tau_n(t) = C_n e^{-a_t \lambda_n^2 t} \tag{J14}$$

Thus it follows that any particular solution of the form

211

$$\theta\left(x,t\right)=\sum_{n=0}^{\infty}a_{n}e^{-a_{t}\lambda_{n}^{2}t}\cos\lambda_{n}x \tag{J15}$$

satisfies Equation (J2). Applying (J3) to (J15) gives

$$\theta_{0}=\sum_{n=0}^{\infty}a_{n}\cos\lambda_{n}x \tag{J16}$$

Multiply both sides by $\cos\lambda_{n}x$, then integrate by x from 0 to L.

$$\int_{0}^{L}\theta_{0}\cos\lambda_{n}xdx=a_{n}\int_{0}^{L}\cos^{2}\lambda_{n}xdx$$

$$=a_{n}\frac{L}{2}\quad\left(\because\cos\lambda_{n}L=0\right)$$

$$a_{n}=\left(-1\right)^{n}\frac{2\theta_{0}}{\lambda_{n}L} \tag{J17}$$

Introducing (J17) into (J15) gives

$$\frac{\theta}{\theta_{0}}=\frac{T\left(x,t\right)-T_{\infty}}{T_{0}-T_{\infty}}=2\sum_{n=0}^{\infty}\frac{\left(-1\right)^{n}}{\lambda_{n}L}e^{-a_{t}\lambda_{n}^{2}t}\cos\lambda_{n}x \tag{J18}$$

2.2 Infinitely large plate with finite heat transfer coefficient

Consider an infinitely large plate whose thickness is $2L$ shown in Figure J3. This time, assume the heat transfer coefficient is finite. Consider the relative temperature $\theta(x,t)$ again.

$$\theta\equiv T-T_{\infty}$$
$$\theta_{0}\equiv T_{0}-T_{\infty} \tag{J19}$$

The equation of heat conduction in one dimension is

$$\frac{\partial\theta}{\partial t}=a_{t}\frac{\partial^{2}\theta}{\partial x^{2}} \tag{J20}$$

The initial condition is

$$\theta\left(x,0\right)=\theta_{0} \tag{J21}$$

The boundary conditions are

$$\frac{\partial\theta\left(0,t\right)}{\partial x}=0 \tag{J22}$$

$$\frac{\partial\theta\left(L,t\right)}{\partial x}=-\frac{h}{K}\theta\left(L,t\right) \tag{J23}$$

The same method of separation of variables in the form of (J6) yields

$$\frac{d^2 X}{dx^2} + \lambda^2 X = 0 \tag{J24}$$

The boundary conditions (J22) and (J23) are interpreted as

$$\frac{dX(0)}{dx} = 0 \tag{J25}$$

$$\frac{dX(L)}{dx} + \frac{h}{K} X(L) = 0 \tag{J26}$$

The solution of (J18) is of the form

$$X(x) = C_1 \cos \lambda x + C_2 \sin \lambda x \tag{J27}$$

The conditions (J25) and (J26) yield

$$C_2 = 0$$

$$\lambda_n L \tan(\lambda_n L) = \frac{hL}{K}$$

hL/K is called "Biot Number", Bi and

$$\lambda_n L \tan(\lambda_n L) = Bi \tag{J28}$$

The method of separation of variables in the form of (J6) yields another equation.

$$\frac{d\tau}{dt} + a_t \lambda^2 \tau = 0 \tag{J29}$$

The solution of (J29) is of the form

$$\tau_n(t) = C_n e^{-a_t \lambda_n^2 t} \tag{J30}$$

Thus it follows that any particular solution of the form

$$\theta(x,t) = \sum_{n=1}^{\infty} a_n e^{-a_t \lambda_n^2 t} \cos \lambda_n x \tag{J31}$$

where λ_n are root of (J28), satisfies Equation (J20). Applying (J21) to (J31) gives

$$\theta_0 = \sum_{n=1}^{\infty} a_n \cos \lambda_n x \tag{J32}$$

Multiplying both sides by $\cos \lambda_n x$ and integrating by x from 0 to L give

$$a_n = \frac{2\theta_0 \sin \lambda_n L}{\lambda_n L + \sin \lambda_n L \cos \lambda_n L} \tag{J33}$$

Introducing (J33) into (J31) gives

$$\frac{\theta}{\theta_0} = \frac{T - T_\infty}{T_0 - T_\infty} = 2\sum_{n=1}^{\infty}\left(\frac{\sin\lambda_n L}{\lambda_n L + \sin\lambda_n L \cos\lambda_n L}\right)e^{-a_t\lambda_n^2 t}\cos\lambda_n x \qquad (J34)$$

2.3   Infinitely long rectangular prism with infinite heat transfer coefficient

Consider an infinitely long rectangular prism whose width is $2L$ and thickness is $2l$. Figure J4 shows its cross section. Assume the heat transfer coefficient is infinitely large. The initial temperature of the prism is T_0. Put the prism in the atmosphere of temperature T_∞ at time $t = 0$. Consider the transition temperature $T(x,y,t)$ at time t and at a position x and y from the center of the section. Let the normalized relative temperature be $\Theta(x,y,t)$.

$$\Theta(x,y,t) \equiv \frac{T - T_\infty}{T_0 - T_\infty} \qquad (J35)$$

The equation of heat conduction in two dimensions is

$$\frac{\partial\Theta}{\partial t} = a_t\left(\frac{\partial^2\Theta}{\partial x^2} + \frac{\partial^2\Theta}{\partial y^2}\right) \qquad (J36)$$

The initial condition is

$$\Theta(x,y,0) = 1 \qquad (J37)$$

The boundary conditions are

$$\frac{\partial\Theta(0,y,t)}{\partial x} = 0 \quad \Theta(L,y,t) = 0 \qquad (J38)$$

$$\frac{\partial\Theta(x,0,t)}{\partial x} = 0 \quad \Theta(x,l,t) = 0 \qquad (J39)$$

The method of separation of variables consists of seeking particular "product solutions" of (J36) in the form

$$\Theta(x,y,t) \equiv X(x,t)Y(y,t) \qquad (J40)$$

where X is a function of x and t alone, and T is a function of y and t alone. If (J40) is introduced into (J36), there follows

$$\frac{1}{X}\left(\frac{\partial X}{\partial t} - a_t\frac{\partial^2 X}{\partial x^2}\right) = -\frac{1}{Y}\left(\frac{\partial Y}{\partial t} - a_t\frac{\partial^2 Y}{\partial y^2}\right) \qquad (J41)$$

Since the both hands of (J41) are independent, there follows

$$\frac{\partial X}{\partial t} = a_t \frac{\partial^2 X}{\partial x^2} \tag{J42}$$

$$X(x,0) = 1 \tag{J43}$$

$$\frac{\partial X(0,t)}{\partial x} = 0 \tag{J44}$$

$$X(L,t) = 0 \tag{J45}$$

and

$$\frac{\partial Y}{\partial t} = a_t \frac{\partial^2 Y}{\partial y^2} \tag{J46}$$

$$Y(y,0) = 1 \tag{J47}$$

$$\frac{\partial Y(0,t)}{\partial y} = 0 \tag{J48}$$

$$Y(l,t) = 0 \tag{J49}$$

Thus, the problem becomes expressible as the product of two one-dimensional unsteady problems. Equation (J40) means

$$\left(\frac{T-T_\infty}{T_0-T_\infty}\right)_{\substack{2L,2l \\ 2D\,plate}} = \left(\frac{T-T_\infty}{T_0-T_\infty}\right)_{\substack{2L \\ 1D\,plate}} \times \left(\frac{T-T_\infty}{T_0-T_\infty}\right)_{\substack{2l \\ 1D\,plate}} \tag{J50}$$

Using the form of (J18), there follows

$$\frac{T-T_\infty}{T_0-T_\infty} = 4\left\{\sum_{n=0}^{\infty}\frac{(-1)^n}{\lambda_n L}e^{-a_t\lambda_n^2 t}\cos\lambda_n x\right\}\left\{\sum_{m=0}^{\infty}\frac{(-1)^m}{\lambda_m l}e^{-a_t\gamma_m^2 t}\cos\gamma_m y\right\} \tag{J51}$$

where

$$\lambda_n L = \frac{2n+1}{2}\pi \quad (n = 0,1,2,\cdots) \tag{J52}$$

$$\gamma_m L = \frac{2m+1}{2}\pi \quad (m = 0,1,2,\cdots) \tag{J53}$$

2.4   Infinitely long rectangular prism with finite heat transfer coefficient

Finally, consider an infinitely long rectangular prism with finite heat transfer coefficient whose width is $2L$ and thickness is $2l$. Figure J5 shows its cross section. Equation (J50) is still

valid here for $T(x,y,t)$. Using the expression of (J34), the expression of the temperature distribution transition is

$$\frac{T-T_\infty}{T_0-T_\infty} = 4\sum_{n=1}^{\infty}\left(\frac{\sin\lambda_n L}{\lambda_n L + \sin\lambda_n L\cos\lambda_n L}\right)e^{-a_t\lambda_n^2 t}\cos\lambda_n x$$

$$\times\sum_{m=1}^{\infty}\left(\frac{\sin\gamma_m l}{\gamma_m l + \sin\gamma_m l\cos\gamma_m l}\right)e^{-a_t\gamma_m^2 t}\cos\gamma_m y \tag{J54}$$

$$\lambda_n L\tan\left(\lambda_n L\right) = Bi_L \tag{J55}$$

$$\gamma_m l\tan\left(\gamma_m l\right) = Bi_l \tag{J56}$$

where

$$Bi_L = \frac{hL}{K} \tag{J57}$$

$$Bi_l = \frac{hl}{K} \tag{J58}$$

3. Calculation

Using Equations (J54) to (J58), the temperature distribution transition was calculated. Equations (J55) and (J56) give a series of λ_n and γ_m for the increase of index parameters n and m. To obtain a good approximation for the infinite summation in (J54), n and m were taken up to twenty. Namely,

$$\frac{T-T_\infty}{T_0-T_\infty} = 4\sum_{n=1}^{20}\left(\frac{\sin\lambda_n L}{\lambda_n L + \sin\lambda_n L\cos\lambda_n L}\right)e^{-a_t\lambda_n^2 t}\cos\lambda_n x$$

$$\times\sum_{m=1}^{20}\left(\frac{\sin\gamma_m l}{\gamma_m l + \sin\gamma_m l\cos\gamma_m l}\right)e^{-a_t\gamma_m^2 t}\cos\gamma_m y \tag{J59}$$

Figure J6 shows the cross section of the bending specimen. The calculation was done along y-axis ($x = 0$). The following properties were used. Typical values were chosen for the thermal conductivity and the heat transfer coefficient from Shoji (1995).

Density of steel	ρ	7850	(kg/m^3)
Specific heat of steel	C_P	0.12 (kcal/kg·°C)	502.326 (J/kg·K)
Thermal conductivity	K	20 (W/m·K) for steel	

Heat transfer coefficient	h	200 (W/m²·K) for slow air forced convection
Thermal diffusivity	a_t	5.07×10^{-6} (m²/s)
Half width	L	0.01905 (m)
Half thickness	l	0.00476 (m)
Biot number for width	Bi_L	0.1905
Biot number for thickness	Bi_l	0.0476

The result for passing times is shown in Figure J7. The abscissa is the normalized distance of y-coordinate, and the ordinate is the normalized relative temperature Θ. At time 0 second, Θ is unity at any locations. As the time is passing, Θ is decreasing almost uniformly at all locations. In 300 seconds, Θ is less than 0.1 anywhere. Finally, the temperature difference at the center of specimen decreased down to less than 10^{-5} of the initial difference in 720 seconds, and the temperature distribution almost equilibrated.

4. Conclusion

The temperature inside the specimen reached the design temperature uniformly in 12 minutes. The period of 60 minutes is enough for the temperature equilibration in the reverse bending cleavage tests.

Acknowledgement

The author expresses his profound appreciation of a great job by Mr. Yoichi Murakami on the derivation of the analytical solutions.

Reference

SHOJI, M. 1995 *Heat Transfer Textbook (Japanese)*, University of Tokyo Series on Advanced Mechanical Engineering 6
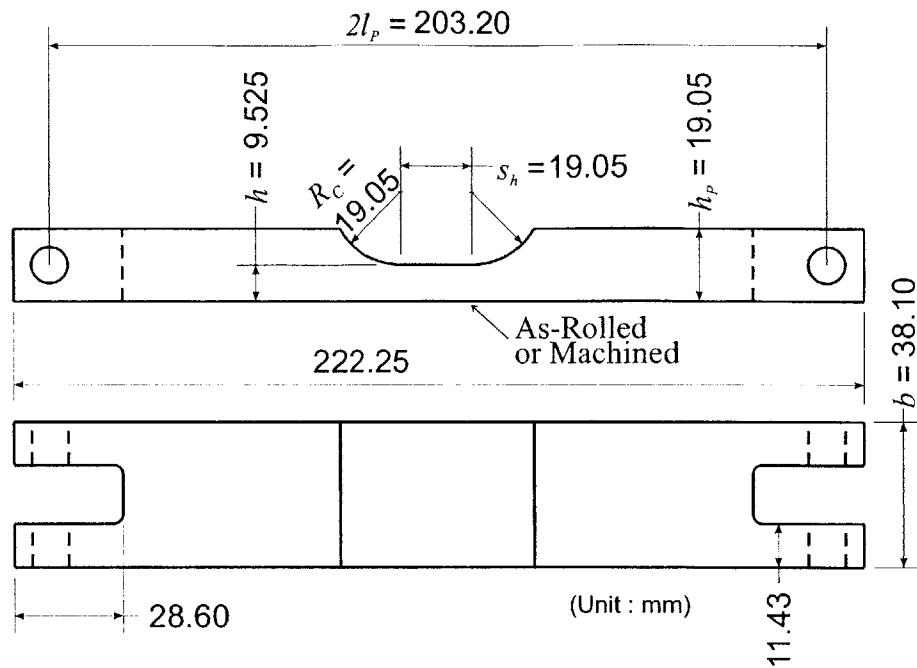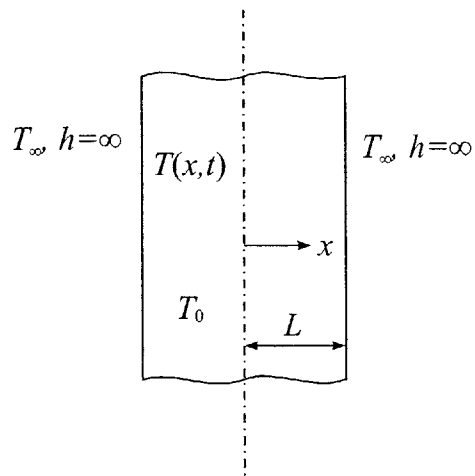
Figure J1   *Reverse bending specimen*

Figure J2   *Infinitely large plate with infinite heat transfer coefficient*
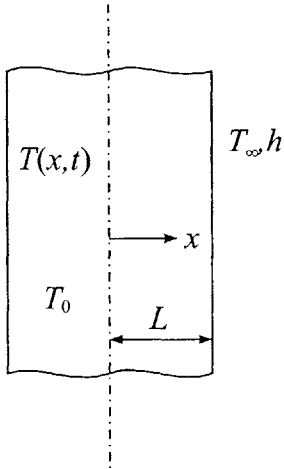
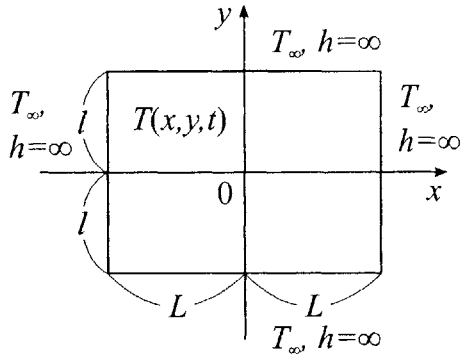*Figure J3*   *Infinitely large plate with finite heat transfer coefficient*

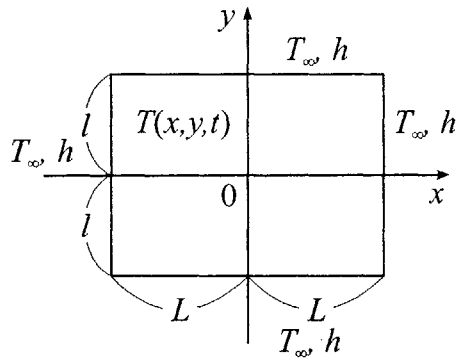*Figure J4*   *Infinitely long rectangular prism with infinite heat transfer coefficient*

Figure J5   *Infinitely long rectangular prism with finite heat transfer coefficient*
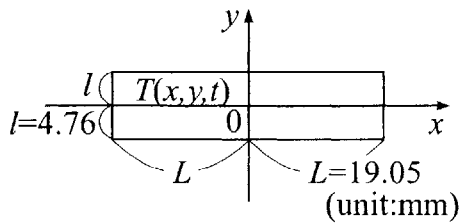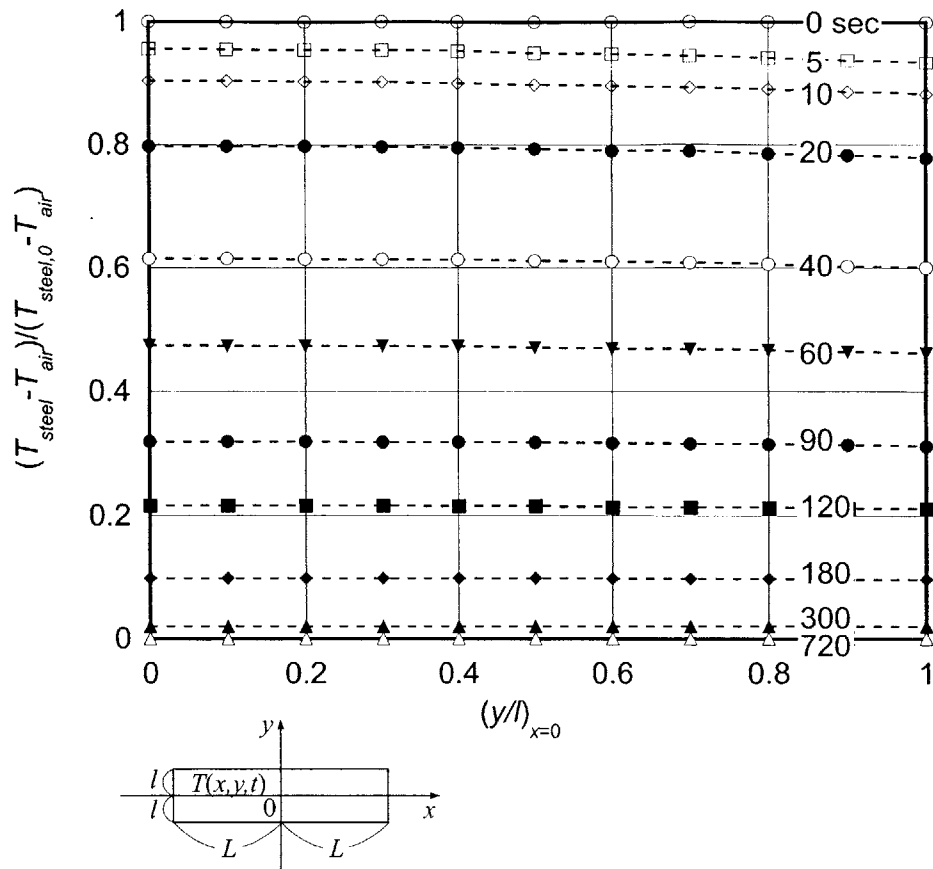
Figure J6   *Cross section of the bending specimen*

Figure J7   *Temperature transient along x = 0 in the direction of plate thickness (l/L = 0.25, hL/K = 0.1905, hl/K = 0.0476)*